Dissertation

submitted to the

Combined Faculty of Mathematics, Engineering and Natural Sciences

of Heidelberg University, Germany

for the degree of

Doctor of Natural Sciences

Put forward by

Sangeetha Sasidharan

born in: Cochin, Kerala, India

Oral examination: October 18, 2023

High-precision atomic mass measurement of helium-4

Referees: PD Dr. Wolfgang Quint

PD Dr. Robert Moshammer

Hochpräzise Messung der Atommasse von Helium-4

Die Penningtrap-Massenspektrometrie ermöglicht eine präzise Bestimmung von Atommassen und unterstützt damit empfindliche Tests der fundamentalen Physik. LIONTRAP (Light Ion TRAP) ist ein spezialisiertes Massenspektrometer, das auf präzise Massenmessungen von leichten Ionen ausgerichtet ist. Mit diesem Experiment erreichen wir derzeit eine relative Auflösung von 10^{-11} und besser für Atommassen. Das Messprinzip beruht auf dem Vergleich der Zyklotronfrequenzen der untersuchten Ionen und eines Kohlenstoffions, die umgekehrt proportional zu ihren Massen sind. Im Rahmen dieser Arbeit wurde eine hochpräzise Massenmessung von $^4He^{2+}$ durchgeführt. Zu diesem Zweck wurde eine kryogene Atomquelle für gasförmige Elemente entwickelt und eine umfassende Untersuchung der systematischen Fehlerquellen welche die Massenmessungen beeinflussen, einschließlich des Bildladungseffektes, der Linienformsystematik und anderer Effekte, durchgeführt. Die hier ermittelte Masse hat eine relative Genauigkeit von 12×10^{-12}. Auf dieser Grundlage wird die atomare Masse des neutralen Atoms mittels der bekannten Bindungsenergien und der Elektronenmasse ohne Verlust an Präzision bestimmt. Der Massenwert weist eine Genauigkeit auf die 1,3-mal größer ist als der Literaturwert, weicht aber um 6,6 kombinierte Standardabweichungen von diesem ab. Dieses Ergebnis trägt zur Grundlagenphysik bei, indem es die Verbesserung der Elektronenmasse durch eine Bestimmung des g-Faktors von $^4He^+$ unterstützt. Gegen Ende der Arbeit werden neue Entwicklungen vorgestellt, darunter ein Test der Zwei-Ionen-Balkenwaagen-Technik zur Verbesserung der Präzision zukünftiger Massenmessungen.

High-precision atomic mass measurement of helium-4

Penning-trap mass spectrometry enables a precise determination of atomic masses, supporting sensitive tests of fundamental physics. LIONTRAP (Light Ion TRAP) is a specialized mass spectrometer focused on precise mass measurements of light ions. In this experiment, we currently reach a relative resolution of 10 parts-per-trillion (ppt) and beyond for atomic masses. The measurement principle involves comparing the cyclotron frequencies of the ions under investigation and a carbon ion, which are inversely proportional to their masses. In the scope of this thesis, a high-precision mass measurement of $^4He^{2+}$ was performed. To this end, a source for gaseous species was developed, and an extensive investigation of the systematics affecting the mass measurements, including image charge shift, lineshape systematics, and others, was conducted. The mass determined herein has a relative precision of 12 ppt. Based on this, the atomic mass of the neutral atom is determined from the binding energies and the electron mass without loss of precision. The mass value exhibits a precision that is 1.3 times greater than the current literature value but deviates from it by 6.6 combined standard deviations. This result contributes to fundamental physics by potentially supporting the improvement of the electron mass via a g-factor determination of $^4He^+$. Towards the end of the thesis, new developments are presented, including a test of the two-ion-balance technique to improve the precision of the upcoming mass measurement.

Contents

List of Figures

List of Tables

1. Introduction

The secret of getting ahead is getting started.

Mark Twain

Mass is an intrinsic and fundamental property that characterizes a particle. The field of mass spectrometry dates back to the time when J. J. Thompson began his hunt for electrons [1, 2] and has now come to the present day when high-precision mass measurements have reached a relative precision of few parts per trillion [3, 4]. State-of-the-art mass measurements with the highest level of accuracy are accomplished mainly by conducting single ion measurements within a Penning trap (see chapter 2). Mass measurement in an electromagnetic field in a trap translates to a comparison of frequencies (see section 6.1).

Although an additional digit to the mass value or a modification in its minute fraction may seem inconsequential to everyday life, they have great significance and consequences with broader implications. The precise masses are used to define natural constants and test the fundamental charge, parity, and time reversal symmetry [5]. Mass measurements of atoms provide valuable information about the binding energies, including the cumulative effects of all the atomic and nuclear interactions.

1.1 Motivation: light ion masses

Masses of light particles like the electron, proton, and isotopes of hydrogen and helium are regarded as fundamental constants, and these also serve as essential parameters in deriving various other physical constants. For instance:

- The electron-to-proton mass ratio is an essential input parameter for evaluating the Rydberg constant [6].
- The atomic mass of the neutron (m_n) is determined from the mass of the deuteron (m_d) and the mass of the proton (m_p) along with the neutron separation energy ($S_n(d)$): $m_n = m_d - m_p + S_n(d)/c^2$ [7].
- A comparison of the measured and calculated free electron g-factor can serve as a stringent test of the Standard Model [8]. Here, the calculation requires an independent value of the fine-structure constant. Such a value can be extracted from atom

interferometry [9]. To this end, a high-precision value of the atom-to-electron mass ratio is required.

High-precision mass measurements can be directly utilized to test the validity of fundamental theories and probe physics beyond the well-accepted Standard Model. Some examples are as follows:

- A stringent test of CPT invariance in the leptonic and baryonic sectors can be performed by a precise comparison of the masses of particles (e.g., proton, electron) and their antiparticles (e.g., antiproton, positron) [10, 11]. Any deviation in the CPT theorem would indicate physics beyond the Standard Model.

- Precise mass measurements can also yield a test of Einstein's mass-energy relation, $E = mc^2$ [12, 13]. For example, in a neutron capture reaction, the daughter nucleus is formed in an excited state and decays via the emission of a gamma photon with an energy equivalent to the neutron separation energy. Therefore

$$(m(^{A}X) - m(^{A+1}X) + m_d - m_p)c^2 = S_n(^{A+1}X) - S_n(d) \tag{1.1}$$

  where ^{A}X is the parent nucleus, ^{A+1}X is the daughter nucleus, and $S_n(^{A+1}X)$ and $S_n(d)$ are energies of the gamma photons [13, 14]. The commonly used candidates are ^{29}Si, ^{33}S, and ^{36}Cl, which generate high-energy gammas. The right side of the Eq. (1.1) constitutes the gamma energies determined through the study of their diffraction angles in a double perfect crystal spectrometer [15]. The left-hand side of the equation constitutes the masses obtained from precision mass spectrometry. This also includes the light ion masses, such as the proton and the deuteron mass. If Eq. (1.1) is not fulfilled, it would indicate a violation of Einstein's equivalence principle.

Several other motivations are associated with light ion masses, which are further elaborated in the subsequent sections.

1.1.1 Light ion mass puzzle

Several experiments worldwide perform precision mass ratio measurements, and this way, establish a network of links between the masses of the light ions. However, in 2015 when the group of Prof. Edmund Myers at Florida State University (FSU) measured the ratio of HD^+ and $^3He^+$ [16] and also the group of Prof. Van Dyck at the University of Washington (UW) remeasured the mass of ^{3}He with ^{12}C ion as reference [17], a 4.4σ discrepancy got revealed among few light ion masses. The inconsistency is found when comparing different relations between the masses in this regime. The comparison occurs between the mass value of proton (m_p), deuteron (m_d), and helion (m_h) (^{3}He) when measured against ^{12}C as reference versus the direct measurement of the mass difference of the ^{3}He (m_h) and the HD^+ molecular

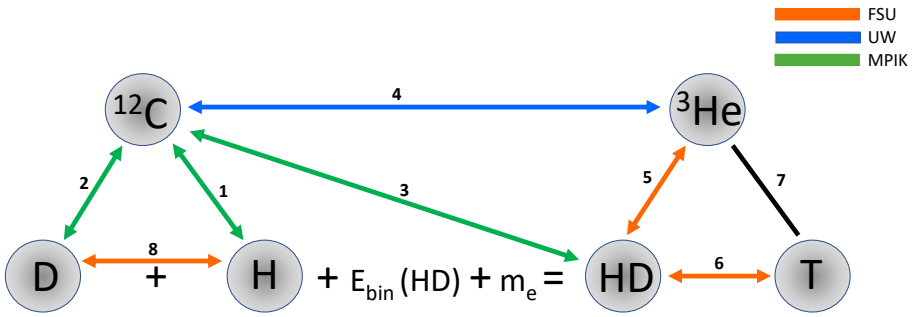

Figure 1.1. The light ion mass puzzle. The green links are measured at LIONTRAP (links **1** [19, 21], **2** [22], and **3** [22]). The orange links are measured at FSU (links **8** [4, 23], **5** [24], and **6** [16]), and the blue link is measured at the UW (link **4** [17]). Only the most recent high-precision measurements of the links are shown. The mass of HD^+ can be obtained from the mass of the proton and the deuteron, together with the involved binding energy and the mass of the electron. The black link (link **7** [25]) shows the mass ratio of interest to the KATRIN experiment.

ions. That is, $m_p + m_d - m_h$ from direct mass measurements against carbon performed at UW [17, 18] versus those obtained from mass ratio measurements ($HD^+/{}^3He^+$) performed at FSU [16]. This internal inconsistency among the high-precision mass values of the light ions is often referred to as the 'light ion mass puzzle' [19, 20].

The puzzle questions the reliability of these fundamental values. Consequently, the LIONTRAP (Light Ion TRAP) experiment was set up to remeasure the masses of light ions with respect to ^{12}C. So far, the proton and the deuteron atomic masses have been remeasured. Our mass values are in excellent agreement with the direct Penning trap measurement of the mass difference of $H_2{}^+$ and deuteron at FSU [4, 23]. The high-precision laser spectroscopy measuring transition frequencies in the rovibrational spectrum of the molecular HD^+ ion yields the ratio of involved masses and is found to be in good agreement [26, 27, 28]. The comparison here is limited by the precision of electron mass [29]. The value of $m_p+m_d-m_h$ from the two different kinds of measurements is compared in table 1.1. This includes the least square adjusted[1] proton and deuteron mass values [19, 22, 30] and helion mass measurement from UW [17] compared to the measurement of $HD^+/{}^3He^+$ by FSU [24]. The links that are presently involved in the puzzle are shown in Fig. 1.1.

Table 1.1. Inconsistency of light ion mass values. For details, see text.

$m_p + m_d - m_h$	Measured by
0.005897432191(70)	FSU [24]
0.005897432449(50)	LIONTRAP [21, 30] & UW [17]
258(86) pu	Deviation

[1]The mass values and uncertainties of the proton and the deuteron are derived from a least-squares adjustment including the mass measurements of the proton, the deuteron, HD^+ by LIONTRAP [19, 22] and the deuteron-to-proton mass ratio by the FSU [23] described in [30] and [31].

At LIONTRAP, primarily, two links measured by UW were remeasured. Our results reveal disagreements with those measured by the UW group, which were considered as the literature mass values. This discrepancy, along with the fact that a 3σ discrepancy remains in the light ion mass puzzle, provides a strong motivation to remeasure the mass of ^{3}He (with ^{12}C as reference), which is currently given by the measurement at UW.

1.1.2 Mass of helium-4

The mass of ^{4}He and its nucleus (α particle) holds significance in fundamental physics. The mass of the $^{4}He^{2+}$ is an important value in fundamental physics and has been included in the CODATA (Committee on Data for Science and Technology) tabulations [32]. In atomic physics, the mass of ^{4}He together with a measurement of the bound electron g-factor in $^{4}He^{+}$ can improve the electron's atomic mass. At present, the electron's atomic mass (m_e) is derived from the bound electron magnetic moment measurement of $^{12}C^{5+}$ [29, 32]. With the available experimental techniques and the current precision in the theory of the g-factor, the determination of m_e with $^{12}C^{5+}$ can be improved further, but it would be sensitive to and eventually limited by higher order bound-state QED contributions (in $\alpha^2(Z\alpha)^{6+}$). Alternatively, ^{4}He has the advantage that the theoretical binding corrections are known with higher precision or in other words, due to the lower nuclear charge, it is far less susceptible (by a factor $(2/6)^{6+}$) to higher-order terms of QED [33].

The recent progress towards precision in laser spectroscopy concerning $^{4}He^{+}$, muonic helium, and antiprotonic helium has heightened the significance of ^{4}He's mass [34, 35, 36]. For example, the field of laser spectroscopy of antiprotonic helium is heading towards improving the antiproton-to-electron mass ratio [36]. They aim to achieve precision at the level of 10^{-11}, which would also increase the impact of the involved mass ratio, i.e., antiproton-to-helium mass ratio. At the present level, the tabulated precision of the mass of ^{4}He seems sufficient; however, if the mass of ^{4}He deviated from the accepted value, it could have an impact.

A high precision and consistent value of ^{4}He mass would allow this highly stable and abundant particle to be used as a reference standard for other mass measurements.

The mass of ^{4}He has been measured before by several groups with different techniques. Some of the most precise determinations are reported in [37, 38, 39, 40, 41, 42]. At present, the result from the group of van Dyck at UW yields the accepted literature value by CODATA and AME (Atomic Mass Evaluation) [32, 43]. This result has a precision of 16 ppt. However, as mentioned in section 1.1.1, our results have previously revealed discrepancies with the masses measured at UW. The existing measurements of the ^{4}He mass by several groups have also shown inconsistencies. Consequently, it seems imperative to remeasure the mass of ^{4}He to establish a reliable value.

A mass measurement of ^{4}He is presented in this thesis.

1.1.3 Mass of tritium and helium-3

The discovery of neutrino oscillations was evidence that neutrinos possess a non-zero rest mass. This implies physics beyond the Standard Model. The physics goal of the KATRIN experiment is to measure the absolute electron anti-neutrino mass ($m_{\bar{\nu}_e}$) scale via the tritium beta-decay [44]. KATRIN performs a model-independent search of the electron anti-neutrino mass by precisely measuring the electron energy spectrum from the single β-decay of molecular tritium $T_2 \rightarrow {}^3HeT^+ + e^- + \bar{\nu}_e$. In the beta decay of tritium to helium, an electron, and an electron anti-neutrino are released. The released energy is shared between the electron's kinetic energy, the total neutrino energy, and the recoil energy of the daughter nucleus. The subtle effect of the neutrino mass is most evident at the endpoint region of the decay energy spectrum. A non-zero rest mass of the neutrino would distort the β spectrum at this region. The endpoint energy will also be shifted to a lower point compared to a case if the neutrino had a zero mass, see Fig. 1.2. This distortion in the spectrum is sensitive to the square of the effective neutrino mass. The current limit set by KATRIN is m_ν <0.8 eV/c^2 (90% confidence level) [25]. The aim of sensitivity on m_ν is 0.2 eV/c^2 (90% confidence level).

The Q value or the mass difference of tritium and helium-3 ($\Delta m = m(\mathrm{T}) - m({}^3\mathrm{He})$) can serve as a crosscheck for the systematics of the KATRIN experiment [46, 47]. Here, the interplay of slope distortion and endpoint shift becomes relevant. If the anti-neutrino mass is larger, the slope is more affected, and so is the extrapolated endpoint. But the endpoint can be calculated from the high-precision measurement of Δm, and any difference will indicate unaccounted systematic errors. The endpoint energy given by a highly precise value of the mass difference of tritium and helium-3 could even be used as fixed input to the

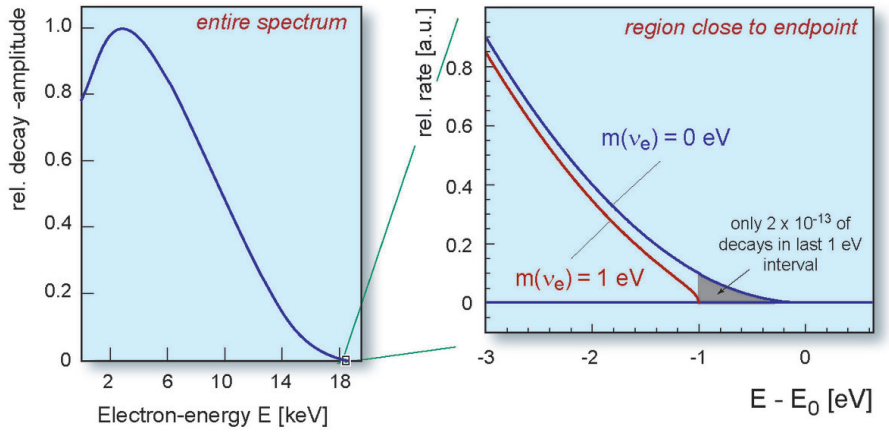

Figure 1.2. On the left is the β-decay spectrum of tritium, and on the right is a zoom into the endpoint region of the spectrum. The energy and the spectrum's shape at the endpoint depend on the electron anti-neutrino mass. E_0 is the energy endpoint energy when neutrino has no mass. The figure is taken from [45].

fits of the energy spectrum [47]. The present high precision mass difference is measured by the Penning trap experiment at FSU and is $\Delta m = 18592.01(7)$ eV/c^2 [16]. To reach the final sensitivity goal of KATRIN, the uncertainty of the involved mass values and the mass difference should be lowered such that $\delta(\Delta m) < 20$ meV/c^2. This means that the relative precision of the masses should be better than 8 ppt. With few technical upgrades and improvements in the measurement technique, this seems achievable at the LIONTRAP experiment.

1.2 Measuring light ion masses

The measurement of light ions comes with various challenges due to their relatively small signals and large systematic shifts due to special relativity resulting from their low rest mass. Accordingly, the LIONTRAP experiment is designed, optimized, and dedicated for mass measurements of light ions. The elements with mass number $A \leq 4$ are primary candidates measured at LIONTRAP with a relative precision of part per trillion. The main measurement principle and goal involves a high-precision comparison of cyclotron frequencies $\omega_c = {}^{qB}/_{m}$ of an ion of interest and a reference ion with their respective charge-to-mass ratio (q/m) in the same magnetic field. This thesis will discuss the experiment's details and the mass measurement of light ions.

1.3 Content of this thesis

The thesis framework is as follows: In Chapter 1 until now, I have briefly introduced the importance of high-precision mass measurements, especially the masses of light ions. Chapter 2 discusses the principles of the measurement tool used in this work, which is a Penning trap. In Chapter 3, the non-destructive detection and high-precision measurement techniques of the eigenfrequencies are broadly described. The state-of-the-art experimental setup and a production technique for gaseous atoms, which was developed during this thesis work, are introduced in Chapter 4. Following this, Chapter 5 outlines preparations before mass measurements and the assessment of several systematic effects. The principle of mass measurements, the measurement procedures, the determination of the helium-4 mass, and a comparison to other high-precision mass measurements of helium-4 and the literature value are reported in Chapter 6. The limitations of the mass measurement during this work and potential improvement to achieve better precision in future measurements are also presented in Chapter 6. A summary and prospects for our experiment form the last part of this thesis in Chapter 7.

2. Physics of Penning traps

Ion traps are pivotal tools in various research fields, from studies in atomic physics to quantum computing. High-precision measurements of mass, g-factor, and studies of spectral lines are some excellent examples of ion trap measurements that can be used to test the predictions of quantum-electrodynamics and search for new physics beyond the Standard Model.

Trapping of ions makes it possible to study them in a controlled environment for long observation times. One could trap an ion by confining it in a space where there is a three-dimensional (3D) potential well in which an ion would achieve a stable equilibrium created by electric fields or magnetic fields or both. Earnshaw's theorem forbids the possibility of trapping charges [statically] in purely electrostatic fields, $\vec{E}$, or purely magnetic fields, $\vec{B}$, [48]. In other words, in a source free-region, the charged particles cannot be confined in a stable stationary equilibrium with static electric or magnetic fields. This can also be understood from Maxwell's formulation of electromagnetic field theory [49], which states that in a region of space that is divergence-free and satisfies the Laplace equation, there only exist saddle points, but no stable equilibrium is possible. Nevertheless, this is resolved by using either oscillating quadrupole electric potential, known as the Paul trap [50, 51], or by the superposition of a magnetostatic and an electrostatic field [52, 53, 54], known as the Penning trap.

At LIONTRAP, we use a Penning trap to isolate, store and manipulate a single ion in an almost perturbation-free environment to perform high-precision mass measurements. To perform such measurements with single ions, Penning traps are advantageous because the confining fields are static, which means that the amplitudes of micromotion are very low, and thus no micromotion-induced AC Stark shifts of the ion's energy levels. Furthermore, the static magnetic field generated by a superconducting magnet is uniform and stable, allowing a very precise cyclotron frequency measurement, thereby making it apt for mass spectrometry.

In this chapter, I will discuss the physics of Penning traps, beginning with section 2.1, where an ideal Penning trap is presented. Later in section 2.2, I will describe a real Penning trap considering trap imperfections and other real-life non-idealities.

2.1 Ideal Penning trap

In a Penning trap, a homogeneous magnetic field, $\vec{B} = B_0\vec{e_z}$, in the axial direction confines the ion in the radial plane, perpendicular to the magnetic field lines. In a pure homogeneous magnetic field, the particle orbits around the magnetic field lines with the cyclotron

frequency, also called free-cyclotron frequency,

$$\omega_c = \frac{qB_0}{m}, \tag{2.1}$$

where m and q are the mass and charge of the ion, respectively.

The confinement of the ion along the magnetic field, i.e., in the axial direction, is achieved by an electrostatic quadrupole potential. The equipotential surfaces of an ideal quadrupolar field are hyperboloids of revolution. Thus the ideal quadrupolar potential can be achieved using three hyperboloidal electrodes (see Fig. 2.1), a ring, and two endcap electrodes that extend to infinity, whose equations in the cylindrical coordinates (z, r) are

$$\frac{r^2}{r_0^2} - \frac{z^2}{z_0^2} = \pm 1, \tag{2.2}$$

where the + and - signs on the right-hand side of the Eq. (2.2) correspond to ring and endcap electrodes, respectively. z_0 is half the distance between the two endcaps, and r_0 is the inner radius of the ring such that $r_0 = \sqrt{2}z_0$ [55][56].

The electrostatic quadrupole potential is given by

$$\Phi(z, r)_{\text{ideal}} = \frac{U_r C_2}{2d_{\text{char}}^2}\left(z^2 - \frac{r^2}{2}\right), \tag{2.3}$$

where U_r is the trapping voltage supplied to the ring electrode, $r = \sqrt{x^2 + y^2}$ is the distance from the z-axis and $d_{\text{char}} = \sqrt{\frac{1}{2}\left(z_0^2 + \frac{r_0^2}{2}\right)}$ is the characteristic trap dimension that depends on z_0 and r_0. C_2 is a dimensionless electric potential coefficient dependent on the geometry of the electrodes. The perfect quadrupole potential created by ideal hyperbolic electrodes

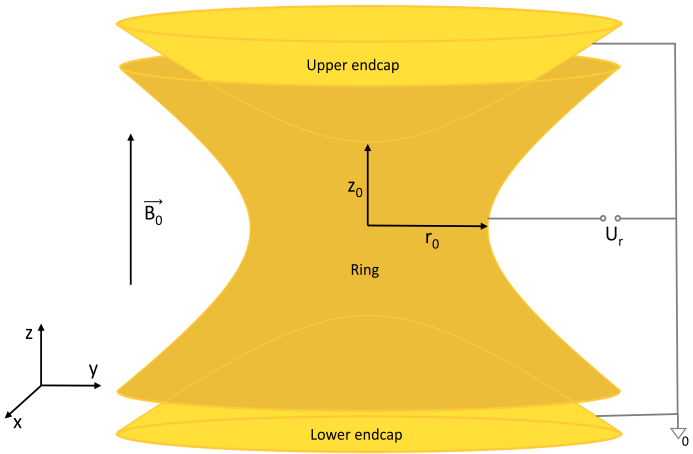

Figure 2.1. The sketch represents a hyperbolic Penning trap with a ring electrode and two endcaps placed in a magnetic field. The radius r_0 and the distance between the endcaps $2z_0$ describe the trap geometry. This sketch depicts truncated electrodes, but ideally, they would have infinite lengths to create a perfect quadrupolar potential.

corresponds to $d_{\text{char}} = z_0$, and $C_2 = 1$ [55].

2.1.1 Motion of the particle

Due to the electrostatic potential, the ion experiences a confining force in the axial direction leading to a harmonic oscillation. However, in the radial directions, the ion experiences a repulsive force directed outwards, but as a consequence of the magnetic field along the axial direction, the ion is returned into a cyclotron-type orbit resulting in a modified cyclotron motion. The combination of the outwards-directed electric field and the axial magnetic field causes a circular $\vec{E} \times \vec{B}$ drift motion around the trap center, the so-called magnetron motion. Hence, the ion exhibits three eigenmotions: harmonic oscillation along the z-axis and a superposition of the modified cyclotron and magnetron motion in the radial plane (see Fig. 2.2). In the following, I will discuss the classical, non-relativistic motion of the particle as we typically work with ions cooled to cryogenic temperatures. The relativistic corrections will be discussed in section 3.4.

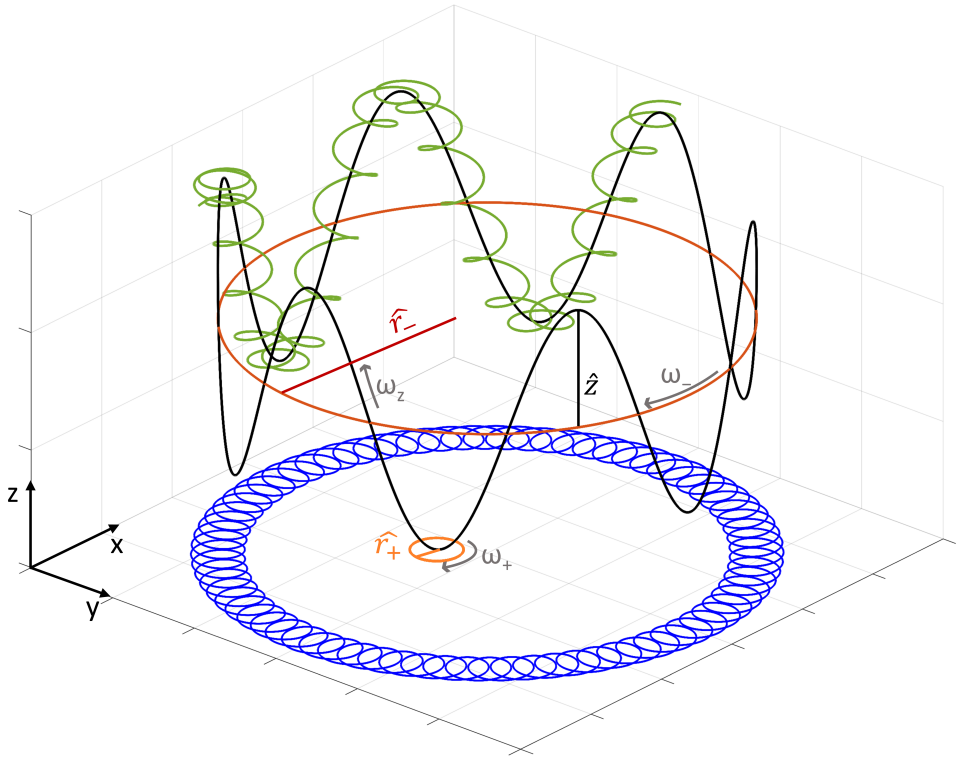

Figure 2.2. An illustration of particle trajectory in a Penning trap described by the superposition of three eigenmotions. The small orange circle indicates the fast cyclotron motion with amplitude r_+ and frequency ω_+. The large red circle indicates the slowest magnetron motion with amplitude r_- and frequency ω_-. The superposition of these two motions is projected onto the xy-plane in blue. The black line depicts the axial motion with amplitude $\hat{z}$ and frequency ω_z. The green line shows the superposition of all three eigenmotions.

A charged particle q with velocity $\vec{v}$ in electromagnetic fields experiences the Lorentz force

$$\vec{F} = q(\vec{E} + \vec{v} \times \vec{B}). \tag{2.4}$$

The negative gradient of the electrostatic potential defined in Eq. (2.3), $\vec{E} = -\vec{\nabla}\Phi$, is

$$\vec{E} = \frac{U_r C_2}{2d_{\text{char}}^2} \begin{pmatrix} x \\ y \\ -2z \end{pmatrix}. \tag{2.5}$$

The homogeneous magnetic field, as mentioned earlier in this chapter, is given by

$$\vec{B} = B_0 \vec{e_z}. \tag{2.6}$$

Newton's law

$$\vec{F} = m\vec{a} = m\dot{\vec{v}}, \tag{2.7}$$

where $\vec{a}$ is the acceleration and m is the rest mass of the particle, along with Eq. (2.4), Eq. (2.5) and Eq. (2.6) can be used to derive the classical equations of motion of a trapped particle:

$$\begin{pmatrix} \ddot{x} \\ \ddot{y} \\ \ddot{z} \end{pmatrix} = \frac{qB_0}{m} \begin{pmatrix} \dot{y} \\ -\dot{x} \\ 0 \end{pmatrix} + \frac{qU_r C_2}{2md_{\text{char}}^2} \begin{pmatrix} x \\ y \\ -2z \end{pmatrix}. \tag{2.8}$$

From Eq. (2.8) and Eq. (2.1)

$$\ddot{x} - \omega_c \dot{y} - \frac{1}{2}\omega_z^2 x = 0, \tag{2.9a}$$

$$\ddot{y} + \omega_c \dot{x} - \frac{1}{2}\omega_z^2 y = 0, \tag{2.9b}$$

$$\ddot{z} + \omega_z^2 z = 0, \tag{2.9c}$$

where we define the frequency of the harmonic oscillation of the ion in the axial direction as:

$$\omega_z = \sqrt{\frac{qU_r C_2}{md_{\text{char}}^2}}. \tag{2.10}$$

Solving the equations of motion (Eq. (2.9)) [57, 58] yields the modified cyclotron motion with frequency ω_+ and radius r_+ and magnetron motion with frequency ω_- and radius r_-,

$$\omega_\pm = \frac{1}{2}\left(\omega_c \pm \sqrt{\omega_c^2 - 2\omega_z^2}\right). \tag{2.11}$$

$$\begin{pmatrix} x(t) \\ y(t) \end{pmatrix} = r_+ \begin{pmatrix} \cos(\omega_+ t + \phi_+) \\ -\sin(\omega_+ t + \phi_+) \end{pmatrix} + r_- \begin{pmatrix} \cos(\omega_- t + \phi_-) \\ -\sin(\omega_- t + \phi_-) \end{pmatrix} \tag{2.12}$$

The term under the square root in Eq. (2.11) must be real-valued to give bound solutions to

the equations and thus sets the stability criterion for the trap:

$$\omega_c^2 - 2\omega_z^2 > 0 \Rightarrow B_0 > \sqrt{\frac{2mU_rC_2}{qd_{\text{char}}^2}}. \tag{2.13}$$

In a strong magnetic field and a comparably weak electric field, the eigenfrequencies have the hierarchy

$$\omega_c > \omega_+ \gg \omega_z \gg \omega_-. \tag{2.14}$$

In an ideal Penning trap the eigenfrequencies are also related as

$$\omega_c = \omega_+ + \omega_-, \tag{2.15}$$

$$\omega_z^2 = 2\omega_+\omega_-, \tag{2.16}$$

$$\omega_c^2 = \omega_+^2 + \omega_z^2 + \omega_-^2. \tag{2.17}$$

Eq. (2.15) and Eq. (2.16) only remain valid for an ideal Penning trap, whereas Eq. (2.17), known as the invariance theorem by Brown and Gabrielse [58], holds for certain deviations from the ideal trap characteristics which will be discussed in detail in section 2.2.4.

2.1.2 Energies of the eigenmodes

The total energy (potential energy + kinetic energy), $E_{\text{tot}} = E_{\text{pot}} + E_{\text{kin}}$, of the particle is defined as [58, 59]:

$$\begin{aligned} E_{\text{tot}} = &\left(\frac{1}{2}m\omega_z^2\hat{z}^2\right)_{E_z(pot,kin)} + \left(\frac{1}{2}m\omega_+^2 r_+^2\right)_{E_+(kin)} + \left(-\frac{1}{2}m\omega_+\omega_- r_+^2\right)_{E_+(pot)} \\ &+ \left(\frac{1}{2}m\omega_-^2 r_-^2\right)_{E_-(kin)} + \left(-\frac{1}{2}m\omega_+\omega_- r_-^2\right)_{E_-(pot)}. \end{aligned} \tag{2.18}$$

The energy associated with each eigenmode is then described as :

$$\text{Axial mode energy, } E_z = \frac{1}{2}m\omega_z^2\hat{z}^2, \tag{2.19}$$

$$\text{Modified cyclotron mode energy, } E_+ = \frac{1}{2}m\omega_+(\omega_+ - \omega_-)r_+^2 \approx \frac{1}{2}m\omega_+^2 r_+^2, \tag{2.20}$$

$$\text{Magnetron mode energy, } E_- = -\frac{1}{2}m\omega_-(\omega_+ - \omega_-)r_-^2 \approx -\frac{1}{4}m\omega_z^2 r_-^2 \approx -\frac{1}{2}m\omega_+\omega_- r_-^2, \tag{2.21}$$

where $\hat{z}$, r_+, and r_- are the amplitudes of the corresponding motions and the assumption that $\omega_+ \gg \omega_-$ and Eq. (2.16) are used.

Kinetic energy dominates the modified cyclotron mode's energy, whereas the magnetron mode's energy is dominated by potential energy, which results in negative magnetron energy. The electrostatic confining potential pushes the ion outward as it is repulsive in the radial

direction, thus making the slow magnetron mode metastable. This means that an increase in magnetron radius leads to decreased magnetron energy. The total energy of the particle in an ideal Penning trap can also be expressed in quantum mechanical terms as the sum of three independent harmonic oscillators,

$$E_{\text{tot}} = \hbar|\omega_+|\left(n_+ + \frac{1}{2}\right) + \hbar|\omega_z|\left(n_z + \frac{1}{2}\right) - \hbar|\omega_-|\left(n_- + \frac{1}{2}\right), \tag{2.22}$$

where $\hbar$ is reduced Planck's constant and n_k are the quantum numbers usually $> 10^5$, which results from typical ion energies at our trap. This is detailed in section 3.4 and will justify the classical treatment of the ions' motion.

2.2 Real Penning trap

A real Penning trap deviates from an ideal Penning trap described so far. Some of the imperfections that occur in reality are:

- **Geometric imperfections**: The trap electrodes, in reality, are truncated and have a finite size, unlike the ideal hyperbolic electrodes with infinite lengths. The hyperbolic electrodes have the disadvantage that their geometry limits optical and physical access to the trap's center. Thus, microwave or optical excitations or the transfer of ions into/between the traps would necessitate holes in the electrodes. These disadvantages are resolved by using cylindrical electrodes for the Penning trap [60], as in our experiment (details in chapter 4). In any case, machining imperfections and limited manufacturing precision lead to imperfections in the design of the electrodes. Furthermore, the electrodes are sometimes split to introduce excitations in the trap.
- **Electric field imperfections**: The voltages applied on the electrodes deviate and fluctuate from the ideal settings due to imperfections in the voltage source ($\frac{\delta U}{U} \sim 10^{-7}$ in our experiment). Due to deviations from the ideal geometry of the electrodes, the electrostatic potential is not perfectly quadrupolar and has higher-order multi-polar contributions. The electrostatic potentials could also suffer an ellipticity and cause the radial components of the electric field to be stronger in one direction than the other. There are also patch potentials due to electrically isolated patches on the surfaces of the electrode, which can be caused by imperfect surfaces of the electrode, deposits of rest gases on the electrode surfaces, charges accumulated on the dielectric materials in the trap system, and any impurities or varying composition of the material of the electrodes. Changes in the work function of the electrode surfaces, for example, due to different crystal structures and thus crystal directions, can also lead to patch potentials causing a non-uniform electrostatic potential.
- **Magnetic field imperfections**: A continuous decay in the magnetic field of the superconducting magnet is expected due to flux creep in the superconducting coil. How-

ever, a notable change would only happen in timescales in the order of years for the present-day magnets. Any ferromagnetic or paramagnetic materials in or near the magnetic field get magnetized and cause disturbances to the magnetic field. The residual magnetic permeability of the trap and surrounding materials fluctuates due to pressure and temperature fluctuations, consequently affecting the magnetic field. The change in liquid helium and nitrogen levels in the reservoirs of the magnet could lead to temperature fluctuations.

- **Misalignment**: Misalignment between the symmetry axis of the electrodes or the electrostatic potential and the magnetic field axis brings deviations from the ideal case. During the assembly of electrodes, misalignment and displacements are possible.

These imperfections, inhomogeneities, fluctuations, and misalignments make the oscillation frequencies of trapped ions depend upon the amplitudes of motion, causing systematic shifts in the eigenfrequencies, which must be carefully identified. The cylindrical Penning trap is inherently cylindrically-symmetric; thus, the electrostatic potential and imperfections also respect this symmetry (with the exception of the patch potentials). The following sections are a description of such cylindrically-symmetric imperfections in the electrostatic and magnetic fields.

2.2.1 Frequency shifts due to electrostatic anharmonicity

A ring and two endcaps can achieve a crude quadrupole potential in a simple ion trap, but these cannot be used for high-precision measurements. The quadrupole potential can be improved by adding correction electrodes and the right choice of the length and length-to-radius ratios of all the electrodes. The work presented in this thesis is performed using a seven electrodes trap. Hereafter, any description of a trap used for this work would refer to an open endcap seven-electrode cylindrical Penning trap (section 4.2.2).
The general form of the electrostatic potential at the center of the trap [59, 61] described in Eq. (2.3) can be expressed as :

$$\Phi(r,z) = \frac{U_r}{2}\sum_{n=0}^{\infty}\frac{C_n}{d_{\text{char}}^n}\sum_{k=0}^{n/2}(-4)^{-k}\frac{n!}{(n-2k)!(k!)^2}z^{n-2k}r^{2k} \tag{2.23}$$

where r and z are the cylindrical coordinates. The series expansion of electric potential can be rewritten as follows:

$$\begin{aligned}\Phi(z,r) = \frac{U_r}{2}\Bigg[&C_0 + \frac{C_1 z}{d_{\text{char}}} + \frac{C_2}{d_{\text{char}}^2}\left(z^2 - \frac{r^2}{2}\right)\\ &+ \frac{C_3}{d_{\text{char}}^3}\left(z^3 - \frac{3}{2}zr^2\right) + \frac{C_4}{d_{\text{char}}^4}\left(z^4 - 3z^2r^2 + \frac{3}{8}r^4\right)\\ &+ \frac{C_5}{d_{\text{char}}^5}\left(z^5 - 5z^3r^2 + \frac{15}{8}zr^4\right) + \frac{C_6}{d_{\text{char}}^6}\left(z^6 - \frac{15}{2}z^4r^2 + \frac{45}{8}z^2r^4 - \frac{5}{16}r^6\right) + \ldots.\Bigg]\end{aligned} \tag{2.24}$$

In the above equation (Eq. (2.24)), there are both even and odd C_n coefficients that describe the anharmonicity of the electric field. The following two subsections discuss the frequency shifts associated with these coefficients.

2.2.1.1 Even order anharmonicity coefficients

The first even coefficient $\mathbf{C}_0$ is an unobservable constant that does not influence the trapped particle and thus can be ignored. The next coefficient $\mathbf{C}_2$ is responsible for the desired electrostatic quadrupole potential as described in Eq. (2.3). The value of this dimensionless parameter depends on the geometry of the trap electrodes. For example, the ideal hyperbolic traps have C_2 = 1 and C_n = 0 for $n \neq 2$ whereas cylindrical traps have $C_2 \approx$ -0.5. The dominant electrostatic anharmonicity results in non-zero higher-order even coefficients, $\mathbf{C}_4$, $\mathbf{C}_6$, $\mathbf{C}_8$, and so on. These coefficients lead to energy-dependent shifts of the oscillating frequencies. As the order of the coefficient increases, the influence on the eigenfrequencies is lower due to the typical small amplitudes of the particle compared to the trap dimensions.

The first-order frequency shifts due to the leading order anharmonicity described by the even order coefficient C_n, n = 4,6..., in a symmetric potential are discussed in [59, 62]. The frequency shifts due to C_4 and C_6 can be summarized as follows:
Shifts in axial frequency ω_z are

$$\frac{\Delta\omega_z}{\omega_z} = \frac{C_4}{C_2}\frac{3}{4d_{\text{char}}^2}(\hat{z}^2 - 2r_+^2 - 2r_-^2), \tag{2.25}$$

$$\frac{\Delta\omega_z}{\omega_z} = \frac{C_6}{C_2}\frac{15}{16d_{\text{char}}^4}(\hat{z}^4 + 3r_+^4 + 3r_-^4 - 6r_+^2\hat{z}^2 - 6r_-^2\hat{z}^2 + 12r_+^2r_-^2), \tag{2.26}$$

Shifts in the radial frequencies ω_+, and ω_- are

$$\Delta\omega_\pm = \mp\frac{C_4}{C_2}\frac{3}{2d_{\text{char}}^2}\frac{\omega_+\omega_-}{\omega_+ - \omega_-}(2\hat{z}^2 - r_\pm^2 - 2r_\mp^2), \tag{2.27}$$

$$\Delta\omega_\pm = \mp\frac{C_6}{C_2}\frac{15}{8d_{\text{char}}^4}\frac{\omega_+\omega_-}{\omega_+ - \omega_-}(3\hat{z}^4 + r_\pm^4 + 3r_\mp^4 - 6r_\pm^2\hat{z}^2 - 12r_\mp^2\hat{z}^2 + 6r_+^2r_-^2). \tag{2.28}$$

For a close-to-ideal quadrupole potential, as many as possible $C_{n>2}$ coefficients should be nulled. The geometry of the seven-electrode Penning trap (see section 4.2.2 and [63]) and the voltages supplied to the correction electrodes at LIONTRAP is chosen to produce a highly harmonic potential with the lowest order anharmonicity coefficients tuned out. For a fixed radius of the electrodes and identical gap size between the electrodes, a highly harmonic electrical trapping potential in a cylindrical seven-electrode Penning trap can be attained by manipulating 5 degrees of freedom: the length of the ring electrode (l_r), lengths of the correction electrodes (l_{C1}, l_{C2}) and voltages on the correction electrodes (U_{C1}, U_{C2}). These parameters are chosen such that $C_4 = C_6 = C_8 = C_{10} = 0$ [63]. However, due to imperfections in manufacturing and assembly, these coefficients are not tuned out completely.

The lengths of the electrodes are fixed by design, so the remaining two degrees of freedom, which are the correction and the ring voltages, can be adjusted to tune C_4 = C_6 = 0, even in the presence of machining imperfections. The voltage ratio of correction to ring electrodes, which can be adjusted online, is known as the Tuning Ratio. The remaining coefficients C_8, C_{10}, C_{12},... have to be accepted as they turn out after manufacturing. Due to our robust trap design, the value of C_8 remains small. The effects of the remaining anharmonicities on the eigenfrequencies are negligible. Such a trap with leading order anharmonicities nulled is described as a **compensated** trap. Another important criterion that has to be fulfilled for the practical operation of the trap is **orthogonality**. That is, the even coefficient C_2 and, consequently, the axial frequency of the ion should be independent of the correction voltages. C_2 can be expressed in terms of the two correction voltages as

$$C_2 = D_{2,1}\frac{U_{C1}}{U_r} + D_{2,2}\frac{U_{C2}}{U_r} + E_2, \tag{2.29}$$

where $\frac{U_{C1}}{U_r}$ = TR_1 and $\frac{U_{C2}}{U_r}$ = TR_2 are the Tuning Ratios. At our seven-electrode trap, the correction voltages are adjusted by the same factor to ensure that the axial frequency remains unaffected. Thus, the trap achieves a combined orthogonality criterion,

$$D_2^{comb} = D_{2,1}\frac{U_{C1}}{U_r} + D_{2,2}\frac{U_{C2}}{U_r} = 0. \tag{2.30}$$

This combined orthogonality feature makes it possible to tune the trap online (in situ). The compensation or optimization process of the trap is detailed in section 5.2.

2.2.1.2 Odd order anharmonicity coefficients

The odd-order coefficients are nominally null and result only from machining and voltage imperfections. They do not produce first-order shifts. The typically very small effects of the odd-odd and odd-even combinations are discussed in this section. The odd coefficients contribute to frequency shifts in second and higher order.

The first odd coefficient, C_1, influences the center of the axial oscillation. The potential $\phi_1 \propto z$ does not depend on the radial component r. Typically, we define C_1 = 0 because we develop the potential around the trap center, where the cold particle sits in the absence of magnetic or other forces. If the potential is developed around a point that is not the trap center, $C_1 \neq 0$ and there will be frequency shifts resulting from $C_1 \cdot C_n (n \geq 3)$. As we always choose to develop around the minimum C_1 = 0. Nevertheless, there can be shifts in the axial equilibrium position because of which the ion could be exposed to a different magnetic field due to possible inhomogeneities. This brings a variation in the free cyclotron frequency and thus the radial eigenfrequencies. Such shifts in equilibrium position could arise from magnetic moment combined with magnetic field gradients, gravity, or any change in the electric field experienced by the ion. These have to be treated, if not negligible. Usually, such ef-

fects are suppressed in our trap; for example, there are patch potentials present on the trap electrodes, which means by changing the trapping voltage, we could change the electric field experienced by the ion, thus changing the electrostatic minimum. This effect is reduced by the usage of varactor [22] or two tank circuits [21], allowing us to use the same trapping potential for different axial frequencies.

The electrostatic potential experienced by the ion can be asymmetric in certain instances. The terms C_k, where $k = 2n + 1, n > 0$, are typically correlated with such voltages on the electrodes that do not fulfill mirror-symmetry. Referring to Eq. (2.24), the next leading order odd anharmonicity coefficient of the potential is C_3. The equations of motion in such an altered potential can be solved analytically [64]. The positional shift and the corresponding frequency shift when the shifted equilibrium position is $z(t) = \hat{z}\cos((\omega_z + \Delta\omega_z)t) + \Delta z$ [30, 59, 65] can be summarized as follows:
The positional shift is

$$\Delta z = -\frac{3}{4}\frac{C_3}{C_2 d_{\text{char}}}\hat{z}^2 + \frac{3}{4}\frac{C_3}{C_2 d_{\text{char}}}r_{\pm}^2. \tag{2.31}$$

The electrostatic potential needs to be developed around the new equilibrium position. Thus a series expansion of the potential around the new equilibrium of motion gives the relative frequency shift:

$$\frac{\Delta\omega_z}{\omega_z} \approx -\frac{15}{16}\frac{C_3^2}{C_2^2 d_{\text{char}}^2}\hat{z}^2 + \frac{9}{8}\frac{C_3^2}{C_2^2 d_{\text{char}}^2}r_{\pm}^2. \tag{2.32}$$

The overall consequence of an asymmetric potential is an increase in the oscillation period about the z-axis and, as a result, a decrease in the frequency justifying the negative sign of the frequency shift for $\hat{z}$ [59].

Notably, the frequency shifts due to the odd coefficients are of second order in the coefficient. In combination with the individual C_{odd} to be nominally null, this justifies why these coefficients are often neglected when optimizing a trap. During optimization, the dependence of the axial frequency on the magnetron radius is studied, and the tuning ratio is chosen such that the shift in the axial frequency is minimal for the largest range of magnetron radii, which implies that the even coefficients and especially C_4 are minimized ($C_4 \approx 0$). However, the scaling of the frequency shift due to C_3^2 for the radial amplitudes is similar to that of the neighboring even coefficient C_4 (Eq. (2.25)). Thus when optimizing the trap by studying the axial frequency shifts as a function of r_-^2, one does not attain $C_4 \approx 0$, but the combination of C_4 and C_3 is nulled. This implies that either both shifts must cancel each other or both are nulled. Combining the $r_{\pm}^2$ terms of Eq. (2.25) and Eq. (2.32), we can evaluate

$$C_4 = \frac{3}{4}\frac{C_3^2}{C_2}. \tag{2.33}$$

However, in this case the axial frequency shifts due to C_3^2 (Eq. (2.32)) and C_4 (Eq. (2.25)) for the axial amplitudes $\hat{z}$ are not zero.

When an asymmetric potential is applied to the trap intentionally to shift the position of

the ion or the potential is asymmetric unintentionally, the effects due to odd coefficients are more prominent, and then special care needs to be taken to avoid significant errors.

Combinations of two anharmonic coefficients of the potential can also produce frequency shifts. Even-odd (C_4C_3), even-even (C_4C_6), and odd-odd (C_3C_5) cross-terms and shifts due to these anharmonicities are discussed in detail in [59, 66].

2.2.2 Frequency shifts due to magnetostatic inhomogeneity

The magnetic field of the superconducting magnet is not perfectly homogeneous or uniform in reality. Some of the reasons are detailed in the introduction of section 2.2. These imperfections in the magnetic field also lead to energy-dependent frequency shifts.
The magnetic field expanded as Legendre series in the cylindrical coordinates is

$$\begin{aligned} B(z,r) = B_0\hat{e}_z + B_1\left(z\hat{e}_z - \frac{r}{2}\hat{e}_r\right) + B_2\left((z^2 - \frac{r^2}{2})\hat{e}_z - zr\hat{e}_r\right) \\ + B_3\left(\left(z^3 - \frac{3}{2}zr^2\right)\hat{e}_z + \left(-\frac{3}{2}z^2r + \frac{3}{8}r^3\right)\hat{e}_r\right) \\ + B_4\left(\left(z^4 - 3z^2r^2 + \frac{3}{8}r^4\right)\hat{e}_z + \left(-2z^3r + \frac{3}{2}zr^3\right)\hat{e}_r\right)... \end{aligned} \tag{2.34}$$

where $\hat{e}_z$ and $\hat{e}_r$ are the unit vectors in the axial and radial directions. The strong axial field component usually suppresses the strength of the radial field component of the magnetic field, but the relation of the axial magnetic field to the axial and radial coordinates leads to frequency shifts that are discussed further in this section.

An ion in a circular motion (magnetron and cyclotron mode) on a plane perpendicular to the magnetic field is equivalent to an electric current through a circular coil:

$$I = \frac{q}{t} = q\frac{\omega_\pm}{2\pi}. \tag{2.35}$$

This produces an orbital magnetic moment

$$\begin{aligned} \left|\mu_z^{(\pm)}\right| &= I\pi r_\pm^2 \\ \Rightarrow \mu_z^{(\pm)} &= -\frac{q}{2}\omega_\pm r_\pm^2. \end{aligned} \tag{2.36}$$

The potential energy associated with such a magnetic moment is

$$U_{mag} = -\mu_z^{(\pm)} \cdot \vec{B} \tag{2.37}$$

causing an additional force in the z-direction as the ion tries to minimize its total energy

$$F_z^{(\mu)} = -\frac{\partial U_{mag}}{\partial z} = \mu_z^{(\pm)}\frac{\partial B}{\partial z}. \tag{2.38}$$

The axial equation of motion hence becomes

$$\ddot{z} + \omega_z^2 z - \frac{\mu_z^{(\pm)}}{m}\frac{\partial B}{\partial z} = 0. \tag{2.39}$$

The derivative vanishes for a homogeneous magnetic field, and there is no additional force in the axial direction. The lower-order terms B_1 (linear) and B_2 (quadratic) are the most important magnetic field perturbations.

Considering the odd-order magnetostatic inhomogeneity, B_1 (Eq. (2.34)), the equation of motion (Eq. (2.39)) will be

$$\ddot{z} + \omega_z^2 z - \frac{\mu_z^{(\pm)}}{m}B_1 = 0. \tag{2.40}$$

The additional term in the axial equation of motion results in an equilibrium position shift

$$\Delta z = \frac{\mu_z B_1}{m\omega_z^2} = -\frac{\omega_c\omega_\pm}{2\omega_z^2}\frac{B_1}{B_0}r_\pm^2, \tag{2.41}$$

just like the odd anharmonicity coefficients. The contribution of B_1 indicates that the magnetic field is not homogeneous. In the shifted position, the ion experiences a different magnetic field and, thus, a shift in the radial frequencies. The magnetic moment related to modified cyclotron mode translates into a relative shift in the magnetic field $\frac{\Delta B}{B} \simeq \frac{B_1}{B_0}\Delta z = \frac{\Delta\omega_+}{\omega_+}$. Thus,

$$\frac{\Delta\omega_+}{\omega_+} = -\frac{\omega_c\omega_+}{2\omega_z^2}\left(\frac{B_1}{B_0}\right)^2 r_+^2. \tag{2.42}$$

As in the case of electrostatic anharmonicity coefficients, the odd magnetic inhomogeneity terms also only produce frequency shifts in the second order.

The next interesting magnetic inhomogeneity term is the even coefficient B_2. The B_2 term changes the equation of motion (Eq. (2.39)) as

$$\ddot{z} + \omega_z^2 z - \frac{\mu_z^{(\pm)}}{m}2B_2 z = 0. \tag{2.43}$$

This additional term adds up with the electrostatic force and generates an axial frequency shifted by

$$|\Delta\omega_z| = \frac{\mu_z^{(\pm)}B_2}{\omega_z m} \tag{2.44}$$

The resultant relative axial frequency shift is

$$\frac{\Delta\omega_z}{\omega_z} = \frac{\omega_+ + \omega_-}{\omega_+\omega_-}\frac{B_2}{4B_0}(r_-^2\omega_- + r_+^2\omega_+), \tag{2.45}$$

Similarly, the relative shift in the modified cyclotron and magnetron modes are

$$\frac{\Delta\omega_+}{\omega_+} = \frac{\omega_+ + \omega_-}{\omega_+ - \omega_-}\frac{B_2}{2B_0}\left(\hat{z}^2 - r_+^2 - r_-^2\left(1 + \frac{\omega_-}{\omega_+}\right)\right), \tag{2.46}$$

and

$$\frac{\Delta\omega_-}{\omega_-} = -\frac{\omega_+ + \omega_-}{\omega_+ - \omega_-}\frac{B_2}{2B_0}\left(\hat{z}^2 - r_-^2 - r_+^2\left(1 + \frac{\omega_+}{\omega_-}\right)\right). \tag{2.47}$$

A superconducting shim coil has been implemented around the trap chamber to minimize B_2 in situ (section 4.7). To measure B_2, the axial frequency shift as a function of various modified cyclotron radii r_+ is studied. Details of such a measurement will be discussed in section 5.3.

2.2.3 Frequency shifts due to a combination of electric field and magnetic field imperfections

The electrostatic anharmonicity combined with magnetostatic inhomogeneity can also cause frequency shifts. The leading order odd coefficients of the electric and magnetic field imperfections C_3 and B_1 combined lead to a shift in the axial frequency. Due to B_1, the ion experiences a positional shift (see Eq. (2.41)) in an asymmetric electrostatic potential due to C_3. A harmonic oscillation is then developed in this new equilibrium position. A series expansion of the potential at this shifted position, assuming $r_\pm \gg \hat{z}$, leads to

$$\frac{\Delta\omega_z}{\omega_z} = -\frac{3B_1}{4B_0}\frac{C_3}{C_2}\frac{\omega_\pm\omega_c}{\omega_z^2 d_{\text{char}}}r_\pm^2. \tag{2.48}$$

When considering r_+ to be dominant and assuming $\omega_+ \approx \omega_c$ and $\omega_z^2 = 2\omega_+\omega_-$, the above equation can be rewritten as:

$$\frac{\Delta\omega_z}{\omega_z} = -\frac{3B_1}{8B_0}\frac{C_3}{C_2}\frac{\omega_+}{\omega_-}\frac{r_+^2}{d_{\text{char}}}. \tag{2.49}$$

Comparing the terms scaling with r_+^2 in Eq. (2.45) and Eq. (2.49), we get

$$B_2 = -\frac{3}{2}\frac{B_1 C_3}{C_2 d_{\text{char}}}. \tag{2.50}$$

Therefore, the uncertainty in C_3 and B_1 directly influences the limit to which the magnetic field can be optimized.

The combination of frequency shifts due to B_2 (Eq. (2.49)) and leading order electrostatic anharmonicity C_4 (Eq. (2.25)) that scale with r_+^2 is

$$\frac{\Delta\omega_z}{\omega_z} = \left(\frac{B_2}{4B_0}\frac{\omega_+}{\omega_-} - \frac{3}{2}\frac{C_4}{C_2 d_{\text{char}}^2}\right)r_+^2. \tag{2.51}$$

When the optimized condition of $\Delta\omega_z = 0$ for any radius r_+ is attained

$$B_2 = \frac{6C_4}{C_2 d_{\text{char}}^2} \frac{\omega_-}{\omega_+}. \tag{2.52}$$

This sets another limit to which the magnetic field can be optimized. In other words, the limit to which B_2 can be nulled depends on the uncertainty in the electrostatic anharmonicity, C_4.

2.2.4 Frequency shifts due to misalignment and ellipticity: invariance theorem

When the trap system is placed in the magnetic field, the trap axis or the z-axis of the electrostatic quadrupole potential should be aligned with the z-axis of the magnetic field. However, a minimal tilt θ between these axes is unavoidable. Furthermore, the geometric and mechanical flaws of the trap lead to distortion of the azimuthal symmetry of the quadrupole electric field, which can be modeled to first order as an effective ellipticity ϵ. These are both inevitable lowest-order imperfections of a real Penning trap because the frequency shift associated with them appears even for a cold particle. Higher-order imperfections will likely scale with energy and thus drop out when cooling better or extrapolating to zero energy. These frequency shifts are derived in [67, 68].

The free cyclotron frequency can be extracted as $\omega_c = \omega_+ + \omega_-$ (Eq. (2.15)), but this equation holds only for an ideal Penning trap and is sensitive to θ and ϵ. In the invariance theorem proposed by Brown–Gabrielse, the shifts arising from misalignment and ellipticity are suppressed completely, and the free cyclotron frequency can be extracted from all three eigenfrequencies in the trap as $\omega_c^2 = \omega_+^2 + \omega_z^2 + \omega_-^2$ (Eq. (2.17)) [58, 68]. On comparing Eq. (2.15) and Eq. (2.17), information about the tilt and the distorted electric field can be extracted [69] as:

$$(\omega_+ + \omega_-) - \sqrt{\omega_+^2 + \omega_z^2 + \omega_-^2} = \omega_- \left(\frac{9}{4}\theta^2 - \frac{1}{2}\epsilon^2 \right) \tag{2.53}$$

More details on the alignment of our trap system and how we tune them are discussed in section 5.5. In this thesis, the free cyclotron frequency of the ion is calculated using the invariance theorem.

3. Frequency measurements and further systematic shifts

The mass measurement technique employed at LIONTRAP is performed with single ions over extended periods, demanding highly sensitive and non-destructive frequency detection and measurement methods. The detection method used and discussed in this chapter relies on image charges induced on the electrodes by the ion. This chapter elaborates on the measurement of axial frequency and how the coupling between radial and axial modes enables the measurement of radial frequencies using an axial detection system. Furthermore, a coherent phase-sensitive detection technique is introduced. Estimating the cyclotron frequency using the invariance theorem necessitates measuring all three eigenfrequencies. Additionally, the chapter provides insights into the techniques used for determining ion temperature and the ion's thermal amplitudes. Systematic shifts resulting from the effects of the image charges and the finite temperature of the ion are also discussed.

3.1 Induced image current detection

When an ion is trapped within a conductive electrode, electrostatic induction leads to the generation of image charges (mirror charges) on the electrode surfaces. Since the trapped ion in a Penning trap is not at rest but moves with its eigenfrequencies, the image charges also move accordingly. The oscillating image charge that moves in and out of the electrode is referred to as image current (AC signal) with a frequency exactly as that of the ion (ideally). The image current is typically in the order of femtoampere and can be converted to a detectable voltage by introducing a high impedance between the electrodes, which is usually done using customized cryogenic and superconducting electronics. The frequency information carried by the current varies depending on the position (and geometry) of the electrodes. For example, the current induced due to the axial motion of the ion can be picked up from the off-center electrodes (in our case, the lower and upper correction electrodes), whereas the radial motion (modified cyclotron) of the ion requires splitting of the electrode to which the detection system is connected (see section 3.2.4). In the following sections, the detection techniques will be explained, corresponding to an axial detection system, which also enables the measurement of all frequencies via suitable mode-couplings.

3.1.1 Detection principle

The current induced on the electrode by a moving point charge is well explained by the Shockley–Ramo theorem. The theorem was formulated by William Shockley [70] and Karl Ramo [71] independently and states that the induced current i_{ind} due to a charge q moving

with a velocity $\vec{v}$ is

$$i_{\text{ind}} = q\vec{v}\frac{\vec{E_0}}{U}. \tag{3.1}$$

Here, E_0 is the electric field of the electrode at the position of the ion when the bias potential of the given electrode is U in the absence of charge (ion), and all the other electrodes are grounded [70, 71, 72]. As mentioned earlier, this section only deals with the axial motion of the ion; thus, the fields and potentials are also discussed in terms of the axial motion of the ion. The electric field at the ion position created by the center ring electrode is zero; thus, the signal is picked up from the off-center correction and/or endcap electrodes (See Fig. 3.1).

The 'effective electrode distance'

$$D = \frac{U}{\vec{E_0}}, \tag{3.2}$$

is the distance between two infinite parallel capacitors, which would pick up an equivalent electric field or image current induced by the ion, just as in a real electrode configuration. Therefore, Eq. (3.1) can be rewritten in terms of D and the harmonic axial oscillation $z(t) = \hat{z}\cos(\omega_z t)$ (assuming constant amplitude) coordinate as

$$i_{\text{ind}}(t) = \frac{q\dot{z}(t)}{D} = -\frac{q\omega_z}{D}\hat{z}\sin(\omega_z t) \Rightarrow i_{\text{ind}}^{\text{rms}} = \frac{q}{D}\frac{\hat{z}}{\sqrt{2}}\omega_z. \tag{3.3}$$

D depends on the actual geometry and the position of the electrode to which the detector is connected and can be determined from Finite Element Method simulations. For the combination of electrodes used for axial detection in our experiment D = 9.6 mm. For a cooled $^4He^{2+}$ ion in our trap (see table. 3.1), this would lead to an induced current of $i_{\text{ind}}^{\text{rms}} = 3\,\text{fA}$.

To detect this tiny current, a trans-impedance amplification is done by a superconducting tank circuit (resonator), designed to be in resonance with the axial frequency of the ion. The large impedance of the resonator converts the current into a measurable voltage

$$u_{\text{ind}}(t) = Z(\omega)i_{\text{ind}}^{\text{rms}}(t). \tag{3.4}$$

3.1.2 Tank circuit - axial resonator

A tank circuit (resonator) is an LC oscillator. Without the inductance, the capacitance of the trap electrodes would cause a low impedance at high frequencies. To compensate, a superconducting coil is connected to this trap capacitance in parallel and is designed to have an inductance L such that the frequency of the resonator matches the axial frequency of the ion. At resonance, the resonator can have a very high impedance, limited by electrical losses. Sometimes additional capacitance is added to adjust the resonance frequency. However, the total capacitance (C) of the resonator also includes the intrinsic capacitance of the coil, the

capacitance of the amplifier, and several parasitic cable capacitances. The finite resistance due to combined component losses of the circuit can be modeled as a parallel resistance (R_p) to the total inductance and capacitance of the resonant circuit. Thus, the total impedance of the resonator circuit is

$$\begin{aligned} Z &= \frac{1}{\frac{1}{i\omega L} + i\omega C + \frac{1}{R_p}} \\ \Rightarrow Z^{-1} &= \frac{1}{R_p}\left[1 + iQ\left(\frac{\omega}{\omega_{\text{res}}} - \frac{\omega_{\text{res}}}{\omega}\right)\right], \end{aligned} \tag{3.5}$$

where ω_{res} is the resonance frequency given by the inductance and capacitance of the circuit:

$$\omega_{\text{res}} = \frac{1}{\sqrt{LC}}, \tag{3.6}$$

and Q denotes the quality factor, and at resonance, it is defined as

$$Q = \frac{R_p}{\omega_{\text{res}} L} = R_p \omega_{\text{res}} C. \tag{3.7}$$

The quality factor denotes the efficiency of the circuit. It is the ratio between the stored and lost energy per oscillation cycle. The estimation of the quality factor is discussed in section 3.1.2.1. From Eq. (3.7), it becomes obvious that a low capacitance, a large inductance, and a large Q value would be ideal to have a large R_p and, consequently, the maximum voltage drop at resonance $u_{\text{ind}} = R_p i_{\text{ind}} = Q\omega_{\text{res}} L i_{\text{ind}} = \frac{Q}{\omega_{\text{res}} C} i_{\text{ind}}$ (see Eq. (3.4) and Eq. (3.5)).

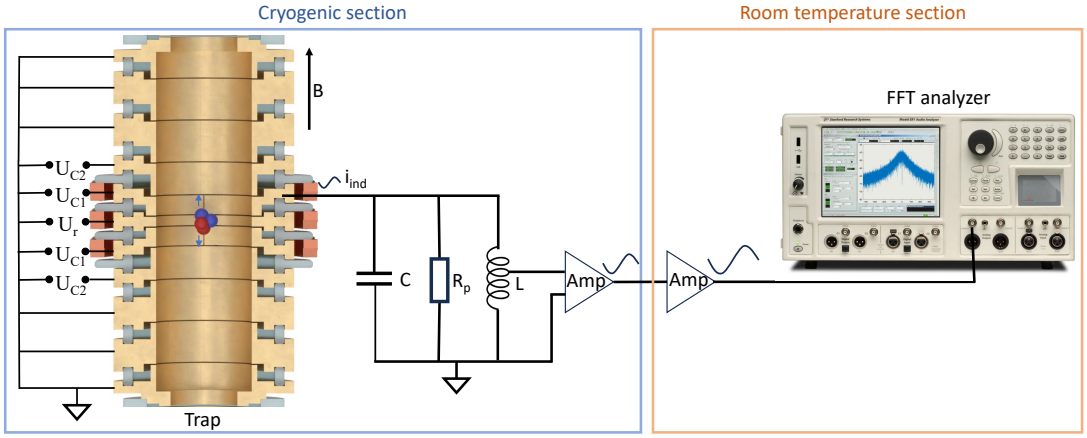

Figure 3.1. Illustration of the basic principle of the image current detection method. A tank circuit is a parallel LC circuit where the capacitance C includes the trap capacitance and all additional parasitic and non-parasitic capacitances. A homemade inductor coil with an inductance L is attached to the capacitance to form the tank circuit. The parallel resistance R_p represents the resistive losses in the circuit. The induced current i_{ind} is picked up by the tank circuit from the correction electrode(s) and converted to a measurable voltage amplified at two stages, once in the cryogenic section and then at the room temperature section before the signal is read out by a signal analyzer.

3.1.2.1 Resonator spectrum

The measurable electronic signal of the resonator is the thermal noise, also known as Johnson-Nyquist noise, which is a random electrical noise that arises due to the thermal energy of electrons in conductive materials [73, 74]. It is a fundamental type of noise that exists at any finite temperature. It is present in all electronic components and circuits independent of the voltage applied to it and only depends on the temperature and resistance. The thermal noise spectrum characterizes how the noise is distributed across different frequencies. An example of a thermal noise spectrum of the resonator is shown in Fig. 3.2. For a resonator designed to oscillate at a specific frequency, thermal noise manifests as voltage or current fluctuations that are directly related to the temperature of the system. The root mean square (RMS) voltage of thermal noise u_n represents the effective voltage that characterizes the noise in a system at a given temperature.

$$u_n = \sqrt{4k_B T Re(Z)\Delta\nu}, \tag{3.8}$$

where k_B is Boltzmann's constant, T is the absolute temperature in Kelvin, and $\Delta\nu$ is the bandwidth over which the RMS voltage is measured. Substituting Eq. (3.5) in Eq. (3.8) we can derive the RMS voltage of our resonator

$$u_n^{\text{res}} = \sqrt{\frac{4k_B T R_p \Delta\nu}{1 + Q^2\left(\frac{\omega}{\omega_{\text{res}}} - \frac{\omega_{\text{res}}}{\omega}\right)^2}}, \tag{3.9}$$

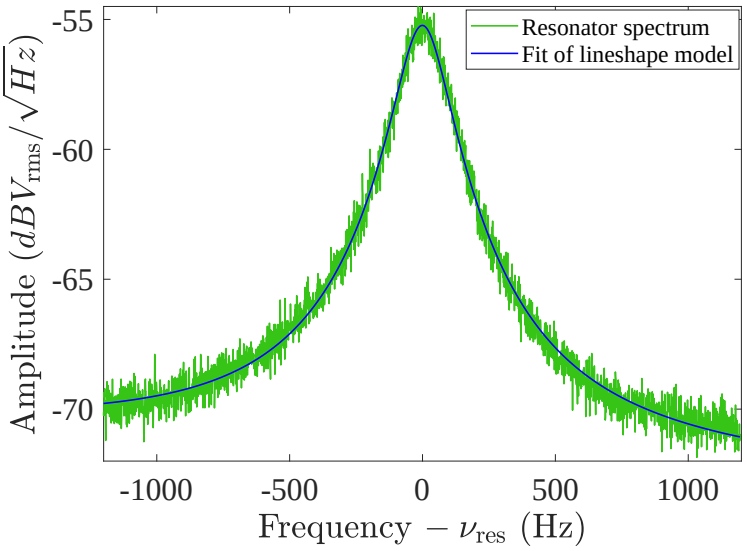

Figure 3.2. The thermal noise spectrum of the axial resonator connected to the trap. A lineshape model is fitted to the noise spectrum to extract the resonator parameter. For details see text.

A fast Fourier transformation (FFT) of the u_n^{res} results in a resonance curve. At resonance, the reactive components (inductance and capacitance) cancel each other, resulting in a purely resistive behavior. This means the impedance becomes purely real $Re(Z(\omega)) = R_p$, and the resonance curve reaches its peak. The peak value corresponds to the resonance frequency ω_{res}. Away from the resonance frequency, the reactive components dominate, leading to an increase in the imaginary part of impedance (reactance) and a decrease in the real part. The non-zero imaginary part of the detector impedance causes frequency shift which is discussed in section 3.1.5. The resonance spectrum shows the variation of the square root of the real part of impedance as a function of frequency, highlighting the point of resonance where the impedance is purely resistive (peak value). In practice, the quality factor can be obtained from the resonance curve as

$$Q = \frac{\omega_{\text{res}}}{\Delta\omega}, \tag{3.10}$$

where $\Delta\omega$ is the Full-Width-Half-Maximum (FWHM) of the resonator thermal noise spectrum, which is the -3 dB width of the spectrum. For large quality factor values (Q), the resonance curve of an LCR circuit becomes narrower, indicating lower energy losses.

3.1.2.2 Amplification

An ultra-low-noise cryogenic amplifier is responsible for amplifying the above-mentioned resonator signal and transferring it to the room-temperature section for further amplification and Fourier analysis. The design and working of the cryogenic amplifier developed by Dr. Sven Sturm can be found in [75].

In practice, the lineshape of the resonator spectrum is not straightforward. It has a contribution from the noise of the amplifier (u_n^{ampl}), which is frequency independent. The frequency dependence of the detection system (transfer function) results in a linearly (in log scale) decreasing noise characterized by the slope κ_{det}. Additionally, the signal is amplified by a factor A. The theoretically expected lineshape is

$$u_n^{\text{final}}(\omega) = A(1 + \kappa_{\text{det}}(\omega - \omega_{\text{res}}))\sqrt{(u_n^{\text{res}}(\omega))^2 + (u_n^{\text{ampl}})^2}. \tag{3.11}$$

On converting to decibel ($1\ \text{dBV}_{\text{rms}} = 20\log_{10}\frac{\text{V}_{\text{rms}}}{1\text{V}_{\text{rms}}}$) scaling

$$20\log_{10}u_n^{\text{final}}(\omega) = 10\log_{10}\left[\tilde{A}Re(Z)/R_p + (\tilde{u}_n^{\text{ampl}})^2\right] + \tilde{\kappa}_{\text{det}}(\omega - \omega_{\text{res}})\ (\text{dBV}_{\text{rms}}), \tag{3.12}$$

where $\tilde{A}$, $\tilde{u}_n^{\text{ampl}}$, $\tilde{\kappa}_{\text{det}}$ along with Q and ω_{res}, are extracted by fitting the resonator spectrum. Such a fit to the resonator spectrum is depicted in Fig. 3.2.

3.1.3 Detector-ion interaction

When an ion is trapped, it interacts with the tank circuit attached to the electrodes. The current induced by the ion will generate a voltage across the impedance of the tank circuit, which causes an additional force on the ion. From Eq. (3.1), Eq. (3.3), Eq. (3.4) and consid-

ering the axial motion of the ion such that $\omega = \omega_z$, the following relation for the additional reactive force can be derived.

$$F_z = qE_z = -q\frac{u_{\text{ind}}}{D} = -q\frac{Z(\omega_z)i_{\text{ind}}}{D} = -q^2\frac{Z(\omega_z)\dot{z}}{D^2}. \tag{3.13}$$

Thus the equation of motion of the ion (Eq. (2.9c)) will have an additional term

$$\ddot{z} + 2\gamma\dot{z} + \omega_z^2 z = 0. \tag{3.14}$$

The equation resembles a harmonic oscillator of frequency ω_z, damped with a damping constant $\gamma = \frac{q^2 Z(\omega_z)}{2mD^2}$. The damping constant is generally complex due to the complex nature of the impedance. The real and imaginary parts have different consequences and are explained in the next two sections.

3.1.4 Resistive cooling

The real part of the damping constant, resulting from the real part of the impedance of the detector, damps the axial motion of the ion. When the ion interacts with the detector system, the energy of the ion motion E is dissipated in the tank circuit. This way, the ion loses its energy in an exponential decay on a time scale called the cooling time constant τ:

$$\begin{aligned} E(t) &= E_0 \exp(-t/\tau), \\ \tau(\omega_z) &\equiv \frac{1}{2Re(\gamma)} \\ \Rightarrow \tau(\omega_z) &= \frac{mD^2}{q^2 Re(Z(\omega_z))}. \end{aligned} \tag{3.15}$$

In practice, the trap potential is tuned such that the axial frequency of the ion coincides with the resonance frequency of the resonator. There, the power $P = i_{\text{ind}}^2 R_p$ is dissipated most effectively. At resonance, the damping constant's imaginary part becomes zero, and the shift in the eigenfrequency, as described in section 3.1.5, is nulled.

$$\tau(\omega_z = \omega_{\text{res}}) = \frac{mD^2}{q^2 R_p}. \tag{3.16}$$

This process is referred to as 'resistive cooling' [76], which is most efficient at resonance. It is utilized to decrease the energy of trapped particles until they reach the physical temperature corresponding to the impedance of the tank circuit (see section 3.4).

3.1.5 Image current shift

The imaginary part of the damping constant due to the imaginary part of the detector impedance leads to a shift in the eigenfrequency of the ion. The presence of the imaginary component gives rise to an effective potential, as discussed in [75, 77], resulting in a frequency shift.

According to [77] the shift is

$$\Delta\omega_z = \frac{\gamma_0\gamma_{\text{res}}}{2}\frac{\omega_z - \omega_{\text{res}}}{(\omega_z - \omega_{\text{res}})^2 + \gamma_{\text{res}}^2/4}, \tag{3.17}$$

where $\gamma_0 = \frac{q^2 R_p}{2mD^2}$ (Eq. (3.15)), the resonator's damping constant $\gamma_{\text{res}} = \omega_z/Q$ and $(\omega_z - \omega_{\text{res}})$ is the detuning between the ion's axial frequency and the resonator's frequency. This frequency shift is known as the 'image current shift'[1]. Eq. (3.17)[2] denotes that for a specific detuning, the ion's frequency is pushed or pulled further away from the center frequency of the resonator, and thus this shift is often referred to as frequency pulling or pushing since it contributes to the displacement of the ion's frequency. The magnitude of this shift can be reduced by either bringing the ion into exact resonance with the tank circuit, where the impedance is completely real or by ensuring that the resonator's frequency is significantly different from the ion's frequency.

3.1.6 Non-thermalized ion detection: peak detection

When the ion interacts with the resonator, and its axial temperature is excited to overcome the thermal noise of the resonator, it initially appears as a peak on top of the resonator spectrum at the resonance frequency. The amplitude of the peak depends on the axial energy of the ion in comparison to the thermal noise of the resonator. At this point, there is no thermal equilibrium between the ion and the tank circuit. The ion is then detected by this peak, and the axial frequency is extracted from the maximum of the peak signal recorded as a Fourier spectrum. Such a peak signal is shown in Fig. 3.3a. The signal readout should be shorter than a few cooling time constants; otherwise, the axial energy will be dissipated at the tank circuit, and no peak can be observed. However, as the peak thermalizes fast, the achievable precision in the measured axial frequency is limited, and due to significant axial energy, the frequency measurements are exposed to energy-dependent shifts.

The SNR of the peak is defined as the ratio of the signal amplitude on the resonator (voltage drop across the impedance) and the thermal noise of the detection system. The electronic noises generated by the cryogenic amplifiers are neglected; see [75, 78].

$$\text{SNR}_{\text{peak}} \simeq \frac{q\omega_z\sqrt{R_p\tau_{\text{meas}}}}{D\sqrt{4k_BT}} z_{\text{rms}}, \tag{3.18}$$

where τ_{meas} is the signal readout time and ion in resonance is assumed. The signal readout time should be approximately $\tau_{\text{meas}} < 3\,\tau(\omega_{\text{res}})$.

In order to have a large SNR_{peak} for the best signal readout and detection, the temperature of the resonator could be decreased with the help of electronic feedback (see section 3.2.5).

[1] This is different from the image charge shift (introduced in section 3.1.9), which is a direct consequence of the ion interaction with the trap electrodes and does not depend on the detector circuit.

[2] The shift in modified cyclotron mode also follows this definition for the corresponding frequencies.

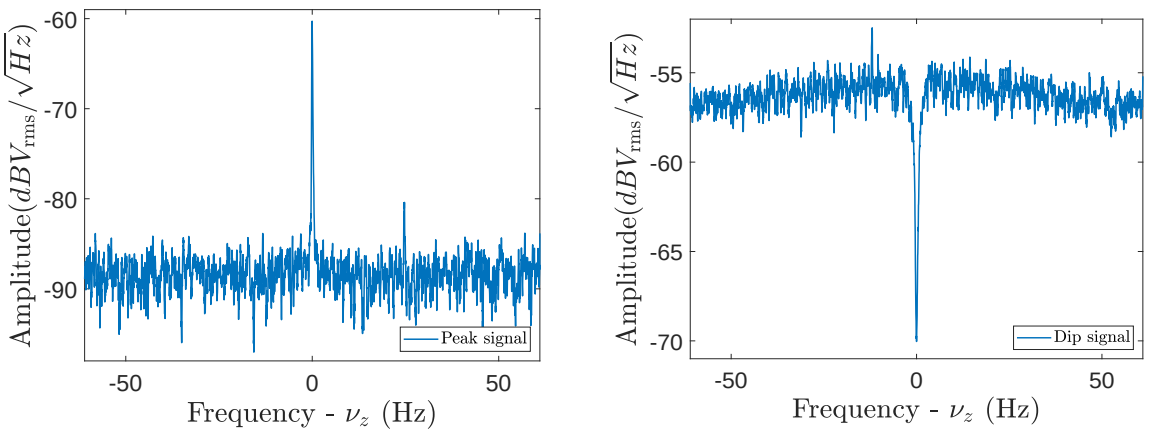

(a) Peak signal **(b)** Dip signal

Figure 3.3. Interaction of an ion with the resonator resulting in a peak and dip signal depending on the energy of the ion. In (a), an excited ion signal which appears as a peak over the thermal noise of the resonator, while dissipating its power, is shown. In (b), a signal when the ion is in thermal equilibrium with the resonator such that it shorts the noise of the detection system at its resonance frequency and appears as a dip is shown.

The image current could also be increased by increasing the oscillation amplitude z_{rms}, but this would lead to energy-dependent frequency shifts. It would be natural to think that an increase in the parallel resistance R_p would also help to increase the SNR, but this does not work out because the cooling time constant $\tau(\omega_{\mathrm{res}})$ scales inversely with R_p. Consequently, the measurement time τ_{meas} of the signal, which is proportional to the cooling time constant and limited by the same, also varies inversely with R_p.

3.1.7 Thermalized ion detection: dip detection

When an ion is tuned to the resonance frequency, it interacts and gets into thermal equilibrium with the resonator, depending on its cooling time constant. This also provides a possibility to measure the axial frequency. To explain the signal obtained from this interaction, first, the equation of motion of the ion Eq. (3.14) can be rewritten in terms of the induced current (Eq. (3.3)) and voltage (Eq. (3.4)) as

$$\frac{mD^2}{q^2}\frac{\partial i_{\mathrm{ind}}}{\partial t} + \frac{m\omega_z^2 D^2}{q^2}\int i_{\mathrm{ind}}\, dt = u_{\mathrm{ind}}. \tag{3.19}$$

The first and the second terms (on the right) can be identified as the voltage caused by an inductance (L_{ion}) and a capacitance (C_{ion}), respectively.

$$L_{\mathrm{ion}}\frac{\partial i_{\mathrm{ind}}}{\partial t} + \frac{1}{C_{\mathrm{ion}}}\int i_{\mathrm{ind}}\, dt = u_{\mathrm{ind}}. \tag{3.20}$$

Now, Eq. (3.20) resembles the differential equation of an undamped series LC circuit. To this end, the ion can be modeled as such a series LC circuit coupled to an LCR parallel

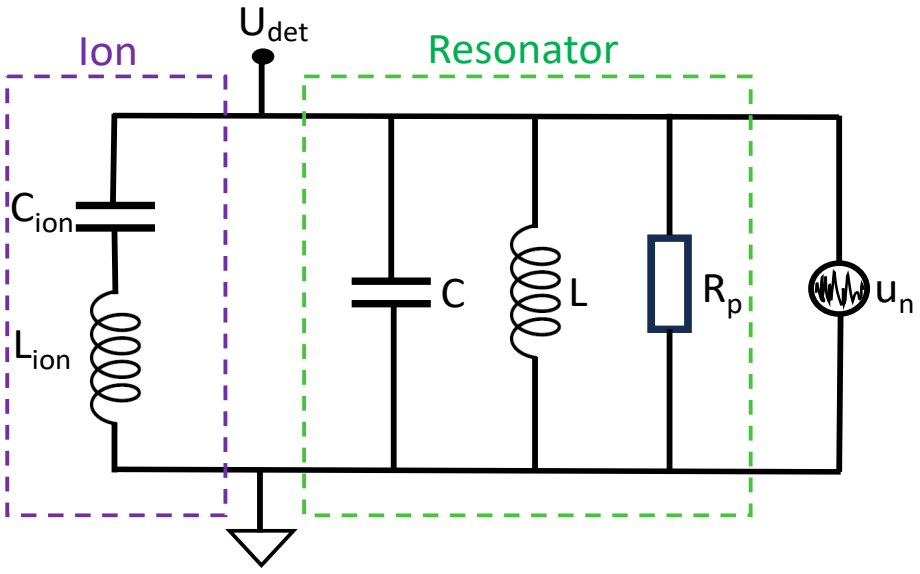

Figure 3.4. Equivalent circuit model of ion and resonator. The ion can be modeled as a series LC circuit parallel to the LCR tank circuit. See text for details.

circuit, which is the resonator. See Fig. 3.4. The equivalent circuit parameters of the ion with resonance frequency $\omega_{\text{res}} = \frac{1}{\sqrt{L_{\text{ion}} C_{\text{ion}}}}$, can be thus be identified as

$$L_{\text{ion}} = \frac{mD^2}{q^2}, C_{\text{ion}} = \frac{q^2}{m\omega_z^2 D^2} \tag{3.21}$$

The impedance of the equivalent series LC circuit of the ion is

$$Z_{\text{ion}} = i\omega L_{\text{ion}} - \frac{i}{\omega C_{\text{ion}}} \tag{3.22}$$

The total impedance of the ion and resonator circuit can be derived from Eq. (3.5) and Eq. (3.22) as

$$\begin{aligned} z_{\text{tot}} &= \left(\frac{1}{Z} + \frac{1}{Z_{\text{ion}}}\right)^{-1} \\ &= \left(\frac{1}{R_p}\left(1 + iQ\left(\frac{\omega}{\omega_{\text{res}}} - \frac{\omega_{\text{res}}}{\omega}\right)\right) + \frac{i}{\omega R_p \tau}\left(\frac{\omega_z^2}{\omega^2} - 1\right)^{-1}\right)^{-1}, \end{aligned} \tag{3.23}$$

where $\tau = \tau(\omega_z = \omega_{\text{res}})$ is the cooling time constant. Only the real part of the total impedance influences the thermal noise spectrum, and using Eq. (3.6), this can be re-written as

$$Re(z_{\text{tot}}) = R_p \frac{(\omega_{\text{res}}\omega(\omega^2 - \omega_z^2))^2}{(\omega_{\text{res}}\omega(\omega^2 - \omega_z^2))^2 + (Q(\omega^2 + \omega_{\text{res}}^2)(\omega^2 - \omega_z^2) - \omega_{\text{res}}\omega^2/\tau)^2}. \tag{3.24}$$

To estimate the noise density and the lineshape, Eq. (3.24) can be inserted into Eq. (3.8)

and finally converted to $\mathrm{dBV_{rms}}$ units as described in section 3.1.2.2 and Eq. (3.12) as:

$$20\log_{10}u_n^{\mathrm{dip}}(\omega) = 10\log_{10}\left[\tilde{A}Re(Z_{\mathrm{tot}})/R_p + (\tilde{u}_n^{\mathrm{ampl}})^2\right] + \tilde{\kappa}_{\mathrm{det}}(\omega-\omega_{\mathrm{res}})\ (\mathrm{dBV_{rms}}). \quad (3.25)$$

This is the lineshape of the thermal noise of the resonator with a thermalized ion signal. As the series LC circuit has minimum impedance at resonance, the ion in thermal equilibrium with the resonator effectively shortens the detector impedance at its resonance frequency, which is the axial frequency in this case. This appears as a sharp minimum in the thermal noise of the resonator and is called a 'dip' as seen in Fig. 3.3b and Fig. 3.5a. Accordingly, the frequency of the ion can be measured in thermal equilibrium with the resonator and at low axial energy. The unperturbed frequency is extracted by least squares fitting the dip spectrum using the lineshape model[3] given by Eq. (3.25)[4]. A fit of the dip spectrum with the lineshape model is illustrated in Fig. 3.5b. The extracted axial frequency is not affected by the image current effect (see section 3.1.5) as far as the ion is in resonance with the detection system. The dip can be characterized by its -3 dB dip-width (linewidth) $\Delta\nu_z$ [76], which is related to the cooling time constant and the number of trapped ions N.

$$\Delta\nu_z = \frac{N}{2\pi\tau}. \quad (3.26)$$

For weak coupling, such that the dip-width is much smaller than the resonator width, the dip-width linearly scales with the number of ions in resonance; thus, this relation allows us

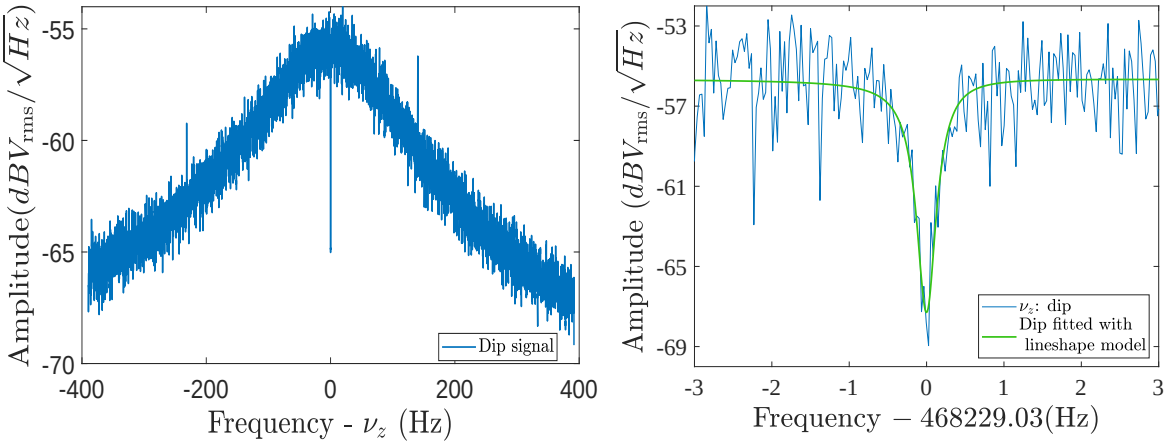

(a) Zoomed-out view of the dip

(b) Zoomed-in view of the dip

Figure 3.5. A dip spectrum of a $^4He^{2+}$ ion. In (a) a zoomed-out view of the dip on the thermal noise of the resonator is visible. (b) is a detailed illustration of the dip with $\sim$ 500 mHz of -3 dB width fitted with a lineshape model, which enables the detection of the axial frequency of the ion

[3] Here, ν_z is assumed to be perfectly stable otherwise these cause extra shifts.

[4] The resonator parameters which are input to the dip lineshape model are obtained beforehand by fitting the thermal noise spectrum of the resonator without an ion.

to determine the number of thermalized trapped ions provided they have similar or the same ν_z and are coherently moving.

The SNR of the dip signal is defined as the thermal noise of the resonator divided by the noise floor at the resonance frequency of the ion. The noise floor at the frequency of the ion or the 'dip-depth' is limited by the amplifier's voltage noise and the frequency resolution. The dip-depth (in logarithmic units) is infinite for an ideal amplifier with no noise, assuming a perfectly stable ν_z. The SNR is then given as [75]:

$$\mathrm{SNR}_{\mathrm{dip}} = \frac{\sqrt{4k_B T R_p \kappa^2 + (i_n^{\mathrm{amp}} R_p \kappa^2)^2}}{u_n^{\mathrm{amp}}}, \tag{3.27}$$

where i_n^{amp} is the current noise density of the amplifier, and the other parameters have the same meaning as described in Eq. (3.11). From the equation, it can be noted that an increase in temperature or current noise density would lead to a better SNR, but this would increase the temperature of the ion and lead to systematic shifts. The SNR can be maximized using a low-noise amplifier (low u_n^{amp} and i_n^{amp}) and a resonator with a high Q value ($\propto R_p$).

3.1.8 Measurement of axial frequency

The dip detection technique described in section 3.1.7 is used for measuring the axial frequency of a thermalized ion in our experiment. In the process, the ion cools to the temperature of the tank circuit (4.2 K) (see section 3.1.4 and section 3.4), thus having small thermal amplitudes which minimize the energy-dependent systematic shifts during the dip detection process. However, this technique is incoherent as the ion in resonance with the detection system is driven by the incoherent thermal noise. Therefore, long averaging over the noise spectra is required to have a good fit quality of the dip. The frequency uncertainty scales inversely to the square root of the averaging time: $\delta\nu_{z,\mathrm{dip}} \sim 1/\sqrt{T}$. To measure the axial frequency, FFT spectra of the thermal noise are acquired usually after an averaging time of $\sim$3 min[5]. However, such long averaging times have the disadvantage that during this period, the axial frequency is subject to systematic shifts due to changes in the trapping potential. Another disadvantage of the dip detection technique is that the extraction of the unperturbed axial frequency depends on a fit of the lineshape model to the thermal noise spectrum, see section 3.1.7. The lineshape model uses the fitted resonator parameters as input. To this end, these parameters must be known precisely, which is not the case, resulting in a systematic shift of the axial frequency. More details on this can be found in section 6.4.5.

The axial frequency measurement is performed in the Precision Trap, with a superconducting resonator connected to the lower correction electrodes and an endcap electrode. In this campaign, the resonator had a Q value of about 2300. More details in section 4.4.1.

[5]The averaging time depends on the resolution required. For mass measurement, axial frequencies are extracted after an averaging time of 3 min to resolve and improve the visibility of the dip signal. However, shorter averaging times ($\sim$1 min) are used if a lower precision measurement is performed.

3.1.9 Image charge shift

The induced image charges on the electrode essentially make it possible to detect the ion, but these image charges produce an additional electric field and cause a change in the effective trapping potential resulting in a frequency shift known as 'image charge shift'. This should not be confused with the 'image current shift' (discussed in section 3.1.5), which depends on the interaction of the ion with the resonator. The image charge shift is a direct result of the ion interaction with the electrodes and originates from pseudo-static charges. The eigenmotion of the trapped particle makes the induced image charges dynamic but time-retarded due to the finite speed of light. This can lead to a frequency-dependent phase shift between the ion motion and the back-action of the image charges [79, 80]. However, unlike free electrons, where the field retardation and resulting cavity shifts (the conductive walls of the trap act as a microwave cavity) are significant, these effects are negligible for an atomic ion. This is because the wavelengths related to the eigenmodes of the trapped particle are much larger than the trap size ($\lambda = \frac{c}{\nu} \gg r_{\text{trap}} = 5$ mm for all eigenfrequencies). Thus, the phase shifts due to the dynamic nature of the image charges are negligible for all eigenfrequencies in our case, and only contributions from the effective back action of the image charges, which is in phase with the ion motion, are considered.

Due to the axial symmetry of the cylindrical Penning trap, the force caused by the image charges acts mainly in the radial direction and causes energy-independent image charge shift of the radial frequencies. A detailed discussion of this shift can be found in [81]. If the electrodes of the cylindrical Penning trap are assumed to be infinitely long electrodes with radius r_0, an analytical calculation of the ICS is possible [82] and results in

$$\Delta\nu_{\pm} = \mp\frac{q^2}{16\pi^2\epsilon_0 m r_0^3 \nu_c}, \tag{3.28}$$

where ϵ_0 is the vacuum permittivity. The magnetron and cyclotron frequencies shift by the same magnitude with different signs. This does not cancel out in estimating cyclotron frequency when using the invariance theorem Eq. (2.17). Then, the relative cyclotron frequency shift can be estimated as

$$\frac{\Delta\nu_c}{\nu_c} = \left(-\frac{\nu_+}{\nu_c} + \frac{\nu_-}{\nu_c}\right)\frac{m}{4\pi\epsilon_0 B_0^2 r_0^3} \approx -\frac{m}{4\pi\epsilon_0 B_0^2 r_0^3}. \tag{3.29}$$

From Eq. (3.29), it is clear that a larger trap radius decreases the shift, but a bigger trap would have a diminished detectable image current signal. Thus, the trap design involves a compromise between the signal strength and the influence of image charge on the ion.

The image charges can also be simulated using the trap geometry, and such simulations using COMSOL based on finite element methods were performed for our trap geometry. The calculated relative shift of the cyclotron frequency (Eq. (3.29)) has a prefactor slightly

smaller than 1. Therefore, $\frac{\Delta\nu_c}{\nu_c} \approx -0.975\frac{m}{4\pi\epsilon_0 B_0^2 r_0^3}$ (from table II in [81]). The results of this simulation and an experimental determination of this effect in the LIONTRAP experiment are reported in [81]. A detailed explanation of a re-measurement of this frequency shift in our trap during this thesis can be found in section 5.6.

3.2 Excitation and coupling of eigenmotions

Manipulation and control of the ion's motion are necessary for high-precision measurements. This is achieved by applying oscillating electric fields to an electrode or a split electrode, or even a set of electrodes. These radio-frequency excitations allow eigenfrequency detection and cooling based on sideband coupling of different states of the ion's motion. Excitations are also used to excite the eigenmotions individually when applied at the corresponding frequency of the desired motion to be excited. In this section, the basics of the dipolar, quadrupolar, and LC excitation, which are used extensively at LIONTRAP, are discussed.

3.2.1 Dipolar excitations

The dipole excitation is used to directly excite a specific motional mode. A dipolar excitation requires an electric field that exerts an additional force on the ion during the excitation pulse time. For example, a dipolar excitation in the axial direction would exert a force:

$$\vec{F}_{D_z} = q\vec{E}_{D_z} = -q\frac{U_{D_z}}{D_{\text{eff}}}\cos\left(\omega_{\text{rf}}t + \phi_{\text{rf}}\right)\begin{pmatrix}0\\0\\1\end{pmatrix}, \tag{3.30}$$

where U_{D_z} is the amplitude of the excitation signal, ω_{rf} is the frequency of excitation, D_{eff} is the effective electrode distance of the excitation electrode and ϕ_{rf} is the phase with respect to the ion's motion. This modifies the equation of motion of the ion (Eq. (2.9)), making it analogous to a forced harmonic oscillator.

The excitation drives must be applied at the frequency of the particular mode that needs to be excited with the right field geometry. So for axial dipolar excitations $\omega_{\text{rf}} = \omega_z$. Such an excitation can be realized by applying a radio frequency voltage on an off-center electrode (correction or endcap electrodes). During this work, the D_z excitation line was connected to an endcap electrode. Similarly, for excitations of the radial modes, a driving electric field directed radially is produced by applying alternating electric voltages at the corresponding frequency ($\omega_{\text{rf}} = \omega_+$, $\omega_{\text{rf}} = \omega_-$) using vertically split electrodes.

Depending on the initial phase ($\phi - \phi_{\text{rf}}$) and frequency ($\omega - \omega_{\text{rf}}$) relation between the excitation and the ion's eigenmotion, the amplitude either immediately increases or initially decreases (known as transient oscillation) and then increases in-phase with the excitation. If the ion's phase lags $90°$ behind the excitation drive's phase ($d\phi = \phi - \phi_{\text{rf}} = $ -90°) and the excitation amplitude is much larger than the ion's initial amplitude, the amplitude or radius of the ion motion increases linearly. Thus, dipolar excitation on a cold ion can be

used to imprint an amplitude and phase, which is extensively used during phase-sensitive measurements, to be discussed in section 3.3. If the ion has large initial amplitudes, this will influence the final phase after excitation. So, in general, the ion has to be cooled to as low temperatures as possible, or the excitation pulse should be large enough to reduce the impact of the initial thermal distribution.

3.2.2 Quadrupolar excitations

Quadrupolar excitation, as the name suggests, has a quadrupolar field configuration and is usually used to couple two eigenmodes, thereby causing an energy exchange between the modes. The most used excitation in our experiment is Q_{xz}, which causes a force on the ion:

$$\vec{F}_{Q_{\mathrm{xz}}} = q\vec{E}_{Q_{\mathrm{xz}}} = -q\frac{U_{Q_{\mathrm{xz}}}}{D_{\mathrm{eff}}^2}\cos\left(\omega_{\mathrm{rf}}t + \phi_{\mathrm{rf}}\right)\begin{pmatrix} z \\ 0 \\ x \end{pmatrix}. \tag{3.31}$$

Energy exchange between the modes with such excitations has the advantage that an axial resonator suffices to address the radial modes. This excitation can be achieved using half of a vertically (azimuthally) split off-center electrode. However, it does not produce a purely quadrupolar field but might contain dipolar components, which allows us to use the Q_{xz} excitation line to supply both quadrupolar, dipolar, and parametric excitations, see section. 4.4.3. An excitation to couple between two radial modes, Q_{xy}, would require breaking the two-fold symmetry of an azimuthally split electrode; for example, this can be achieved by splitting an electrode into quarters. Electrodes divided into quarters are not implemented at Liontrap, and thus Q_{xy} excitations are not possible.

The Q_{xz} excitation can be done at any of the four sidebands $\omega_+ \pm \omega_z$ or $\omega_z \mp \omega_-$ to couple independent eigenmodes in different ways. The equations governing the motion of the coupled trapping modes can be expressed in a manner analogous to a driven quantum-mechanical two-level system. The frequencies associated with these modes are obtained from solving the time-independent Schrödinger equation for the coupled system [58, 83][6].

Blue sideband: Upper modified cyclotron sideband and lower magnetron sideband When the coupling frequency is $\omega_+ + \omega_z$ or $\omega_z - \omega_-$, the amplitudes of both modes increase exponentially after an initial transient response. The energy gain process of the modes can be easily understood with a quantum mechanical approach of the coupled harmonic oscillator. The heating (photon absorption) rate and the cooling (stimulated emission) can be understood as the ion absorbing or emitting a photon of the sideband frequency. In the process, the initial quantum states $|n_z, n_\pm\rangle$ of the ion which interacts with a photon with energy $E = \hbar(\omega_z \pm \omega_\pm)$ changes to $|n_z + 1, n_\pm + 1\rangle$ or $|n_z - 1, n_\pm - 1\rangle$. On calculating the transition probability using the creation and annihilation operators of the interacting oscillators,

[6] The analogy between the quantum mechanical and classical Rabi oscillations is described in [84]

it can be derived that the heating process dominates the cooling process. Now, switching back to the generally used classical approach in the regime we work (quantum numbers $> 10^5$, see section 3.4), the heating process is analogous to an increased amplitude or radius. The phases of the excited mode depend on the initial phases of the motional modes and the coupling pulse. This has been put to use in the phase-sensitive detection technique of the modified cyclotron frequency discussed in section 3.3 and [85].

Red sideband: Lower modified cyclotron sideband and upper magnetron sideband When the coupling frequency is $\omega_+ - \omega_z$ or $\omega_- + \omega_z$, amplitudes of both modes are modulated (Rabi-like oscillations) with Rabi-frequency over time depending on the strength of the coupling field as

$$\begin{aligned} z(t) &= \hat{z}_{\text{max}} \sin\left(\frac{\Omega}{2}t + \phi_\Omega\right) \sin(\omega_z t + \phi_z) \\ r_\pm(t) &= r_{\pm,\text{max}} \cos\left(\frac{\Omega}{2}t + \phi_\Omega\right) \sin(\omega_\pm t + \phi_\pm), \end{aligned} \tag{3.32}$$

where $\hat{z}_{\text{max}}$ and $r_{\pm,\text{max}}$ are the maximum motional amplitudes. ϕ_z and ϕ_Ω are arbitrary initial phases and the Rabi frequency

$$\Omega = \frac{qU_{Q_{\text{xz}}}}{2mD_{\text{eff}}^2\sqrt{\omega_z\omega_\pm}}. \tag{3.33}$$

There is a continuous transfer of action (classical) between the modes while such excitation is applied. The ion is thermalized with the resonator during the entropy transfer with the coupling pulse, which results in the cooling of the modes and also allows the measurement of radial frequencies. These applications are discussed in section 3.2.3 and section 3.2.4, respectively. The red sideband frequency is also used for phase-sensitive detection, known as the PnP (Pulse aNd Phase) technique [86], to extract the modified cyclotron frequency (see section 3.3).

3.2.3 Sideband cooling

In section 3.1.4, the cooling method for the axial frequency is discussed. For the modified cyclotron motion, resistive cooling can be achieved by connecting a tuned resonator between the two halves of an electrode. This way, the image currents can also be used to detect the modified cyclotron frequency and, consequently, cool the mode. However, detecting and cooling the magnetron motion this way is impossible because any dissipation at the magnetron frequency would increase the magnetron radius, and a rapid ion loss due to the negative energy associated with the metastable magnetron mode would occur.

At LIONTRAP, there is no tuned modified cyclotron resonator for the ions of interest, but the red sideband coupling can be used to dissipate energy in the radial mode to the axial resonator. Such a cooling technique where a mode of the ion is thermalized with the

resonator and a coupling drive at the sideband frequencies is applied to thermalize both the involved modes to the resonator is known as 'sideband cooling'. This technique is especially interesting for the magnetron motion, as direct cooling is impossible.

Just as described in the case of blue sideband coupling, the energy transfer between the modes can be explained quantum mechanically where the quantum states change due to the interaction with the photon at frequency $\omega_{\pm} \mp \omega_z$. The quantum number of one mode increases while the other mode's quantum number decreases, and vice versa. This continues until the time-averaged quantum number of both the involved modes converge $\langle n_z \rangle = \langle n_{\pm} \rangle$ [63]. This sideband cooling process is illustrated with an energy level diagram in Fig. 3.6. Thus the average values of the energies (temperatures) of both modes are related to each other via the frequency ratio (see Eq. (2.22)). The whole sideband cooling process is performed with a cooled axial mode which results in the dissipation of energy from the radial modes to the axial resonator until thermal equilibrium is achieved. For more details regarding the temperature of the modes, see section 3.4.

The advantage of using sideband cooling over direct resonator cooling is that no image current shift is involved, and a single axial resonator can be used generally for all eigenmodes. However, the temperature that can be achieved with direct cooling with a cryogenically cooled resonator is much lower than the sideband cooling.

3.2.4 Measurement of radial frequencies: double-dip

As mentioned earlier, when an excitation drive with the red sideband frequency is applied, the energy transfer between the coupled modes occurs at the Rabi frequency Ω. This frequency depends on the amplitude of the drive that is applied, which can be understood from

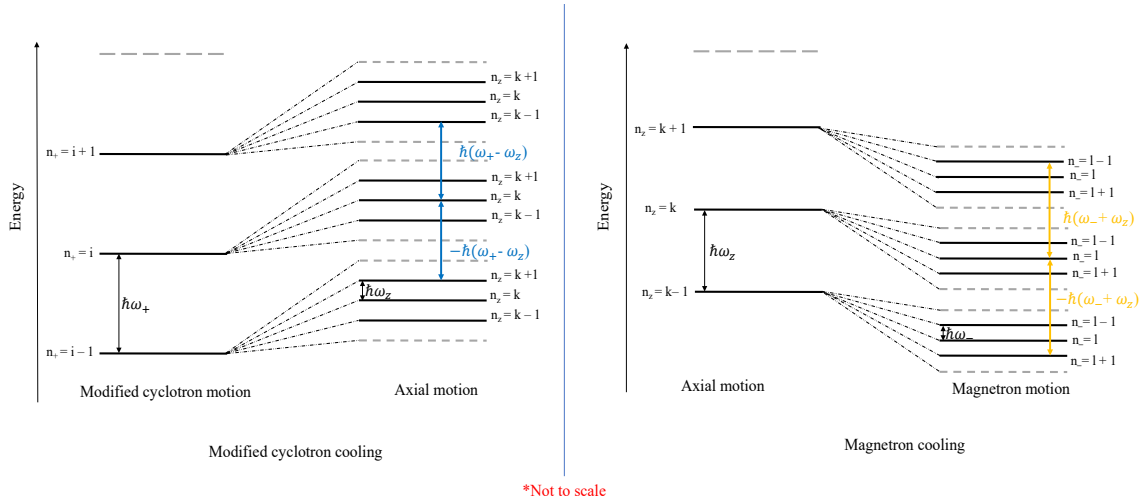

Figure 3.6. Energy level scheme of the cyclotron, the axial and the magnetron motions (not to scale). The transition between the quantum states during the sideband cooling of the radial motions is shown.

Eq. (3.33). On expanding Eq. (3.32) we arrive at the modulated axial amplitude given by

$$z(t) = \frac{1}{2}\hat{z}_{\text{max}}\left[\cos\left(2\pi\left(\nu_z - \frac{\Omega}{4\pi}\right)t + (\phi_z - \phi_\Omega)\right) - \cos\left(2\pi\left(\nu_z + \frac{\Omega}{4\pi}\right)t + (\phi_z - \phi_\Omega)\right)\right] \tag{3.34}$$

implying that the dip splits into two components (left and right of the dip) with frequencies

$$\begin{aligned}\omega_l &= \omega_z - \frac{\Omega}{2}\\ \omega_r &= \omega_z + \frac{\Omega}{2}.\end{aligned} \tag{3.35}$$

This frequency spectrum recorded at thermal equilibrium is known as a double-dip, and the separation between the two dips is exactly the Rabi frequency at resonance. An example of such a frequency spectrum at the coupling frequency $\omega_{\text{rf}} = \omega_+ - \omega_z$ is shown in Fig. 3.7. In case the coupling drive ω_{rf} is not in perfect resonance, the individual frequencies of the components of the double-dip change accordingly and result in asymmetric left and right dip around the axial frequency indicating an avoided crossing behaviour [83]. If the detuning $\delta_\pm = \omega_{\text{rf}} - (\omega_\pm \mp \omega_z)$, then the frequencies of the right and left dip are shifted as:

$$\begin{aligned}\omega_l &= \omega_z - \frac{\delta_\pm}{2} - \frac{\Omega'_\pm}{2}\\ \omega_r &= \omega_z - \frac{\delta_\pm}{2} + \frac{\Omega'_\pm}{2}\end{aligned} \tag{3.36}$$

where $\Omega'_\pm = \sqrt{\Omega_\pm^2 + \delta_\pm^2}$ is the modified Rabi frequency. In such a non-resonant coupling, the action is not transferred from one mode into another completely. For coherent Rabi oscillations, both modes are still thermalized as long as both dips are on the resonator. Since the Rabi splitting of the dips is mathematically described as a two-ion system having axial frequencies $\omega_{l,r}$, the effective impedance of the system is then

$$\begin{aligned}z_{\text{tot,DD}} &= \left(\frac{1}{Z_{\text{det}}} + \frac{1}{Z_{\text{Ion1}}} + \frac{1}{Z_{\text{Ion2}}}\right)^{-1}\\ &= R_p\left(1 + iQ\left(\frac{\omega}{\omega_{\text{res}}} - \frac{\omega_{\text{res}}}{\omega}\right) + \frac{i}{\omega\tau_l}\left(\frac{\omega_l^2}{\omega^2} - 1\right)^{-1} + \frac{i}{\omega\tau_r}\left(\frac{\omega_r^2}{\omega^2} - 1\right)^{-1}\right)^{-1}\end{aligned} \tag{3.37}$$

where τ_l and τ_r are the cooling time constants of the individual dips, the definitions can be found in [30]. Compared to the single axial dip, the dip widths (determined by τ_l and τ_r) of the left and right dips are reduced by a factor of two. The lineshape of the double-dip is then described in the same manner as that of the dip by using $Re(Z_{\text{tot,DD}})$.

Using the ω_z determined from the single dip spectrum, independently measured in the absence of excitation (see section 3.1.7), along with the known ω_{rf} and the frequencies $\omega_{l,r}$ obtained by fitting a lineshape model to the double-dip, the radial frequencies can be

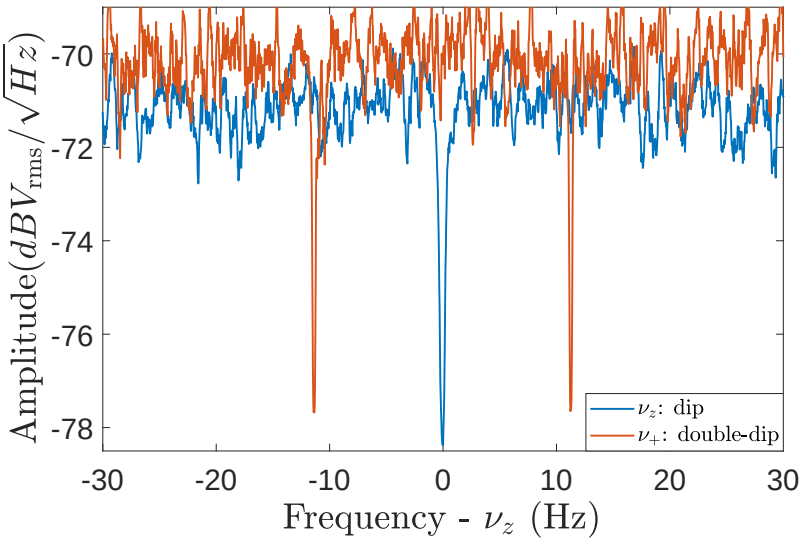

Figure 3.7. A dip (blue) and double-dip (red) spectrum of $^4He^{2+}$: The double-dip spectrum (red) at $\omega_{\mathrm{rf}} = \omega_+ - \omega_z$, enables the detection of the modified cyclotron frequency of the ion. At resonant coupling, the individual dips of the double-dip are symmetrically split on either side of the dip signal, and the width of these are half the width of the single axial dip. For details, see the text.

determined as

$$\begin{aligned} \omega_- &= \omega_{\mathrm{rf}} + \omega_z - \omega_l - \omega_r \\ \omega_+ &= \omega_{\mathrm{rf}} - \omega_z + \omega_l + \omega_r. \end{aligned} \tag{3.38}$$

Measuring the magnetron frequency has some complexity involved as the coupling frequency $\omega_{\mathrm{rf}} = \omega_- + \omega_z$ is close to the axial frequency. Thus, the coupling drive has the tendency to interact with the resonator and introduce extra noise to it. The axial motion of the ion is also excited by this and results in a higher temperature. Such changes in the axial frequency will result in an incorrect determination of the magnetron frequency. Thus, in our experiment, we measure the magnetron frequencies from the double-dip at different coupling strengths and then extrapolate to zero excitation and extract the actual magnetron frequency. The magnetron frequency with the lowest magnitude among the eigenfrequencies influences the cyclotron frequency the least when using the invariance theorem. Hence, it is not measured in every mass measurement cycle but only sporadically during the measurement campaign.

The double-dip technique has the ion in thermal equilibrium during the measurement and thus, reduces energy-dependent systematic shifts. However, it has the drawback that the interaction between the ion and the tank circuit causes frequency pulling [77]. Thus, this method relies on a lineshape model to extract the unperturbed frequencies. Furthermore, as we need to average over a noise signal, the measurement takes a long time, making it sensitive to magnetic field fluctuations. As a result the achievable precision using the double-

dip technique is limited. While this is more than sufficient for the magnetron frequency, the leading order modified cyclotron frequency needs to be extracted with the highest possible precision. The aforementioned issues are, to a large extent, mitigated by employing coherent phase-sensitive measurements of the modified cyclotron frequency, which will be discussed in section 3.3.

3.2.5 Electronic feedback

Electronic feedback to the detection system can be used to change the detector's resonance frequency or energy and, as a result, influence the ion's (in resonance) motion. In our experiment, active electronic feedback is used to manipulate the thermal noise of the resonator to effectively reduce its temperature and, consequently, the ion's temperature.

The electronic feedback is accomplished when the normal output signal of the axial amplifier is phase shifted, attenuated, and finally capacitively fed back to the resonator [63, 75]. By adjusting the attenuation, one can influence the feedback gain (G_{FB}), and adjusting the phase of the fed-back signal allows for selecting the desired type of feedback. A detailed explanation of this technique can be found in [75, 87]; here, only a brief discussion of this well-known method is done.

Depending on the phase of the signal that is returned to the detection system, the effect of the feedback loop is different:

90° phase-shifted feedback: When the phase of the feedback is shifted $\pm 90^{\circ}$ compared to the ion signal, the effective parallel capacitance of the resonator is modified. This could result in a shift in the resonance frequency of the resonator by a few line widths. However, the Q value remains unchanged with this type of feedback. Due to the change in resonance frequency when such feedback is applied, the ion-resonator interaction is minimized, and thus the cooling time constant of the ion is increased.

0° or 180° phase-shifted feedback: By applying this type of feedback signal, the quality factor Q of the resonator varies, leading to a modification in the ion's effective temperature. The temperature changes that occur are contingent upon the feedback gain G_{FB} as $T_{\mathrm{eff}} = (1 \pm G_{\mathrm{FB}})\, T$. The two possibilities depending on the sign can be achieved by selection of the appropriate phase:

- **Positive feedback**: A 0° phase-shifted feedback signal increases the Q value and, thereby, increases the temperature of the resonator. The coupling of the ion with the resonator is significantly higher. This results in larger dip width of the ion signal.

- **Negative feedback**: With 180° phase shift, the effect is quite the opposite compared to the positive feedback. The Q value of the resonator is reduced, which in turn decreases the effective temperature of the detector system. The dip-width of the ion also reduces in this setting. This negative feedback is used in our experiment to reduce the

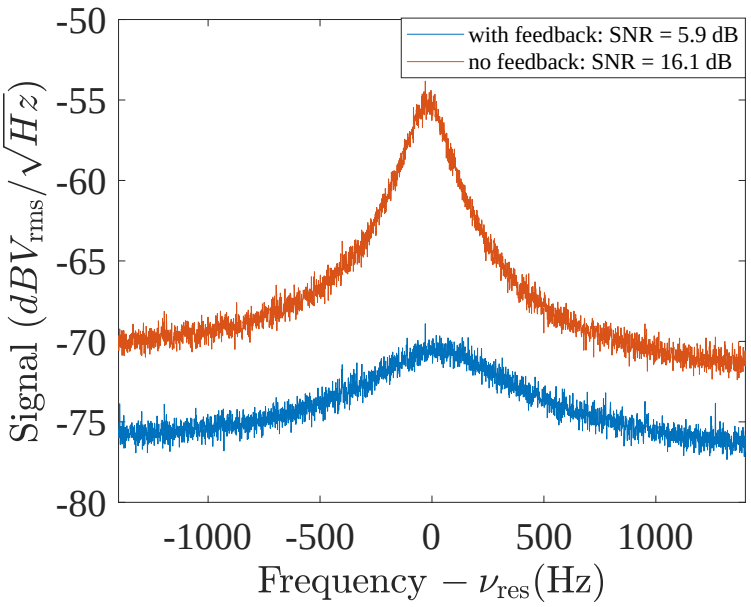

Figure 3.8. Thermal noise spectrum of the resonator with and without negative feedback. The SNR is reduced from 16.1 dB to 5.9dB with 180° phase-shifted feedback. The application of feedback results in a decrease of 6 dB in the signal level as the impedance of the mixer changes when the local oscillator output is turned on for feedback.

temperature of the ion below the ambient temperature of 4.2 K. The lower limit of the achievable temperature is set by the electronic noise of the amplifier.

In Fig. 4.9, section 4.4.4, the electrical connections of the feedback setup are demonstrated. In the experiment, the feedback is adjusted by scanning phases and attenuation to obtain the required feedback type and strength. During this work, an attenuation of 68 dB and a feedback phase of $30°$ is used to decrease the SNR from 16 to 6 dB without changing the resonator frequency. Fig. 3.8 shows the resonator spectra with and without feedback.

An alternate method to influence the ion's motion is by applying a signal back to the ion through an electrode instead of the resonator and is often referred to as 'self-excitation of the single ion oscillator', which is discussed in [75, 88].

3.3 Measurement of modified cyclotron frequency: phase sensitive

As seen in section 3.2.4 and section 3.1.8, the incoherent detection technique has several disadvantages, which are overcome by using a coherent phase-sensitive method of detection. In such methods, usually, the instantaneous phase of the ion at two moments separated by an evolution time is recorded from which the frequency of the mode can be estimated as $\nu = \Delta\phi/(360° \ \Delta T_{\mathrm{evol}})$. The phase evolves linearly with time and enables an accurate determination of the frequency. Thus, the main advantage of phase-sensitive measurement is the relative uncertainty of the frequency (see section 6.6), which scales inversely with

measurement time, unlike the dip or double-dip technique.

The free cyclotron frequency, which is of large importance in a mass measurement, is most influenced by the modified cyclotron frequency when using the invariance theorem and hence this needs to be measured with the highest precision. Therefore, phase-sensitive techniques like PnA (Pulse aNd Amplify) and PnP (Pulse aNd Phase) are commonly used to extract the frequency of the modified cyclotron mode.

Any phase-sensitive technique involves imprinting a phase (ϕ_0) onto the modified cyclotron mode, which is then allowed to evolve freely. After a certain evolution time (T_{evol}), the final phase ($\phi_1 = \phi_0 + \omega_+ T_{\text{evol}}$) is detected usually by transferring the phase information from the modified cyclotron motion to the axial motion with the help of a coupling drive. Finally, the eigenmodes are cooled.

The coupling pulse, which is used to manipulate the energy of the modes and also transfer the phase information, differs depending on the type of phase-sensitive detection technique used. In the PnP technique [83], the coupling pulse $\omega_{\text{rf}} = \omega_+ - \omega_z$ is used to transfer the classical action from the modified cyclotron mode to the axial mode as described in 3.2.2. The axial energy of the ion after the coupling pulse is determined by the initial energy of the cyclotron mode. The SNR of the signal after the coupling needs to be large enough to unambiguously detect and extract the phase information. Therefore, the initial energy of the cyclotron mode should be adequately high and this could result in systematic shifts. On that account, at LIONTRAP the PnA technique [85] is used to couple the modes. In the PnA technique, $\omega_{\text{rf}} = \omega_+ + \omega_z$, which leads to parametric amplification of both modes without any loss of the phase information. The excitation of the axial mode and, consequently, the SNR of the detection signal relies on the strength of the coupling field[7]. The initial energy of the cyclotron mode needs to be only sufficiently high enough to define a phase. This allows a frequency measurement starting from reasonably low modified cyclotron energies.

The phase definition, phase evolution and conservation of phase information during the coupling pulse of the modified cyclotron mode is illustrated in Fig. 3.9. The PnA pulse routine (PnA cycle) and the principle of parametric amplification are shown in Fig. 3.10.

The details of the steps involved in a PnA measurement during this work are as follows:

First pulse: A dipolar excitation (D_x) at the modified cyclotron frequency $\omega_{\text{rf}} = \omega_+$ is applied on a thermalized ion. This imprints a phase on the ion and also increases the modified cyclotron radius depending on the pulse length and amplitude. During this work, pulse lengths ranging from ∼5 ms to ∼50 ms and an amplitude of 0.1 Vpp were used.

Phase accumulation: The phase of the excited mode evolves during T_{evol}. At this time, the ion is fully decoupled from the detection system. As mentioned before, the phase information at two different instances is required to extract the frequency, so short (∼100 ms)

[7] One should keep in mind that although the second pulse strength can be increased, the phase jitter also depends on the axial amplitude during the amplification pulse.

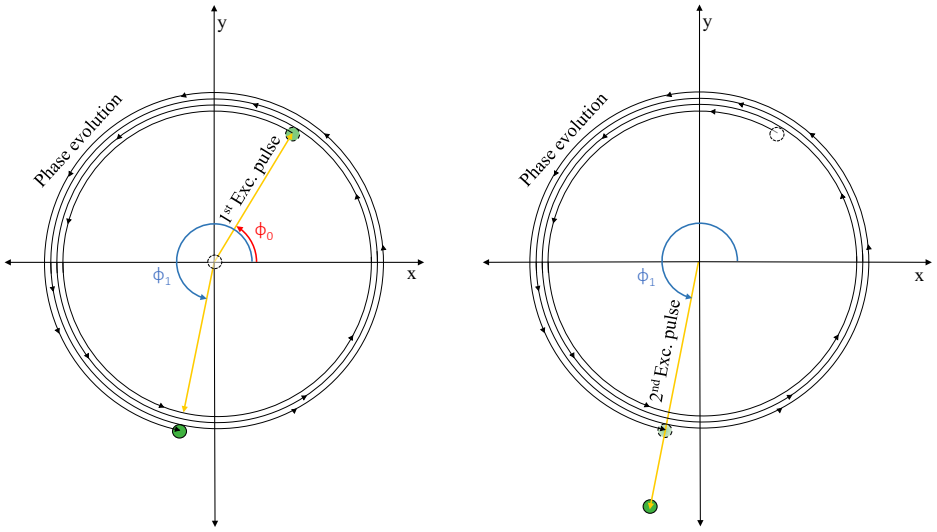

Figure 3.9. Radial phase dynamics during the PnA sequence. The first dipolar pulse at ω_+ excites the modified cyclotron mode and defines a phase ϕ_0. The phase then freely accumulates until a defined evolution time, when the acquired phase is ϕ_1. A few rotations of the ion during the phase evolution time are shown. Note that the amplitudes remain constant during this time; the rotations with increasing diameter are solely for visualization purposes. Then, on applying a second pulse, the amplitude of the modified cyclotron mode increases.

and long evolution times ($\sim$20 s) are used. The PnA cycles at the T_{evol}'s are repeated six times to reduce the statistical uncertainty. As phases can only be read as a factor of 2π, a phase unwrapping procedure is required to unambiguously determine the real phase, which necessitates additional measurements between the long and short evolution times (see [63] for more details). The long evolution times allow the determination of ν_+ with the highest precision. The longest possible evolution time is determined by the frequency fluctuations, which should not cause jitter $> 2\pi$ to keep the unwrapping procedure unambiguous.

Second pulse: The second coupling pulse $\omega_{\text{rf}} = \omega_+ + \omega_z$, leads to an exponential increase of the amplitudes of the modified cyclotron and axial modes and enables the transfer of phase information from the radial to the axial mode. The coupling drive used during this work had a pulse length ranging from 15 ms to 70 ms and amplitude of 1 Vpp. The transfer of phase information occurs, provided the modified cyclotron mode radius and axial mode amplitude after the evolution time and just before the coupling pulse follows the relation $\hat{z}_{\text{final}} > \sqrt{\frac{\omega_+}{\omega_z}} r_{+,\text{initial}}$.

Signal detection: The excited axial mode after the second pulse appears as a peak signal over the thermal noise of the resonator, which is read out using a Fourier analyzer with an acquisition time of 512 ms. A complex FFT of the detected signal holds the axial phase information and, consequently, the phase information of the modified cyclotron mode. To optimize SNR, the signal is read out with negative electronic feedback applied to the resonator (see section 3.2.5). Such a feedback is also necessary during the amplification pulse

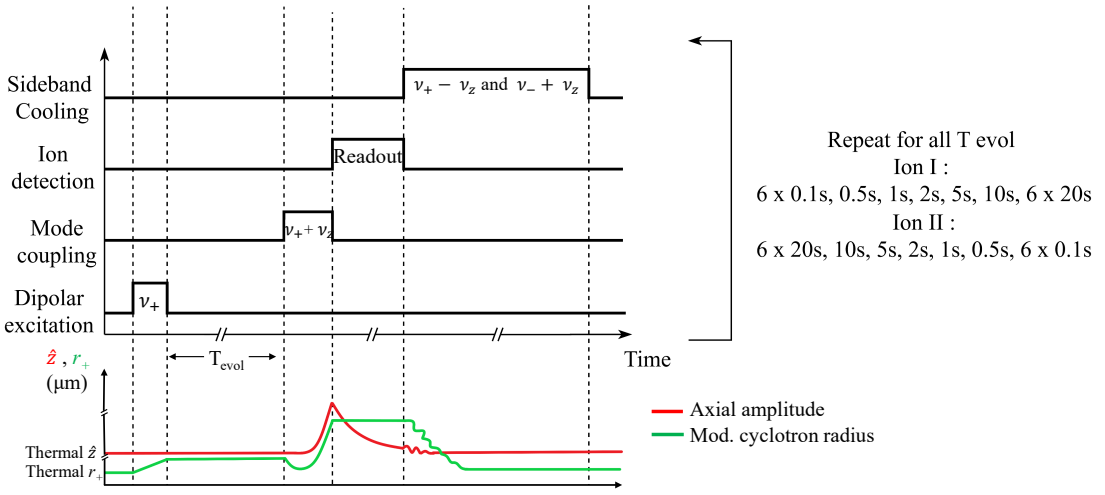

Figure 3.10. PnA pulse routine and scheme of parametric amplification. The pulse sequence of a single PnA cycle is shown. Every measurement cycle consists of 17 such PnA cycles, each performed with different evolution time. An overview of the changes in the amplitude of the axial and modified cyclotron mode during the PnA sequence is also shown.

to minimize the axial amplitude.

Cooling: The modified cyclotron mode and the magnetron modes are cooled via sideband coupling (see section 3.2.3), each for about 15 s.

To find optimum settings for the different excitation strengths with a reasonable SNR and phase jitter of the output signal, the r^+_{exc} during the evolution (given by D_x pulse) and the amplitude of the coupling pulse (given by Q_{xz} pulse) are both varied. As the amplitudes are increased, trap anharmonicities start to play a role, and as the amplitudes are reduced, read-out jitter plays a role (see section 6.6). Usually, the amplitude widths are set, and the excitation pulse lengths are varied to avoid any systematic effect from the non-linearities in the voltage output of function generators. The longest possible duration of the pulse length is limited by the modified cyclotron or axial frequency fluctuation: $T_{\text{exc}} \ll {}^1\!/\!\delta\nu_{+/z}$.

Using such a phase-sensitive technique has more advantages, as the phase information is extracted from the maximum of the peak signal. Thus, no lineshape model is involved, unlike the double-dip technique. Furthermore, the measured phase corresponds to the modified cyclotron mode and does not rely on the axial frequency directly. Therefore, the uncertainties in the axial frequency related to the dip lineshape or voltage fluctuations do not strongly affect the cyclotron frequency determination.

3.4 Temperatures of the eigenmodes and relativistic effect

Temperature is typically defined as a statistical property that emerges from the behavior of large samples or an ensemble of particles (atoms, molecules, or ions). Thus, when considering a single ion, the concept of temperature becomes less straightforward. This is where the ergodic hypothesis becomes particularly relevant, which states that the time average of

a system's observable property is equivalent to the average of the same property across a large ensemble of similar systems. The ergodic hypothesis connects the statistical behavior of a system over time to the behavior of an ensemble of similar systems. Thus we can relate the temperature (time-averaged) of an ion to the temperature of an ensemble of ions.

As discussed in the previous sections, a trapped ion in our Penning trap is detected and thermalized with the tank circuit through resistive cooling (see section 3.1.4). When the ion is in thermal equilibrium with the tank circuit, it is essentially in equilibrium with the electron gas (ensemble) temperature of the tank circuit. Thus, if the ion's energy E is measured many times, the result would be a Boltzmann distribution characterized by the temperature T of the tank circuit (electron gas), resulting in

$$\langle E \rangle = k_B T, \tag{3.39}$$

where $\langle E \rangle$ is the mean value of the total energy and k_B is the Boltzmann constant. If repeated measurements of the ion energy are performed, it will follow a thermal distribution governed by the exponential $e^{-\frac{E}{k_B T}}$. The probability density is

$$p(E) = \frac{1}{k_B T} e^{-\frac{E}{k_B T}}. \tag{3.40}$$

During this thesis work, an axial detection system was used, which was cooled to $4.2\,\mathrm{K}$ by a liquid helium bath. It can be made lower with the help of electronic feedback. Therefore, equation Eq. (3.39) and Eq. (3.40) can be rewritten in terms of the axial temperature T_z as

$$\begin{aligned} \langle E_z \rangle &= k_B T_z, \\ p(E_z) &= \frac{1}{k_B T_z} e^{-\frac{E_z}{k_B T_z}}. \end{aligned} \tag{3.41}$$

From the quantum mechanical expression for the axial energy given in Eq. (2.22) and Eq. (3.41), the mean quantum number is estimated. Assuming an axial temperature of $4.2\,\mathrm{K}$, $\langle n_z \rangle \approx 2 \times 10^5$. Due to such large quantum numbers, classical treatment of the system is justified.

As described in section 3.2.3, the coupling of the axial mode to the radial modes with a suitable quadrupolar drive at the sideband frequency could be used to cool the radial modes. In this process, an energy transfer between the modes occurs, and the quantum numbers of both modes tend to converge such that $\langle n_\pm \rangle = \langle n_z \rangle$, depending on which mode is cooled. Then, from Eq. (2.22),

$$\begin{aligned} \langle E_\pm \rangle &= \pm\, \hbar\omega_\pm \left(\langle n_\pm \rangle + \frac{1}{2} \right) = \pm\, \hbar\omega_\pm \left(\langle n_z \rangle + \frac{1}{2} \right) \\ &= \pm\, \frac{\omega_\pm}{\omega_z} \hbar\omega_z \left(\langle n_z \rangle + \frac{1}{2} \right) \\ &= \pm\, \frac{\omega_\pm}{\omega_z} \langle E_z \rangle \end{aligned} \tag{3.42}$$

Table 3.1. A summary of the frequencies, temperatures, amplitudes and energies of $^{12}C^{6+}$ and $^{4}He^{2+}$ for the eigenmodes. The parameters are estimated assuming 4.2 K temperature for the axial mode of the ions. The frequencies correspond to a trapping potential of -7.79 V and a magnetic field of 3.76 T. For details, see text.

	Frequency $^{12}C^{6+}$ / $^{4}He^{2+}$ (Hz)	Temperature (K)	Thermal amplitude (μm)	Energy (meV)
ν_z	468381 / 468229	4.2	45	0.36
ν_-	3795 / 3795	-0.034	5.7	-0.003
ν_+	28904530 / 28885728	259	5.7	22.3

Applying the relation between energy and temperature according to Eq. (3.39), the temperatures of the radial modes are then

$$T_\pm = \pm \frac{\omega_\pm}{\omega_z} T_z. \tag{3.43}$$

The temperatures are then given by the frequency ratio times the axial temperature. The negative 'temperature' of the magnetron mode corresponds to its negative energy $\langle E_- \rangle = k_B T_- < 0$ (see section 2.1.2). If the radial energy is measured multiple times, it would also result in a Boltzmann distribution analogous to axial energy but scaled by the frequency ratio $\frac{\omega_\pm}{\omega_z}$.

$$p(E_\pm) = \pm \frac{\omega_z}{k_B \omega_\pm T_z} e^{\mp \frac{E_\pm \omega_z}{k_B \omega_\pm T_z}}. \tag{3.44}$$

Therefore, when all three eigenmodes have been cooled by the axial resonator, the temperatures are given by Eq. (3.41) and Eq. (3.42). The measurement of the temperatures of the ion is discussed in section 5.4.

Thermal amplitudes:

On comparing Eq. (2.19) and Eq. (3.41) the averaged axial amplitude can be derived as

$$\langle \hat{z} \rangle = \sqrt{\langle \hat{z}^2 \rangle} = \sqrt{\frac{2 k_B T_z}{m \omega_z^2}}. \tag{3.45}$$

Similarly on comparing Eq. (2.20), Eq. (2.21), Eq. (3.42) and Eq. (3.45) the averaged radial amplitudes can be derived as

$$\langle r_+ \rangle = \sqrt{\frac{\omega_z}{\omega_+}} \langle \hat{z} \rangle \quad \text{and} \quad \langle r_- \rangle = \sqrt{\frac{2\omega_-}{\omega_z}} \langle \hat{z} \rangle = \sqrt{\frac{\omega_z}{\omega_+}} \langle \hat{z} \rangle. \tag{3.46}$$

3.4.1 Relativistic shift

So far, in this thesis, the motion of a particle has been treated with a non-relativistic approach. In this section, the influence of the motional degrees of freedom of an ion due to special relativity (relativistic mass increase) on the motional frequencies will be examined.

Even in an ideal trap or a well-tuned trap with no electrostatic anharmonicity and magnetostatic inhomogeneity, the relativistic effects will disrupt the harmonicity and cannot be tuned, leading to frequency shifts. A detailed derivation of the relativistic frequency shifts can be found in [58, 59, 89]. A summary of the frequency shift (in first order) based on the relativistic mass increase is as follows:
Firstly, for a particle of rest mass m moving with velocities v much smaller than that of light c, the relativistic mass is

$$m_{\text{rel}} = \gamma m = \frac{m}{\sqrt{1-\frac{v^2}{c^2}}} \approx m\left(1+\frac{v^2}{2c^2}+...\right) \tag{3.47}$$

such that,

$$\frac{\Delta m}{m} \simeq \frac{v^2}{2c^2}. \tag{3.48}$$

The relativistic shift by and from the modified cyclotron mode is of the most importance, and the shifts related to the axial and magnetron mode can be safely neglected. From Eq. (2.11) and Eq. (3.48)

$$\frac{\Delta\omega_+}{\omega_+} = -\frac{\omega_+}{\omega_+-\omega_-}\frac{\Delta m}{m} = -\frac{\omega_+}{\omega_+-\omega_-}\frac{v^2}{2c^2}. \tag{3.49}$$

Rewriting in terms of amplitude and frequency:

$$\frac{\Delta\omega_+}{\omega_+} \approx -\frac{\omega_+^2 r_+^2}{2c^2} \approx -\frac{E_+}{mc^2}.$$

From Eq. (2.10) and Eq. (3.48)

$$\frac{\Delta\omega_z}{\omega_z} = -\frac{\Delta m}{2m} \simeq -\frac{v^2}{4c^2}. \tag{3.50}$$

Now from Eq. (2.1) and Eq. (3.48)

$$\frac{\Delta\omega_c}{\omega_c} = -\frac{\Delta m}{m} \simeq -\frac{v^2}{2c^2} \approx \frac{\Delta\omega_+}{\omega_+}. \tag{3.51}$$

Although the relativistic effects are relatively small due to the slow motion of the particle compared to the speed of light, they are notably large and are of importance as the frequencies are measured with high precision. For instance, for a particle excited to $80\,\mu$m[8], $\frac{(\omega_+ r_+)^2}{2c^2} \approx 1.2\times10^{-9}$, which is significant. The frequency shifts are especially large for lighter ions like the ones measured at LIONTRAP as the relativistic shift is inversely related[9] to the mass. Sections 6.3.1 and 6.4.1 address how the effect of special relativity is treated in the mass measurement.

[8] It is the largest modified cyclotron radius used during the mass measurement
[9] A decrease in mass causes an increase in the frequency shifts

4. Experimental apparatus

In the previous chapters, the motivation and principles of high-precision measurements were introduced. This chapter discusses the experimental apparatus, the trap system, and all the technical support that enables a high-precision (cyclotron frequency) measurement.

The LIONTRAP setup is an upgraded version of the predecessor *g*-factor experiment in Mainz. A new trap system was developed in 2016, keeping mass measurements of light ions in focus. The first successful measurement using this setup was the proton mass and the mass of oxygen [21], followed by the deuteron and the HD molecular ion masses [22]. This mass measurement setup is detailed in [19] and will be discussed in this chapter. Fig. 4.1 shows the overview of the experimental setup, and on the left of the image, a cross-sectional sketch of the magnet with the apparatus is illustrated. The different components of the experimental setup are described in the following sections.

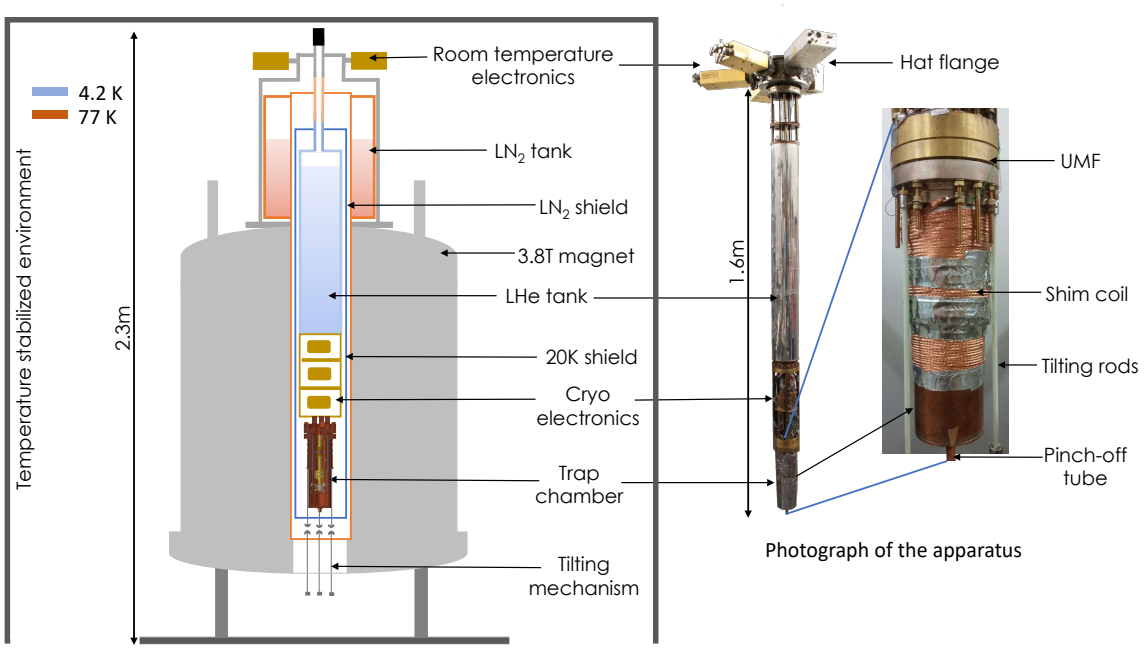

Figure 4.1. A sketch of the main experimental setup. On the left side, an overview of the setup, consisting of the superconducting magnet, the cryostats, and the apparatus, is shown. The apparatus includes the room-temperature electronics hat, the cryoelectronic section, and the trap setup inside the trap chamber. The experimental setup is placed in a temperature-stabilized environment. In the center, a photo of the apparatus is shown before inserting it into the magnet. The photo of the closed trap chamber screwed and sealed to the UMF is on the right. The shim coil is also placed around the trap chamber and is wrapped with a copper braid to ensure efficient heat conduction.

4.1 The magnet and the cryostats

A warm bore superconducting magnet charged to $3.76\,\mathrm{T}$ provides the magnetic field for the experiment. The magnet was charged in 1995, and ever since it has been maintained in persistent mode[1] at cryogenic temperatures without any discharging cycle. The experimental apparatus is vertically placed into the magnet's bore and cooled to cryogenic temperatures with the help of liquid nitrogen and liquid helium cryostats. The liquid nitrogen cryostat is placed on top of the magnet, and the liquid helium cryostat is part of the apparatus. The hat of the experiment, where the boxes that contain several room-temperature electronics are connected, forms the top part of the apparatus. The hat rests on the liquid nitrogen cryostat and helps to fix the apparatus inside the magnet, see Fig 4.1. The magnet's bore is vacuum pumped to create an insulation vacuum of $<10^{-5}\,\mathrm{mbar}$. This vacuum between the cryostat stages and the room-temperature chamber walls ensures that there are no convection losses. The main apparatus, which consists of the trap chamber and the cryoelectronics, is maintained at $4.2\,\mathrm{K}$ with the help of the liquid helium reservoir inside the magnet's bore. However, a large thermal load could be generated due to thermal radiation from warm surfaces around the $4\,\mathrm{K}$ stages, such as the magnet's bore at $300\,\mathrm{K}$. According to Stefan Boltzmann's law, the total radiant heat energy emitted by a body is proportional to T^4, where T is the absolute temperature. Therefore, intermediate heat shields at $77\,\mathrm{K}$ and $20\,\mathrm{K}$ are placed. The $77\,\mathrm{K}$ shield is in direct contact with the liquid nitrogen reservoir, which serves as the outermost thermal stage and actively cools the shield. To further reduce the heat load on the liquid helium cryostat, a $20\,\mathrm{K}$ shield is attached between the $77\,\mathrm{K}$ shield and the trap setup and cooled using evaporated helium gas. The $20\,\mathrm{K}$ shield is connected to the liquid helium filling tube. The largest thermal load arises from the connections between the $4.2\,\mathrm{K}$ stage to room temperature. Such transitions are minimized to the connections of the electronics and the filling tube of the liquid helium reservoir, which also acts as the point of suspension of the experiment. The filling tube is also connected to the helium recovery line for the liquefaction of the evaporated helium. The superconducting magnet and the cryogenic reservoirs were taken over without significant modifications from the g-factor experiment.

4.2 The multi Penning trap system: trap tower

The most crucial component of the experimental apparatus is the Penning trap system. The trap tower consists of 38 electrodes stacked together. This stack of electrodes consists of the Precision Trap (PT) with two Storage Traps (ST-I and ST-II) on either side of it, the Magnetometer Trap (MT), several transport electrodes, and a miniature electron beam ion source (mEBIS) which includes of a Creation Trap (CT) and a field-emission point (FEP) electron source. The MT, ST-I, ST-II, and most parts of the mEBIS are repurposed from the preceding g-factor experiment. The individual sections of the trap setup will be detailed in

[1] No power supply was connected since 1995.

the following sections. A sketch of the complete trap setup is shown in Fig. 4.2.

4.2.1 Trap chamber

The trap tower is placed inside a trap chamber at the most homogeneous magnetic field region. The trap chamber is a vacuum chamber made of OFHC[2] copper that separates the excellent, hermetically sealed, and cryopumped trap vacuum from the isolation vacuum between the cryogenic components and the room-temperature chamber walls. The trap chamber on the upper side is screwed and sealed with indium to a feedthrough flange named UMF[3], which has several feedthroughs for all voltage, excitation, and signal lines to or from the trap tower. A pinch-off tube is welded into the bottom of the trap chamber. A photograph of the trap chamber used in the experiment is shown on the right side of Fig. 4.1. Initially, the trap chamber is evacuated via this tube to Ultra High Vacuum conditions ($10^{-12} < p < 10^{-7}$ mbar). Once pumped, the tube is pinched off, forming a cold-welded seal and hermetically sealing the trap chamber at room temperature. On cryopumping (4.2 K), all the rest gases freeze onto the walls of the vacuum chamber, creating eXtremely High Vacuum ($p < 10^{-12}$ mbar). The pressure inside the trap chamber is $< 10^{-17}$ mbar, which can only be estimated from the lack of charge exchange of the stored ion with the residual gases. This exceptional vacuum enables the storage of a single ion for several months such that the ions are only lost due to technical glitches.

4.2.2 Precision Trap

The Precision trap (PT) is where high-precision measurements of the eigenfrequencies are performed. It is a seven-electrode trap with two sets of correction electrodes capable of creating a highly harmonic potential (section 2.2.1.1). The two sets of correction electrodes allow to minimize or null the anharmonicity coefficient C_4 and C_6, and the geometry is designed such that the other even-order higher coefficients, C_8 and C_{10}, are nominally zero. The endcaps on either end of the trap are partitioned into three shorter rings in order to facilitate slow adiabatic transport of ions. The inner correction electrodes and ring are azimuthally split electrodes for excitations and frequency detection (section 4.4). Compared to the other traps inherited from the g-factor experiment, the PT has a slightly larger radius $r = 5$ mm. The larger radius helps to reduce the systematic image charge shift (section 3.1.9). The particulars of the trap design are discussed in [63] and [19].

4.2.3 Storage Traps

The Storage Traps ST-I and ST-II are situated on either side of the PT. These traps are used to store ions that are not currently measured. The storage traps enable high-precision cyclotron frequency measurements of the two ions very close in time. See section 6.2 for details. The ST-I is a five-electrode trap with correction electrodes. The ST-I has a split correction

[2] Oxygen Free High Conductivity
[3] Unterer Montage Flange

electrode integrated with a detection system and excitation lines (see section 4.4). Thus the ions in this trap can be manipulated. In contrast, ST-II is a simple three-electrode trap only used to store an ion. Below the MT is a set of three electrodes (ST-III) that can be potentially used to store an ion, but in this work, it was only used as transport electrodes.

4.2.4 Magnetometer Trap

The Magnetometer Trap (MT) is a five-electrode trap with a pair of correction electrodes. The trap is almost identical to the ST-I. It is equipped with excitation lines and detection electronics (see section 4.4). The purpose of the MT was to monitor the magnetic field fluctuations by performing independent phase-sensitive measurements of the cyclotron frequency of a third ion in reference to the ions of interest and, in turn, improving the statistical precision. However, this method described in [90] did not lead to the anticipated improvement. The MT was not extensively used during this work. It was only used to perform test measurements, store ions during production, or as transport electrodes.

4.2.5 mEBIS: miniature Electron Beam Ion Source

The cryopumped, hermetically sealed trap chamber does not allow the injection of ions from an external source into the trap. Thus a miniature electron beam ion source produces the ions in situ [91]. The mEBIS is the lowest part of the trap tower; see Fig. 4.2. It consists of a Field Emission Point (FEP) to produce an electron beam. Applying a voltage difference between FEP and the acceleration electrode generates an electric field at the tip of the FEP, which prompts the electrons to tunnel into the vacuum and accelerate towards the acceleration electrode and the target. The electrons pass through a 700 µm hole in the target and are reflected by the high voltage on the reflector electrode. The reflector is biased a little higher than the voltage of FEP. The electrons then start to oscillate between the FEP and reflector along the magnetic field lines. Consequently, the space charge density increases along the beam and causes the beam to widen until it finally impinges on the target surface. The target is made of an electrically conductive carbon nanotube-filled plastic compound (TECAPEEK[4]) and surface coated with different materials and techniques depending on the ions of interest [22]. The impinged electrons on the target surface ablate different species of atoms and molecules, which get ionized by the electron beam. The highest electron beam energy used during this campaign was 1 keV. Electron beam energies up to 2 keV can be used reliably. Those atoms that get ionized within the trapping region of the Creation Trap (CT) get trapped and are further ionized due to electron impact ionization creating ions at higher charge states. The CT is a simple three-electrode trap comprising a ring and two endcaps. The ion cloud, consisting of a large variety of ions generated from the target surface, is stored in the CT. It is later adiabatically transported to the PT, where a single ion is prepared. For the voltage configurations employed in ion production for this work, see section 5.1.

[4] A high-performance thermoplastic: polyetheretherketone (PEEK)

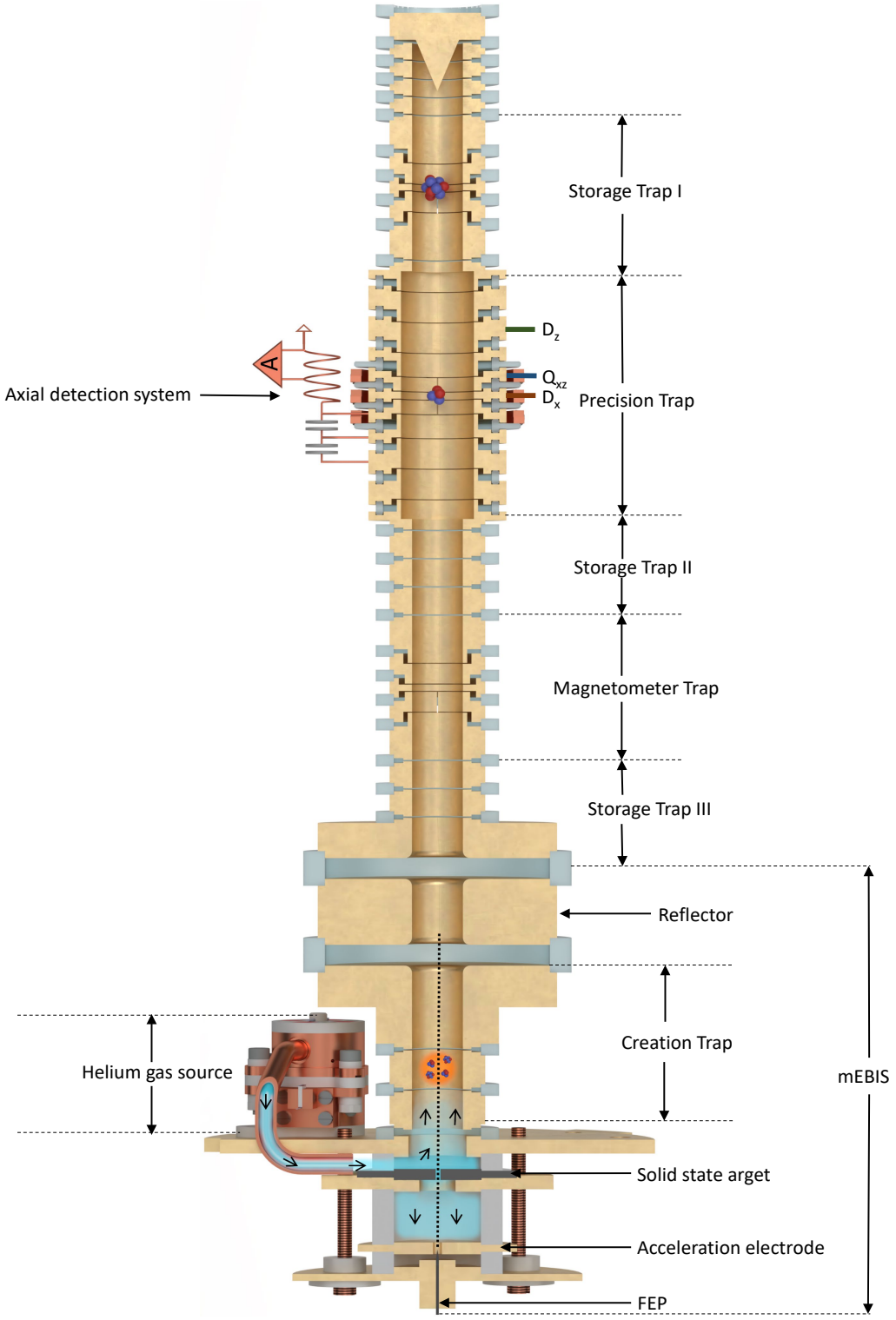

Figure 4.2. Sketch of a sectional view of the trap setup. The mEBIS produces ions in situ, and the helium gas source enables the production of ^{4}He ions. By heating the source, gas atoms (blue) are released and guided into the electron beam (dotted black line), which the FEP produces. Additionally, this electron beam ablates and ionizes atoms from the surface of the target. The ion cloud (orange-shaded spot) is then trapped and stored in the CT and later adiabatically transported to the PT to prepare single ions. The MT was not used in this work. The different ions of interest are stored in separate traps simultaneously. The tank circuit (brown), the cryogenic amplifier system, and the excitation lines in the PT are also shown. The figure is adapted from S.Sasidharan *et. al.*, accepted 2023 [92].

However, the above-discussed production technique only works for atoms that can be bonded to a solid-state target. For our candidate of interest, helium, which is gaseous at room temperature, a new method had to be developed, which is explained in section 4.3.

4.3 Source for gaseous atoms: helium source

The ion production technique using the solid-state target is ineffective for elements in the gaseous state, such as inert gases. This is because the gaseous atoms have very weak bonding capabilities. Moreover, the introduction of a gaseous source inside the trap chamber comes with several challenges and requirements, such as:

- Gas has to be contained and stored inside a closed system and loaded into the trap chamber at room temperature.
- The gas should not deteriorate the cryogenic vacuum quality.
- Controlled release of gas should be possible on demand.
- The mechanism should utilize minimum space due to the limited capacity within the trap chamber.

To comply with these requirements, we have developed a method utilizing the adsorption capabilities of such gases, especially helium, on an adsorption agent such as activated charcoal at $4\,\mathrm{K}$. The highly porous nature of activated charcoal allows it to have vast surface areas starting from $500\,\mathrm{m^2\,g^{-1}}$ to $2000\,\mathrm{m^2\,g^{-1}}$ for adsorption. With our method, the gas is initially contained in a small volume that also contains activated charcoal pellets. However, at room temperature, the gas adsorption by the activated charcoal pellets is negligible. In contrast, at $4\,\mathrm{K}$, the gas mostly adsorbs onto the charcoal surface [93]. Then, the container with gas can be opened with almost no gas released into the trap chamber as it is frozen out on the charcoal. Upon increasing the temperature of these pellets, one could desorb the gas; for example, the desorption of helium gas begins at 20-50 K [94]. See Fig. 4.2.

4.3.1 Working of the source

The construction of the source includes mainly two sections:

- A sealed gas storage chamber containing the gas along with activated charcoal pellets.
- A piercing mechanism that holds a titanium needle (piercing head) to open the sealed chamber to release the gas.

Preparation of gas storage chamber The charcoal pellets are fixed inside the gas storage chamber with heat-conductive glue. A $30\,\mu\mathrm{m}$ thick copper foil is then soft-soldered onto the top of the chamber to seal it. The gas storage chamber has a tube with an inner diameter of $2\,\mathrm{mm}$ and an outer diameter of $3\,\mathrm{mm}$ hard soldered for filling the gas, which is later pinched-off to seal the gas storage chamber completely. The chamber and charcoal pellets are baked at a temperature of $130\,^{\circ}\mathrm{C}$ for about $2\,\mathrm{h}$ to remove residual gases on the surfaces before filling the gas of interest (helium gas). A $100\,\mathrm{mbar}$ of gas is filled into the $0.3\,\mathrm{ml}$ volume of the gas storage chamber, corresponding to $\sim 7 \times 10^{17}$ atoms. A schematic of the setup used to

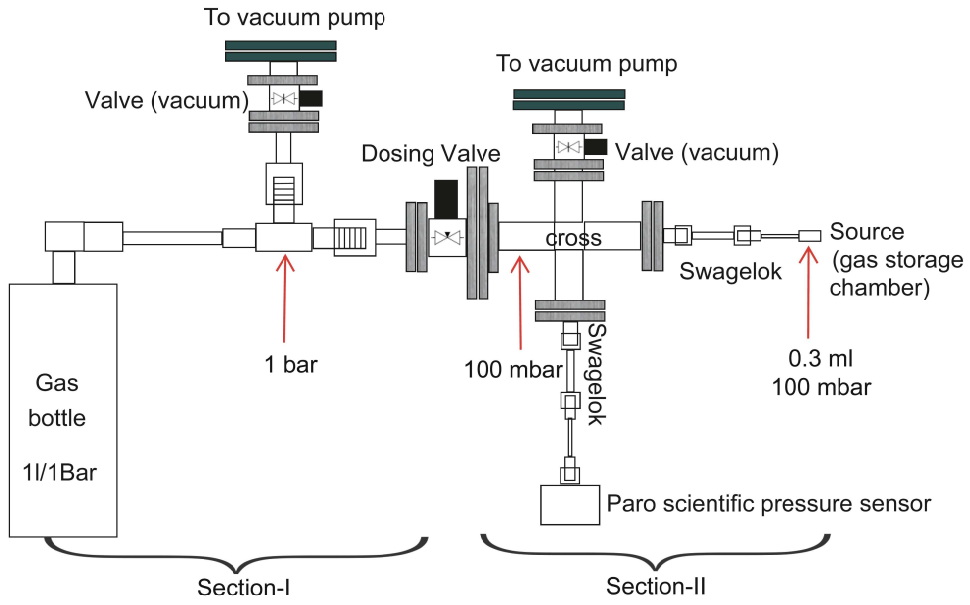

Figure 4.3. Schematic of the setup used for filling the gas storage chamber of the source. Initially, the dosing valve and the gas bottle are entirely closed, and the vacuum pump in section-II is turned on. The source is wrapped with baking wires which are heated and maintained at 130 °C for 1 to 2 hours to release any absorbed moisture and residual gases. Once the baking process is stopped, the vacuum pump from section-I is also turned on to evacuate all parts. Once a good vacuum is achieved, both vacuum valves at the pumps are closed, the gas bottle is opened to fill the small volume in section-I with gas, and the gas bottle is closed again. The dosing valve is then very carefully opened to fill 100 mbar of gas into the source with the help of a highly sensitive pressure sensor. Once filled with gas, the tube on the source is pinched-off.

perform baking and filling gas in the chamber is depicted in Fig. 4.3.

Preparation of piercing mechanism A slender wire is passed through the titanium needle, which presses on a copper-beryllium spring. This thin wire is soldered on either side using a low-temperature solder (Indium 66.3% . Bismuth 33.7% solder ; Melting point 72 °C). One side of the wire is attached to a heating resistor which helps to melt the low-temperature solder to trigger the needle (see Fig. 4.5). This is placed inside a copper housing to guide the needle onto the copper foil. A detailed design of the gaseous source is shown in Fig. 4.4, and a few photographs of the source in preparation and after tests are shown in Fig. 4.5.

Once prepared, the source is placed inside the trap chamber[5] and cooled down along with the experiment. To activate the source, the low-temperature solder connection can be melted by supplying ~ 100 J of heat energy with the help of resistors. The molten solder releases the titanium needle held by the spring, which pierces the foil below, opening a channel to release the gas. However, the helium gas is still adsorbed in the charcoal at 4 K. Only when

[5]Due to the lack of available feedthroughs, the heating resistors for the piercing head and the gas storage chamber were connected to a single feedthrough. The connections were made through two diodes so that individual resistors could be used by manipulating the supply voltage.

applying about 1 W of power to a heating resistor for 45 sec the temperature of the charcoal increases sufficiently to release the gas through the pierced opening. It is guided towards the electron beam in the mEBIS, where the atoms are ionized.

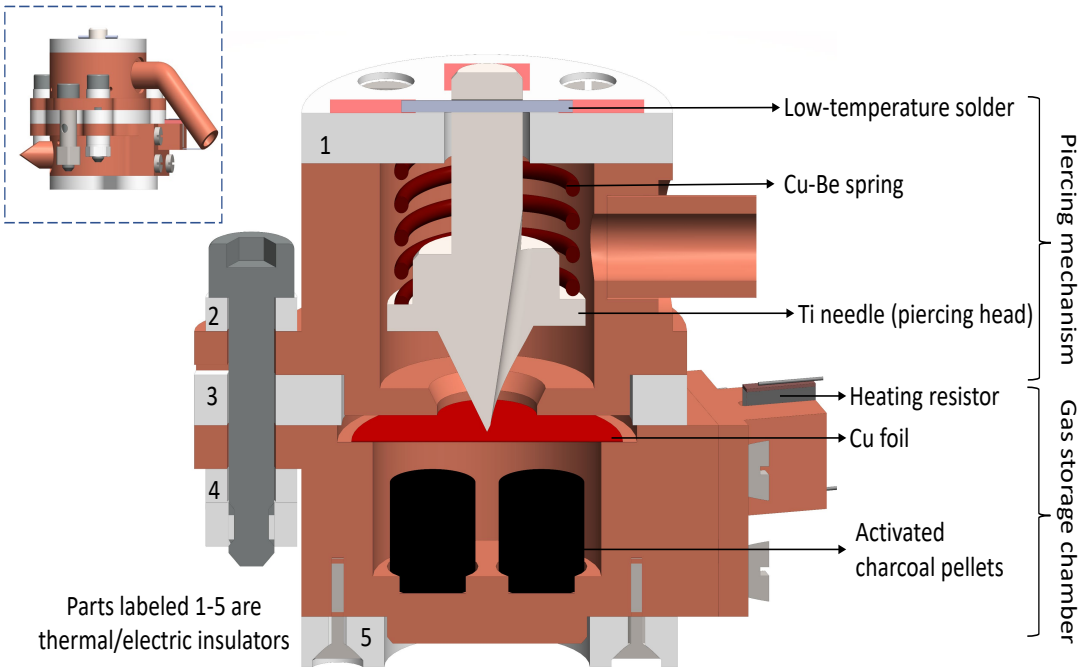

Figure 4.4. A sketch of the sectional view of the source for gaseous species. All the crucial components are labeled, and the text describes the working principle. The complete construction of the source is illustrated in the upper left corner.

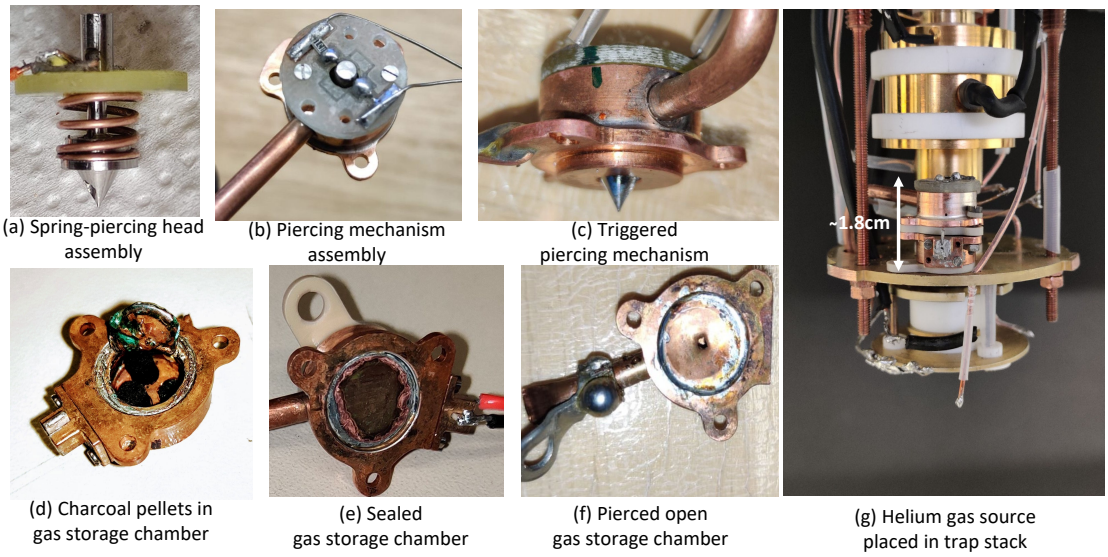

Figure 4.5. Some photographs of the source in preparation are shown in (a), (b), (d), and (e). In (c) and (f), the photographs of the piercing mechanism and the gas storage chamber are shown after the titanium needle is triggered. In (g), the assembled source is fixed on the trap stack holder.

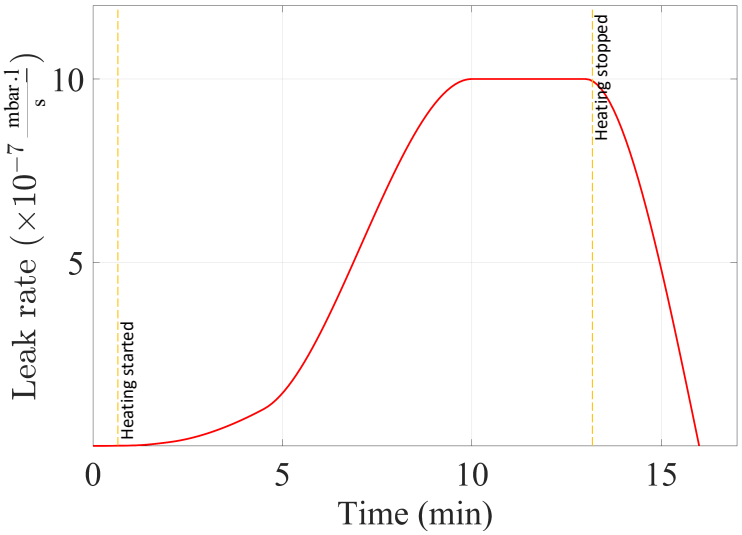

Figure 4.6. The plot shows the result of an example heating cycle in the cold head test. The leak rate is detected using a rest gas analyzer at different stages of the heating (and cooling). The leak rate represents the amount of helium we can release once the source is cooled down in the trap chamber. The plot also indicates that we have control over heating and thus release helium according to demand.

The working of the source was tested in a test stand with a cryogenic cold head where the leak rate of helium gas was studied using a rest gas analyzer. In the test, with a heating power of 1 W, a leak rate of 10^{-9} mbar l s^{-1} was observed in 45 sec, which gradually increased to 10^{-6} mbar l s^{-1} in 5 minutes and remained at this rate until heating was stopped. No gas was detected 2 to 3 minutes after the voltage for heating was turned off. Many such heating cycles were repeated, and it took at least 30 minutes of continuous heating to empty the source. An example of such a heating cycle is summarized in Fig. 4.6.

This source was implemented in the experiment originally for ^{3}He atoms. As the measurement campaign started, the piercing head was activated, and many attempts to create ^{3}He ions took place. However, despite many attempts with different heating powers, we could not produce ^{3}He ions but always produced ^{4}He ions. During a thermal cycle after the measurement campaign of ^{4}He mass, we learned that the piercing mechanism had failed to operate correctly. The fault was mainly in heating the low-temperature solder. There was only a single resistor heating the wire (see Fig. 4.5), and it turned out that the side on which the resistor is connected melts and disconnects the wire holding the piercing head. As soon as it disconnects from one side, it cools rapidly, preventing heat conduction from melting the second spot of the solder to fully release the piercing head. More details and the modified mechanism correcting this issue are discussed in 6.8.1.1.

The heating mechanism on the gas storage chamber allowed the production of ^{4}He by heating the exposed surface of the chamber. The surface of the gas source was pre-heated by supplying a heating power of 200 mW for 45 sec and was kept at a higher temperature

to release helium atoms while the electron beam was switched on to ionize these atoms. Fig. 4.2 illustrates the production of helium ions.

4.4 Electronic components

The experiment requires several electronic components to operate. There are self-built and commercial devices and components in the room temperature and cryogenic sections. The detection systems, excitation lines, voltage sources, and the devices involved in measurement routines are discussed in the following sections. The room-temperature electronics are mainly assembled on the hat flange of the experiment, and devices used to run the experiment are placed on a rack near it.

4.4.1 RF detection electronics

There are 4 Radio Frequency (RF) detection systems connected to the trap tower, which are for axial mode detection. During this thesis, the axial detector in the PT was mainly used. The detection system consists of the LC resonator, a cryogenic amplifier, a room temperature amplifier, and a single sideband mixer for the axial signal. The down-mixed signal with a frequency of $\sim$15 kHz is analyzed by an audio analyzer (Stanford Research, SR1) which performs a Fast Fourier Transform (FFT) of the received signal. The downmixing of the signal is accomplished with the help of a local oscillator (see Fig. 4.9). The implementation of different resonators in the trap tower is described below, and the axial resonators' connections to the trap are shown in Fig. 4.7.

In PT: Two axial resonators (Ax1 and Ax2) were connected to the PT during this measurement campaign. Fig. 4.7 shows the connection of the resonator used to detect carbon

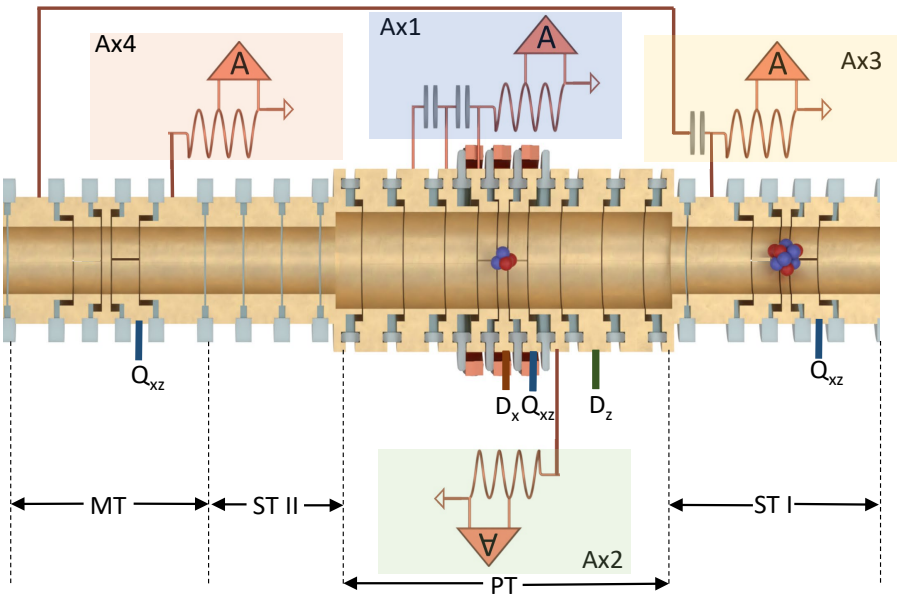

Figure 4.7. A sketch to depict the connections of different axial resonators to the traps. Primarily only the Ax1 detector was used for measurements. For details, see text.

and helium ions, denoted by Ax1. The three electrodes are chosen to have a small effective electrode distance of 9.6 mm. This resonator has an inductance of 3.36 mH, a quality factor of $\sim$2300, and an SNR of 16.5 dB. The resonance frequency was adjusted to the axial frequency of the respective ion using a varactor diode. The difference in the resonance frequencies to address both ions is 150 Hz. A second axial detector (Ax2) with an inductance of 2.0 mH was connected to the upper outer correction electrode. This resonator was connected to be able to address ions with significantly different q/m, for example, Cs^{10+}, with the help of a voltage doubler supplying the ring and the correction voltages.

In MT: An axial resonator (Ax3) with an inductance of 1.65 mH was connected to the lower endcap of the MT, enabling ion detection. Another axial mode detector for electrons (Ax4) with an inductance of 5.6×10^{-4} mH is connected to the upper endcap of the MT. The resonance frequency of this tank circuit was ~ 54 MHz, and a quality factor of ~ 770. This axial resonator for electrons was previously used as a cyclotron mode detector for protons.

In ST-I: The resonator connected to the lower endcap of MT is additionally capacitively connected to the lower endcap of the ST-I (Ax3). It thus gives a possibility to detect the ions and perform measurements. The lower correction electrode of ST-I is also capacitively connected to the split electrodes of PT. This coupling was done to have a possibility of electron cooling of the ion. The coupling is used to exchange energy between the electrons' cooled axial mode and the ion's cyclotron mode. An amplifier and a feedback line are also connected to the ST-I for the cooling of electrons. The principle of electron cooling was demonstrated in the outlook of [30], and the hardware connections were made in this cool-down to investigate it further. However, during this thesis, only the production and storage of electrons were tested, and no further step toward electron cooling was performed.

4.4.2 Voltage sources

Trap voltages: The high-precision DC voltages for the traps from 0 to -14 V are supplied by two UM1-14 voltage sources from Stahl-electronics [95]. The UM1-14 has 3 'precision channels'[6] and 10 add-on 'fast channels'[7]. The precision channels have a resolution of $\approx$ 1 µV (25-bit) and have fluctuations only on the relative 10^{-7} - 10^{-8} level. The precision channels of the UM1-14's supply the following electrodes:

- UM1-14-I: PT ring + PT inner correction electrodes (upper & lower supplied individually)
- UM1-14-II: PT outer correction electrodes (shared) + MT ring + MT correction electrodes (shared)

The PT's outer correction electrodes share a single precision mode channel. However, they can be manipulated separately by voltage mixing using a voltage divider. The same approach

[6] Three secondary precision channels are coupled to the primary precision channels via an internal voltage divider [95].

[7] All the precision channels can also alternately function as fast channels. Therefore, there are 10+3+3 fast channels in total.

is made with the correction electrodes of the MT, which share one precision mode channel of the UM1-14-II. All the other trapping voltages are provided by the fast channels of the UM1-14s, which have lower stability and resolution (16-bit) than the precision channels. However, the voltages on the endcaps, particularly for the PT, must also be stable. As the endcap electrodes are generally at 0 V, the stability can be simply achieved by shorting to ground via the 'shutdown mode' of the fast channels. The precision channels can operate in either 'precision mode' or 'fast mode'. The trap voltages are usually set in the precision mode, and the fast mode is mostly used while performing ion transports. The control software is used to switch between the different modes. The UM1-14s are placed inside the temperature-stabilized environment and shielded inside a copper box (see Fig. 4.1).

Voltages for electronic components in the cryo section: Furthermore, there are bias supplies, mainly the BS1-12 (16-bit resolution) and the BSHD (Locepps [96]) connected to the hat flange of the experiment. These supply voltages are for all the cryogenic amplifiers, cryogenic switches for the excitation lines (refer to section 4.4.3), and varactor diodes.

High voltage for ion production: The High-Voltage box (HV box) is placed on the hat flange and used only during ion production to supply and control the mEBIS. The HV box supplies acceleration voltages of several kV for the electron beam. The operation of mEBIS is discussed in section 4.2.5 and [91]. The voltages for the Creation Trap (CT) are provided by a separate high-voltage module named HVM (-100 to 0 V). The control voltages for HVM and HV box are supplied by the bias supply BS1-12. The stability of these voltages is low as they are not used for any measurement but only for the production of ions.

Filter boards: All the voltages are filtered via RC-low-pass filters twice before entering the trap chamber, once at room-temperature and again at 4 K.

4.4.3 Excitation lines

There are 4 types of excitation lines connected to the trap tower, which are discussed below.

Q_{xz} line: These excitation lines are used to deliver quadrupolar excitations that can be used to couple the axial and radial modes. However, the excitations are not purely quadrupolar but have additional dipolar components D_x and D_z and even a Q_{zz} component and thus can be used for different excitations. For example, the dipolar components can be used to address the radial and axial modes separately, and the Q_{zz} component can be used for parametric excitation ($2\omega_z$)[8]. The choice of the relevant field component is done via the frequency. An excitation at ν_+ only reacts to D_x, and at $\nu_+ - \nu_z$ only to Q_{xz} and so on. Due to the multiple features of this line, it can be used for direct excitation of the modified cyclotron or magnetron motion, cooling of the radial modes, and PnA measurements. Q_{xz} excitation lines are connected to one-half of the split upper correction electrode of the MT and ST-I

[8]The Q_{zz} drive introduces an additional effective potential which resembles a radiofrequency trap ("Paul trap"), in combination with the static potentials of a Penning trap.

and to one-half of the split inner upper correction electrode in the PT (see Fig. 4.7). Only the Q_{xz} line in the PT was used during the mass measurement to provide the PnA excitation pulses. A dual-channel Arbitrary Waveform Generator (AWG), Agilent 33600A, generates the excitation signals for PnA measurement; see section 4.4.4. The Q_{xz} excitation line of PT is connected to the AWG through a power splitter/combiner of Mini-Circuits (ZSC-2-2+). One of the channels provides the first pulse (D_x at ν_+), and the other channel is programmed with the phase evolution time and waiting times followed by the second PnA pulse (Q_{xz} at $\nu_+ + \nu_z$).

$\mathbf{D}_z$ line: This excitation line provides strong axial dipolar excitations and is mainly used during the ion production and cleaning process; see section 5.1.2. A D_z excitation line is connected to the innermost upper endcap electrode (Fig. 4.7). An AWG, Agilent 33250A, produces the excitation signals. The D_z line is also used to excite the ion for axial peak detection during measurements when required.

$\mathbf{D}_x$ line: The dipolar excitation line is used for strong dipolar excitations in the radial direction. A D_x excitation line is connected to one-half of the split ring electrode (Fig. 4.7). The corresponding excitation signals are given using an AWG Agilent 33600A channel when required.

LC line: This excitation line is not connected to the trap directly but acts as an antenna (weak coupling) to the resonators. It is used to change the effective temperature of the resonator and, thus, the ion through negative feedback on the detection system; see section 3.2.5. A separate waveform generator AWG Agilent 33250A supplies the local oscillator signal of the feedback, which defines the phase. The feedback amplitudes are adjusted using attenuators. Only the feedback line connected to the used axial resonator in the PT was active.

4.4.3.1 Cryogenic switches

All the excitation lines are connected to the electrodes via cryogenic switches. These switches make it possible to ground the excitations line in the cryogenic electronic section when not used. The switches were established to reduce the radio frequency noise coupling to the trap [75]. The switching circuits are based on GaAs solid-state switch (SW239). An example of the switch implementation is depicted in Fig. 4.8. The lines are connected to the trap through a capacitive voltage divider which allows the reduction of noise. The circuit also includes the DC biasing for the corresponding electrode.

The excitation lines are, therefore, always connected to the trap electrodes through capacitors. In the ‘on state’ (open), the switch is high ohmic and passes the signal to the electrodes, and allows a strong coupling. In the ’off state’ (closed), the line is grounded, and the signal is strongly suppressed. However, depending on the state of the switch and the amplitude, the excitation is partially rectified by the nonlinear JFET in the switch. This rec-

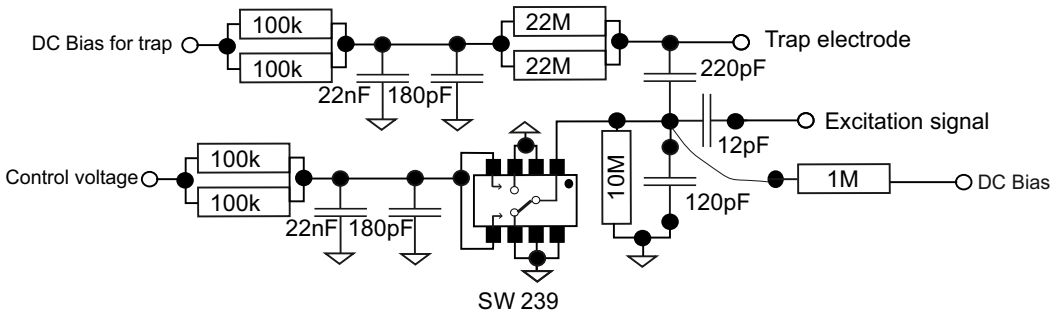

Figure 4.8. The excitation lines and feedback lines are connected through switches implemented as depicted in the circuit shown in the figure.

tification causes a sudden change in the DC. Despite the presence of a capacitor to remove DC after the switch, an excitation pulse, such as the ones used during PnA cycles, causes a DC burst at the start and end of the excitation (altering the mean of the signal), which can partially propagate (momentarily) to the trap side. This issue results in a chirp of the axial frequency after and during every excitation pulse. It is especially troublesome for PnA measurements with short evolution time in the order of tens of milliseconds. The implications of this effect were thoroughly investigated in [65]. This behavior of the switch could be corrected to some extent by supplying a bias voltage to the hot end of the switch, which is the drain of the JFET. After measuring the dependence of this voltage on the excitation signal, a bias voltage line was added via $1\,\mathrm{M}\Omega$ resistance to the hot end of the switch, and a 3V at this line could significantly reduce the rectification.

However, this effect is strongly inhibited when the switch is in the off state. The PnA sequences during the mass measurement campaign have been performed with the switch in the off state, and the influence of this effect is negligible. The short evolution times in this measurement campaign were anyhow increased to $100\,\mathrm{ms}$ from $10\,\mathrm{ms}$ used in the previous campaigns to avoid any effects from this rectification action.

4.4.4 Time reference and device setup for PnA measurement

To provide a common reference time to all devices that generate frequencies and pulses, as well as the FFT analyzer, they are synced with a $10\,\mathrm{MHz}$ signal of a rubidium atomic clock (FS725 by Stanford Research Systems). The distribution of the $10\,\mathrm{MHz}$ signal is fulfilled using a dual distribution amplifier (FS735 by Stanford Research Systems). The clock also provides an output signal of 1 pulse per second (pps), which forms a reference for the trigger pulses generated by a pulse-delay generator (BNC555 by Berkeley Nucleonics Corporation). The BNC has multiple triggering channels, which are used for triggering the PnA pulses generated by an Arbitrary Waveform Generator (AWG 33600A by Agilent) and both the Local Oscillator (LO) and the Feedback Local Oscillator (FB LO) to have a stable phase relation. The AWG used for the PnA measurement is a dual-channel device, and the separate channels can be used for the first and second PnA excitation pulses. The excitation pulses

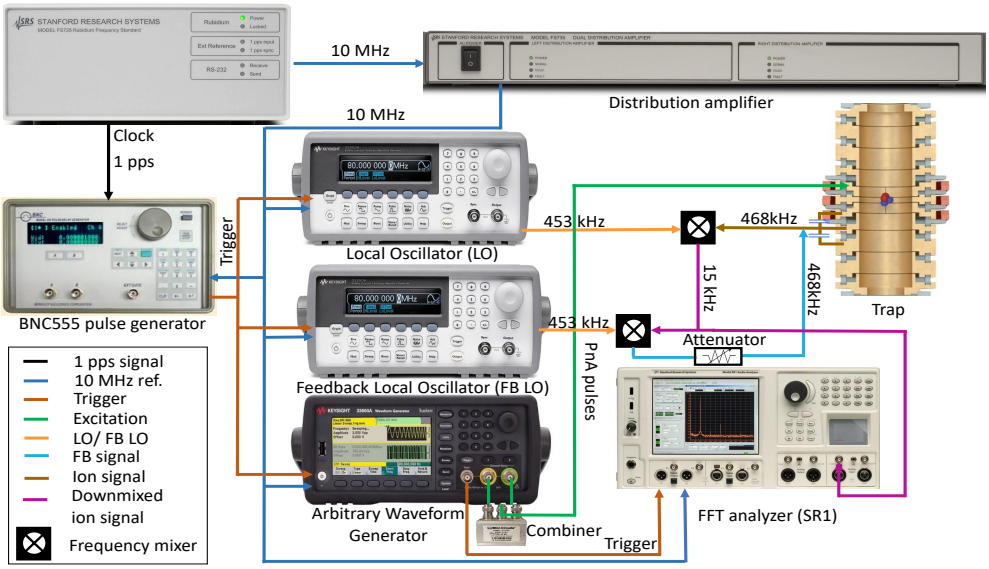

Figure 4.9. A sketch of the setup used in this work to perform PnA measurements. All devices are locked to a rubidium frequency standard clock. The cycles are synchronized to the 1 pps pulse of the atomic clock and triggered by the BNC. All frequencies are referenced to the 10 MHz output distributed by a dual distribution amplifier. The ion signal is down-mixed and read out by an FFT analyzer with the help of a local oscillator. The SR1 is triggered by the AWG, which delivers the excitation pulses. The feedback signal back to the trap is also shown. The different amplification stages are not depicted in the diagram.

and the relevant timings are programmed into the AWG at the beginning of the cycle. The advantage of the dual channel AWG is that once the timing of the pulses is programmed, only one trigger is required for both channels and thus, the relative jitter between the two channels is strongly reduced. The Fourier analyzer (SR1 audio analyzer by Stanford Research Systems) is connected to the sync channel of the AWG and is triggered by the same. A common reference clock is vital for phase-sensitive measurements to avoid any difference in timing between the excitation pulses, function generators, and signal readout. Any slight difference in time would affect the phase stability and cause an extra jitter. The timing system used during the mass measurement campaign is outlined in Fig. 4.9. The sketch also depicts how the signal from the trap $\sim$468 kHz is down-mixed with a sinus signal from the local oscillator, allowing the use of a Fourier analyzer in the audio range (0-28 kHz) to read out the signal. A frequency up-mixing is done to the feedback signal to the trap.

4.5 Stabilization system

Environmental parameters like temperature and pressure affect the temporal stability of the electric and magnetic fields. The fluctuations in the fields influence the high-precision measurements of the eigenfrequencies. During the past years, several stabilization systems have been developed and used to keep down the environmental influences at the experiment. Most of the developments occurred between the proton and deuteron mass campaigns. The temporal stability of the fields during the deuteron campaign was improved and resulted in a

mass measurement with higher precision than the previous mass measurements at the experiment. In the following sections, a brief discussion about these stabilization systems can be found.

4.5.1 Pressure stabilization

Temporal fluctuations of the magnetic field strength limit the precision of the cyclotron frequency measurements. Pressure in the four cryogenic reservoirs[9] of the experiment influence the magnetic stability. The boiling temperature of the cryogenic liquids is dependent on pressure. So if the pressure changes, the temperature of the experiment will change and, in turn, change the magnetic susceptibility of materials in the magnet's bore and also cause geometric changes in the coil. The pressure fluctuations can impact the boil-off rate of the cryogenic liquids. The experimental apparatus is suspended on the liquid helium-filling tube. The fluctuations in boil-off rate cause the tube to expand or contract and thus shift the position of the setup within the magnet.

The pressure changes can occur due to the filling of the cryogenic liquids, evaporation of the cryogenic gases in the reservoir, pressure fluctuations in the recovery line (or exhaust), changes in ambient pressure and temperature in the lab, and changes in the consumption of the cryogenic liquids[10]. Suppressing these changes would increase the magnetic field stability and help improve the statistical precision of the cyclotron frequency ratio. Therefore, a pressure stabilization system for the helium and nitrogen reservoirs of the magnet and the apparatus was developed and implemented as a part of the doctoral thesis of Sascha Rau. All the details of the design can be found in [30].

The pressure of the liquid helium reservoirs of the magnet and apparatus are combined for stabilization, and similarly also, both the nitrogen reservoirs. The setpoint of the pressure stabilization system is 1050 mbar, slightly above the typical pressure in the recovery line. During this work, a more sensitive and accurate pressure sensor by Paroscientific (6000-23A) with an accuracy of 80 µbar was used. This sensor has a resolution in the order of parts per billion. The pressure was stabilized around the setpoint within a few μbar. With the pressure stabilization installed, the magnetic field fluctuations could be reduced, resulting in a reduced modified cyclotron frequency jitter (see section 6.6.2) such that this does not limit the mass measurement.

4.5.2 Temperature stabilization

The temperature stability mainly influences the axial frequency determination due to the fluctuations of the trapping potential. These instabilities arise because the ambient temperature impacts the high-precision voltage source UM1-14. The manufacturer recommends that the voltage source should not be exposed to temperature variations. The temperature

[9] Liquid nitrogen and helium reservoirs for both magnet and apparatus (see section 4.1)

[10] The consumption rate of liquid helium tends to change on modifying the amplifier settings or applying RF pulses.

dependence for the voltage channels of UM1-14 connected to the PT given by its datasheet is $\pm 0.6\,\mathrm{ppmK}^{-1}$ [95]. In the past, cyclotron frequency changes also have been observed due to temperature. The most likely reason for this is the deformation or movement of either the magnet's coil or the trap inside the magnet.

To reduce the temperature changes, the experiment and especially the voltage sources are placed in a thermally insulated box with multiple openable sections to easily access the experiment. During the measurements, it is kept completely closed. The box is actively stabilized above room temperature to avoid the need for active cooling. The temperature stabilization system was installed before the mass measurements at LIONTRAP began [97]. The setpoint during the ^{4}He mass campaign was $30\,^\circ$C. The temperatures are measured through the resistance of PT-100 sensors (platinum resistance thermometer). The sensors are attached to the voltage source and different parts of the experiment, which are connected to a computer through a "REDLAB Temp" module (Meilhaus Electronic). The measured stabilized temperature over two days is plotted for different parts of the experiment in Fig. 4.10. The temperature regulation is performed by a PID (proportional integral derivative) controller, which measures and compares the temperature with a setpoint and determines a suitable output voltage depending on the required heating. The output controls a dimmer

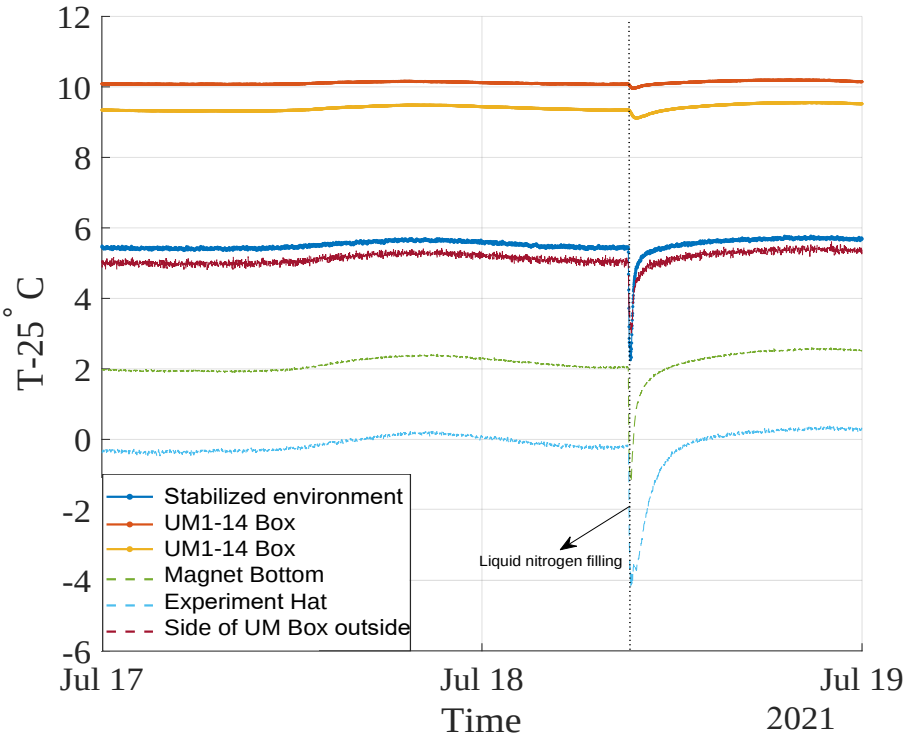

Figure 4.10. The stabilized temperatures for different parts of the experiment are plotted. The sudden dip in temperature is caused by the filling of liquid nitrogen. Here, the actual regulated temperature traces are not displayed but only the temperature after stabilization. The fluctuations are most likely caused by the imperfect insulation of the temperature-stabilized environment.

(SDK-AN-06), which controls the heater to achieve the required temperature. To minimize the temperature gradients, fans are attached inside the box to regulate the airflow that runs full time until interrupted.

The stabilization method has helped reduce the temporal voltage drifts and, consequently, temperature-induced frequency fluctuations. It also speeds up temperature settling after liquid helium or nitrogen filling.

4.6 Control system: software

The control of the complete experiment can be done from a PC. The legacy control software for the experiment was written in *Lab*VIEW. For this measurement campaign, it was decided to migrate this control software from *Lab*VIEW to MATLAB. Compared to *Lab*VIEW, MATLAB has an advantage because it is a script-based language. This property increases the readability of the code and gives the user more control over the implementation details according to their specific requirements, providing more flexibility. The remote control of the devices on hardware is realized through GPIB, USB, RS232, and network connections. At a software level, the control of the devices is implemented using object-oriented programming concepts using classes in MATLAB. The software is employed for live control of the devices, provides interfaces for data acquisition, and automation of the measuring routines. As MATLAB is also used as our analysis tool, the integration is easy, and the implementation of online analysis is straightforward. Another advantage of migrating the implementation was that a version control like Git could be applied. Doing this helped in keeping the history of the changes in the code. MATLAB also stores the command execution history and makes troubleshooting easier. The MATLAB control system of our current setup has been partially inherited from the one developed at ALPHATRAP [96].

4.7 In situ shim coil

As seen in section 2.2.2, the quadratic component of the magnetic field leads to an energy-dependent systematic shift of the eigenfrequencies. The contribution of the quadratic component of the magnetic field is $\frac{1}{2}B_2\hat{z}^2 = B_2\frac{k_BT_z}{m\omega_z^2}$. Therefore the combination of the finite axial temperature and the magnetostatic inhomogeneity has the dominant contribution to this systematic shift. Further temperature reduction is complicated, but the B_2 component can be nulled by installing a shim coil (B_2 compensation coil). Such a compensating coil was installed during the thesis work of Fabian Heisse; the details can be found in [90]. However, the coil was used at full capacity after technical corrections only from the deuteron measurement campaign on, and several design details can be found in [30].

The coil is made of niobium-titanium wire, wound on a copper cylinder, and placed directly around the trap chamber. The coil is wrapped with copper braids so as to dissipate incoming heat effectively. The wrapped coil around the trap chamber is shown in Fig. 4.1. The coil is closed with a superconducting joint, and once loaded and charged, the coil's

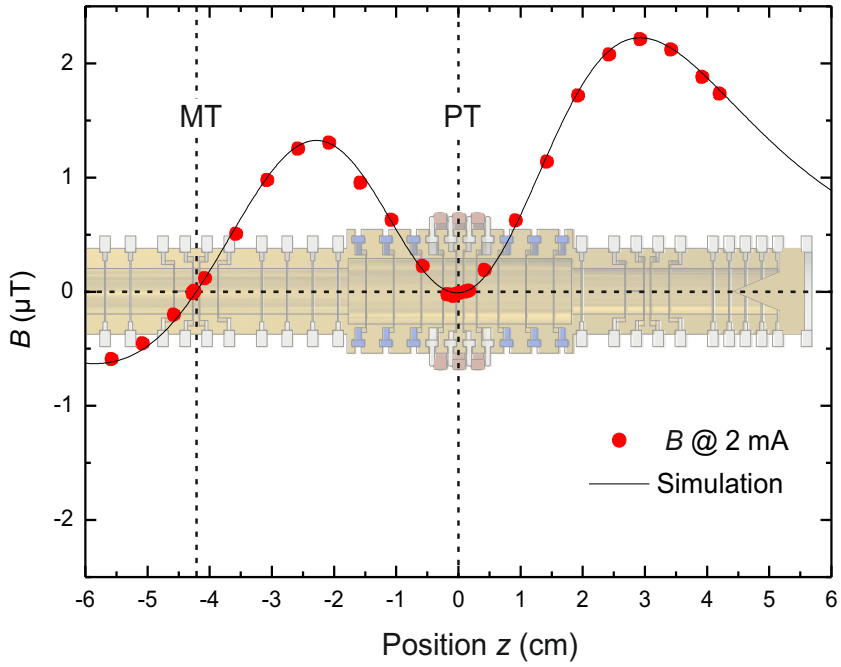

Figure 4.11. Magnetic field generated by the B_2 coil along the z-axis of the trap tower. The black line illustrates simulated data, and the red dots show the measured field in a test setup. The Figure is taken from [90].

magnetic field stays constant until quenched using a heating resistor. The magnetic field generated at the position of PT and MT is nominally zero, and no cyclotron frequency shift is expected if the coil is aligned correctly. The generated magnetic field in the trap is shown in Fig. 4.11, taken from [90]. The coil is designed such that B_2 generated is approximately $3.5\,\mathrm{nT\,mm^{-2}\,mA^{-1}}$ in the PT[11]. The real current used to charge the coil to compensate B_2 can be found in section 5.3. Similarly, a B_1 coil is also implemented to compensate for the residual linear magnetic field gradient. The B_1 generated is approximately $-50\,\mathrm{nT\,mm^{-1}\,mA^{-1}}$. The B_1 shim coil is not a closed-loop superconducting coil. It needs to be constantly supplied with power and has practical difficulties like instabilities of the current supply and increased liquid helium consumption due to heating. Hence the B_1 coil is not used actively during the measurement campaign.

4.8 Tilting mechanism

During the proton mass campaign [21] and the image charge shift measurement with protons [81], an angle between the magnetic field lines and the trap axis $\theta \approx 0.56(8)^\circ$ and ellipticity of the electrodes $\epsilon \leq 0.015$ was measured. The cause of the angle could be a misalignment between the magnetic field and the magnet bore or a tilt of the trap tower it-

[11] This was measured at room temperature outside the magnet using Hall probe and thus might have slight variation in the real setup

self inside the magnetic field. To align the trap by tilting the trap chamber, during the thesis work of Sascha Rau [30], a mechanical adjustment system was developed and installed.

The tilting process is accomplished with three adjustment screws that push on the trap chamber away from the cryogenic electronic section with the help of springs. These screws can be tightened or relaxed from outside. The adjustment screws are elongated using glass fiber rods towards the bottom of the magnet, where three mechanical feedthroughs from room temperature can be coupled to it. The room temperature mechanical feedthroughs can be decoupled from the adjustment screw once the tilting is done to reduce the heat load. The tilting mechanism helped to reduce the angle to $0.05(5)^\circ$ during the deuteron campaign. However, due to certain mechanical constraints, the angle was not reduced to this extent during this work (see section 5.5). The setup of the adjustment screws (tilting rods) on the trap chamber is shown in Fig. 4.1.

5. Trap preparation: steps and measurements

This chapter details the procedures and measurements to prepare for the mass determination of ^{4}He. Production of a single ion, electrostatic trapping field optimization, compensation and estimation of the magnetic field inhomogeneity, determination of the ion temperature, and finally, measurement of the image charge shift in our trap will be discussed.

5.1 Ion production

The first step towards a mass measurement is the creation of single ions of the required species. The ions are created inside the trap chamber using the miniature electron beam ion source (mEBIS). The detailed construction and operation are explained in section 4.2.5. In this section, the voltage configurations and parameters used for the production of ions for this measurement campaign are discussed.

5.1.1 Production scheme

The Field Emission Point (FEP) emits an electron beam current in the order of 100 nA along the magnetic field when there is a voltage difference of at least 700 V between the FEP and the acceleration electrode. The other potentials and energies used in the creation process differ with respect to the desired ion:

- Production of $^{12}C^{6+}$: The electron beam energy chosen for stripping the ^{12}C is about 1 keV, which is higher than the ionization energy required to produce $^{12}C^{6+}$, $E_{ion}^{^{12}C^{6+}}$ = 0.489 keV [98].
- Production of $^4He^{2+}$: Prior to ionizing the ^{4}He gaseous atoms, these are released from the surface of the gas source (refer to section 4.3). Therefore, before the electron beam is produced, the surface of the gas source is pre-heated by supplying a heating power of 200 mW for 45 sec. The surface is kept at a higher temperature to release helium atoms while the FEP is firing, and then the heating is turned off. The electron beam energy chosen for producing $^4He^{2+}$ is about 100 eV, which is higher than the ionization energy for the same, $E_{ion}^{^4He^{2+}}$ = 54.4 eV [98].

The reflector electrode reflects back the electron beam. On multiple reflections, the electron density increases and widens the beam. The reflector voltage is fixed hardware-wise to 1.15 times the FEP voltage. The widened electron beam hits the target, ablates atoms from the target surface, and ionizes them. The gaseous atoms that are released near the target are also ionized. The ion cloud is trapped in the CT, where further electron impact ionization and charge breeding occur. The ring electrode of the CT is then usually set to about ~ -150 V for

a few seconds, which helps to remove low-charged heavy ions due to the stability criterion for the trap described by Eq. (2.13). The ion cloud stored in the CT after production consists of many different species in different charge states, and to prepare a single ion, the ion cloud is adiabatically transported to the PT.

5.1.2 Preparation of a single ion

The constituents in the ion cloud can be detected by recording a mass spectrum (Fig. 5.1). This detection is achieved by ramping the ring voltage of PT over a range of voltage (-14 V to -2 V) and concurrently monitoring the ion signals around the center of the resonator. Due to the ramping of the ring voltage, ions with different q/m ratios are successively tuned with the resonator. To improve the visibility, the axial energy of the ions is increased right before they get into resonance with the tank circuit by applying an excitation signal slightly above

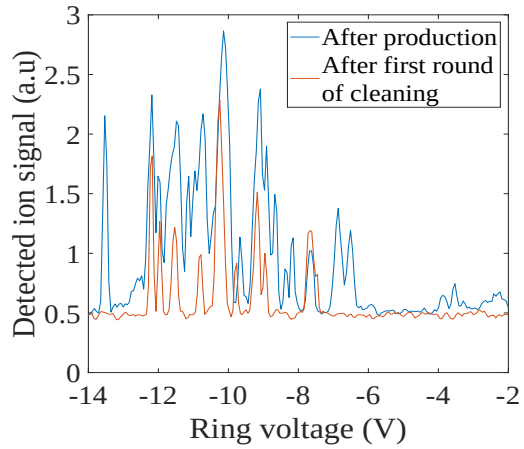

(a) After the production of $^{12}C^{6+}$

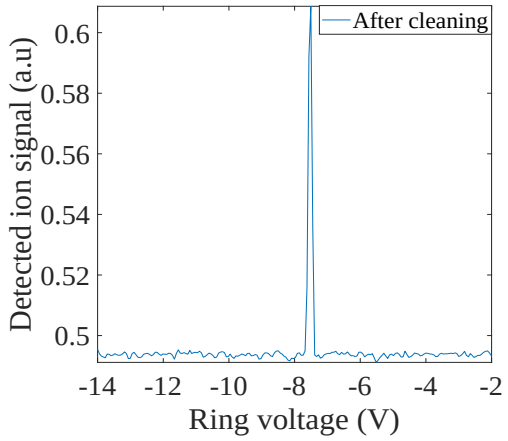

(b) Cleaned to single out $^{12}C^{6+}$

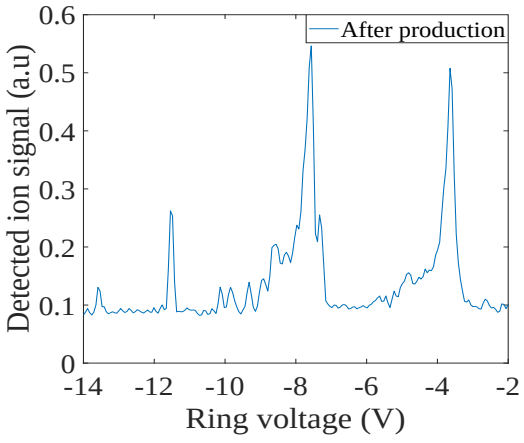

(c) After the production of $^{4}He^{2+}$

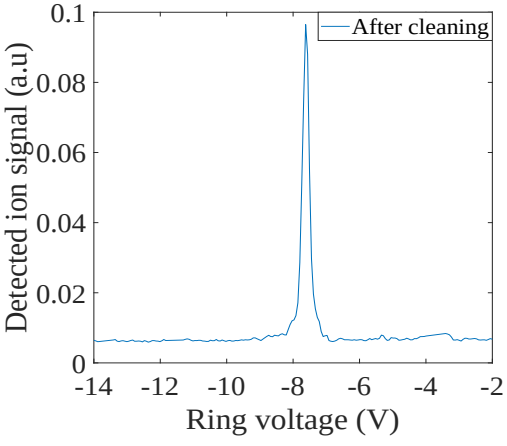

(d) Cleaned to single out $^{4}He^{2+}$

Figure 5.1. An example of mass spectra recorded during the ion production. Plots (a) and (c) show the respective mass spectra of carbon and helium ions after the production run. These are typically large ion clouds. In (b) and (d), peaks of the ions of interest are visible after cleaning the trap. The ions are excited with an off-resonant axial excitation to amplify the visibility.

the resonance frequency of the axial resonator. The disadvantages of such mass spectra are that they have insufficient resolution to resolve different ion species with similar q/m and do not cover all the q/m ratios possible in the ion cloud due to the restricted ring voltages accessible. The methods to deal with these cases are discussed below.

Various techniques are available to isolate a single ion of interest from the cloud [19, 63]. In this work, we used the axial cleaning technique with a strong broadband axial excitation. The cleaning technique is performed in mainly three steps as follows:

1. The axial mode of the ion of interest is cooled by tuning the axial frequency of the ion to the resonator by adjusting the trapping voltage.
2. Broadband axial dipolar frequency sweeps (using D_z line) are performed above and below the axial frequency. It has to be made sure that the excitation frequency ranges do not include the eigenfrequencies of the ion of interest. Thus, the lower limit of the frequency span below the axial frequency is set by the magnetron frequency (ν_-), and the upper limit above resonance is set to two times the axial frequency ($2\nu_z$). The modified cyclotron frequency (ν_+) is much larger and remains unaffected. Now, all the ions except the one of interest have significant axial energy.
3. The next step is to immediately make the trap potential very shallow, even up to $U_r \approx 100\,\mathrm{mV}$, for a few seconds so that the excited ions escape.

This technique is repeated several times until only ions cooled by the resonator remain. However, this means unwanted ions with a similar q/m ratio as the ion of interest could also be cooled and thus not removed in the process. Although the axial frequencies and magnetron frequencies of the ions with similar q/m ratios are close by, but their modified cyclotron frequencies are far apart ($\sim$ kHz) enough to distinguish between different species. To this end, one has to have a good idea of what ion species are produced or are present in the ion cloud to address their modified cyclotron frequency. Here again, an excitation signal at the selected frequency is supplied by which the ions with the addressed frequency are excited. Axial cleaning sweeps are then employed to remove the excited ions with shifted axial frequency from the trap. This technique is only performed if an unwanted ion species that cannot be separated from the ion of interest is present because the modified cyclotron frequencies vary over a wide range for different ion species and would take a long time to sweep over such large frequency ranges.

Once all the other ion species are removed to single out an ion of interest, firstly, the width of the axial dip is observed to estimate the number of ions of the species that are present; see Eq. (3.26). The typical dip-widths for single $^4He^{2+}$ and $^{12}C^{6+}$ ions are $\sim 0.5\,\mathrm{Hz}$ and $\sim 1\,\mathrm{Hz}$, respectively, in our setup during this work. The next step is to excite the axial mode of the ions. These excited ions are then seen as peak signals on the resonator at individually shifted frequencies, depending on the specific amplitude in the anharmonic potential of the trap. As soon as one peak moves onto the center of the resonator and cools, the trap potential is made shallow stepwise so that the particles that are still hot can escape. Until the ion is singled

out, this is repeated multiple times with intermediate cooling of all three eigenmotions of the remaining ions so as not to lose all of them simultaneously.

Once only a single ion is left, this is then carefully transported to ST-I, and the production process is repeated to create the second ion of interest.

5.2 Electrostatic field optimization

In section 2.2.1 energy dependent eigenfrequency shifts due to imperfections of the electrostatic potential were explained. In this section, the optimization of the Precision Trap (PT) to minimize these shifts will be discussed.

In section 2.2.1.1, it was already discussed that the PT is designed to attain a highly harmonic electrical trapping potential ($C_4 = C_6 = C_8 = C_{10} = 0$) with the application of suitable voltages. However, geometric imperfections and undesired islands of potential lead to deviations from the perfectly compensated trap and make online tuning necessary. As the PT is doubly compensated and has two pairs of independent correction voltages, it achieves a combined orthogonality criterion: $C_2 = D_{2,1}\frac{U_{C1}}{U_r} + D_{2,2}\frac{U_{C2}}{U_r} + E_2$, where $D_2^{comb} = D_{2,1}\frac{U_{C1}^{\text{nom}}}{U_r} + D_{2,2}\frac{U_{C2}^{\text{nom}}}{U_r} = 0$, at nominal voltages (see section 2.2.1.1). Therefore, adjusting the voltage applied on the first set of correction electrodes ($\frac{U_{C1}}{U_r} = \text{TR}_1$) makes it necessary to also adjust the voltage applied on the second set of correction electrodes ($\frac{U_{C2}}{U_r} = \text{TR}_2$) by the same factor to keep the axial frequency constant. To adjust both correction voltages at the same time, we use a combined tuning ratio TR, which makes

$$\begin{aligned} \text{TR}_1 &= \text{TR} \cdot \text{TR}_{1,\text{start}}, \\ \text{TR}_2 &= \text{TR} \cdot \text{TR}_{2,\text{start}}. \end{aligned} \tag{5.1}$$

The steps involved in the online optimization process are the following:

1. To study the anharmonicity, the shifts in axial frequency as a function of different magnetron excitation strengths (expressed as the numbers of excitation cycles, #cycle $\propto r_-$) are measured for different tuning ratios by recording the axial frequency before (cold dip) and after the excitation (hot dip), see Fig. 5.2a.
2. These shifts can be modeled with a two or more parameter polynomial fit of even order where the polynomial's coefficients are related to the anharmonicity coefficients,

$$\Delta\nu_z = \sum_{n=1}^{max\ order} P_n(\#\,\text{cycle})^{2n}. \tag{5.2}$$

#cycle = $\nu_- t_{\text{exc}}$, where t_{exc} is the length of the RF excitation pulse at a fixed amplitude (U_{exc}). $\Delta\nu_z$ from C_4, C_3 and C_6 is know from Eq. (2.25), Eq. (2.26) and Eq. (2.32) as

$$\Delta\nu_z \approx -\frac{3\nu_z}{2d_{\text{char}}^2}\frac{C_4}{C_2}r_-^2 + \frac{9\nu_z}{8d_{\text{char}}^2}\frac{C_3^2}{C_2^2}r_-^2 + \frac{45\nu_z}{16d_{\text{char}}^4}\frac{C_6}{C_2}r_-^4, \tag{5.3}$$

Here, the excited magnetron radii and the strength of the magnetron excitations are related by a calibration constant κ_- as:

$$r_- = \kappa_- \#\,\text{cycle}. \tag{5.4}$$

One must note that C_4 and C_3^2 scale with r_-^2 in the same manner, so by zeroing the coefficients associated with r_-^2, either the combination of C_4 and C_3 are nulled, or both are nulled (see section 2.2.1.2). For simplicity, the optimization process and residual anharmonicity estimation will be described in terms of an effective C_4 rather than addressing the odd and even order coefficients separately. Therefore,

$$\Delta\nu_z \approx P_1(\#\,\text{cycle})^2 + P_2(\#\,\text{cycle})^4. \tag{5.5}$$

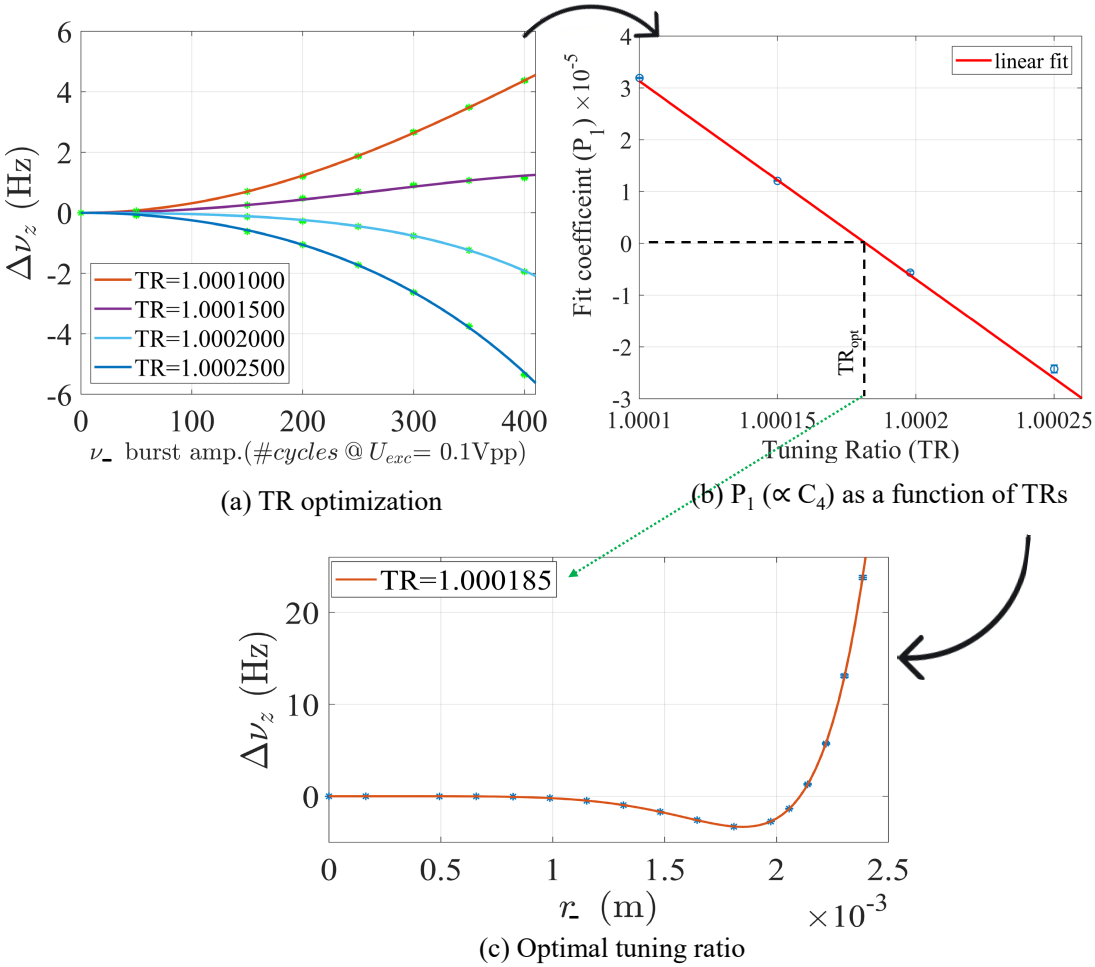

(a) TR optimization

(b) P_1 ($\propto C_4$) as a function of TRs

(c) Optimal tuning ratio

Figure 5.2. An example of electric field optimization in the PT. In (a), the axial frequency shifts vs. magnetron excitation strength for different TR settings are measured. Each measurement is fitted with a polynomial with coefficients proportional to C_4 and C_6. In (b), the coefficients of the quadratic term are used to extract the optimal TR. Finally, in (c) the axial frequency shift as a function of magnetron excitation for optimal TR is measured. The black arrows indicate the order of the process.

3. The fitted parameter of the quadratic term P_1 for different tuning ratios is plotted (see Fig. 5.2b). The linear nature of the plot arises from the fact that the anharmonicity coefficients C_i are bilinear to the individual tuning ratios (TR_1 and TR_2) and linear to the combined tuning ratio (TR)

$$C_i = D_{i,1}\frac{U_{C1}}{U_r} + D_{i,2}\frac{U_{C2}}{U_r} + E_i. \tag{5.6}$$

This implies that at $P_1 = 0$ the C_4 coefficient is nulled. A linear fit of $P_1(\mathrm{TR})$ is done to extract $\mathrm{TR}(P_1 = 0)$ as the optimal tuning ratio (TR_{opt}). This method is repeated with higher order coefficients of the fitted polynomial corresponding to higher order anharmonicities. In the example in Fig. 5.2a, at optimal tuning ratio, the uncertainty in the leading order anharmonicity $\delta C_4 \approx 3.3 \times 10^{-6}$ and $C_6 \approx 9(5) \times 10^{-5}$.
The slope of the line m_{P_1} along with $D_4 = -0.79$ [19] and measured $C_2 = -0.6006$ are used to find the calibration constant as

$$\kappa_- = \sqrt{-\frac{2m_{P_1}C_2 d_{\mathrm{char}}^2}{3\nu_z D_4}}. \tag{5.7}$$

The coefficients $D_{i,j}$ are determined from numerical simulation[1]. The value of the combined D_4 coefficient ($C_4 = \mathrm{TR}\cdot D_4 + E_4$) is also confirmed by experimental results [19].
4. In case the anharmonicity coefficients are large $TR_{1,start}$ or $TR_{2,start}$ can be changed, and the above-described optimization process is repeated.
5. Once TR_{opt} is obtained, the axial frequency shift is studied for a more extensive range of magnetron excitation radii at this setting, see Fig. 5.2c. The optimal TR in the example measurement shown in Fig. 5.2c is $TR_{opt} = 1.000185$ and $\kappa_- = 6.16\ \frac{\mu m}{\#cycle}$ at $0.1\ V_{pp}$.

The tuning of the electrostatic potential needs to be repeated after every production cycle due to the modification or formation of patch potentials on the surfaces of the electrodes resulting from surface imperfection or frozen rest gas that gets charged up by the ions or electron beam during production (see section 2.2). These altered patches of potential tend to change the position of the ion. The magnitude of the effective patch potentials can be estimated by comparing the axial frequencies ($\nu_{z,1}$ and $\nu_{z,2}$) of the ion at two different ring voltage settings ($U_{r,1}$ and $U_{r,2}$) as:

$$U_{\mathrm{patch}} = \frac{U_{r,2}\left(\frac{\nu_{z,1}}{\nu_{z,2}}\right)^2 - U_{r,1}}{1 - \left(\frac{\nu_{z,1}}{\nu_{z,2}}\right)^2}. \tag{5.8}$$

[1] The uncertainties of the coefficients are ignored for now

The different axial frequency settings are achieved by changing the voltage on the varactor diode to shift the resonance frequency of the tank circuit. Then the ring voltage is adjusted to bring the ion's axial frequency back into resonance with the resonator. In our trap, the patch potentials are in the order of a few tens of mV. With every production, the effective electric potential changes due to the change of patch potentials on the electrode surfaces. Thus, the TR is adjusted after every new ion creation.

5.2.1 Estimating residual electrostatic anharmonicity

After optimization and measuring the axial frequency shift as a function of the magnetron radius at optimal TR_{opt}, the residual anharmonicity coefficients are determined by fitting polynomials of different orders (Eq. (5.2)) for different ranges of the magnetron radii. The exact radius at which the ions become sensitive to C_4, C_6, or higher coefficients is undefined, and for the same reason choosing the order of the polynomial that should be used to extract the anharmonicity coefficients is not straightforward. Thus, even-order polynomials with different degrees from r_-^4 to r_-^{12} are chosen. Each of these polynomials was then used to describe the frequency shift data for various ranges of magnetron radii. The fit-range varied from the minimum number of data points required to fit the model to the largest excited magnetron radius. The reduced χ^2 varied to a large extent for different combinations of polynomials and the fit-ranges. In Fig. 5.3, the C_4 and C_6 values for different fit models with reduced χ^2 around 1 are presented for the measurement shown in Fig. 5.2c. The values of the anharmonicity coefficients depend on the fit-range. However, for all good fits, which produce a reduced χ^2 close to 1, the values fall in a limited range giving the uncertainty of the C_4 and C_6 coefficients. In this particular example (Fig. 5.3), C_4 values are in the range $\pm 6 \times 10^{-6}$, and C_6 values are between 1×10^{-4} and -4×10^{-4}.

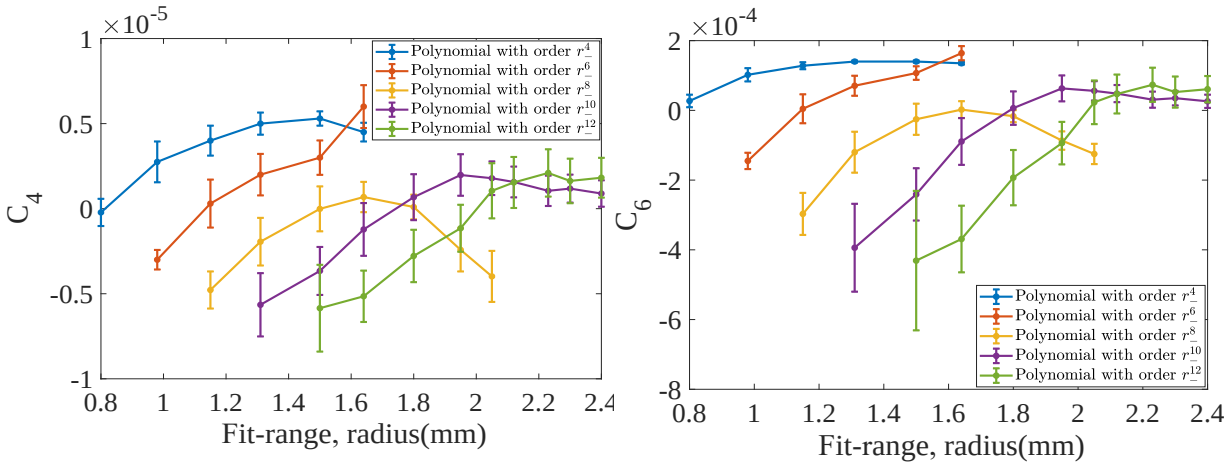

(a) Estimating the value of C_4

(b) Estimating the value of C_6

Figure 5.3. An example of electrostatic anharmonicity estimation. In (a) and (b), the values of C_4 and C_6 are plotted for different combinations of polynomial fit orders and fit ranges of the data in Fig. 5.2c with reduced χ^2 close to 1.

Multiple TR measurements were performed during the measurement campaign. An average of the anharmonicity coefficients obtained from fits with reasonable χ^2 over different measurements results in:

$$\begin{aligned} C_4 &= 0(1) \times 10^{-5}, \\ C_6 &= -4(15) \times 10^{-5}. \end{aligned} \tag{5.9}$$

The uncertainty of these coefficients is small enough not to cause significant systematic shifts in the cyclotron frequency ratio measurements, which will be discussed in section 6.4.2.

In the optimization process that we have discussed so far, tuning $C_4 \approx 0$ implies that the combination of C_4 and C_3 has been nulled or zero frequency shift is achieved when $C_4 = \frac{3C_3^2}{4C_2}$ (see section 2.2.1.2 and section 5.2). The voltages we use in our trap throughout the measurement campaign are applied symmetrically; thus, the contribution from C_3 can be assumed to be small. The natural size of C_3 in our trap is $\sim 10^{-3}$, as our electrode lengths are known to $\pm 10\,\mu$m, and $d_{\text{char}} = 5.107$ mm. This translates into a C_4 in the range of 10^{-6} to 10^{-5} after the optimization.

The magnetic field inhomogeneity (B_2) can also cause frequency shifts, but as the optimization measurements are done with magnetron mode excitations, the influence of the small magnetic inhomogeneities due to reasonably small values of B_2, such as in our PT, can be neglected.

5.3 Magnetic field optimization

As detailed in section 2.2.2, the quadratic component of the magnetic field B_2 causes the leading order frequency shifts. As the first step, one needs to activate the closed loop superconducting shim coil to compensate for this magnetic field inhomogeneity (see section 4.7). To get a preliminary measure of B_2, the axial frequency shift is observed after a modified cyclotron mode excitation. Initially, we excited the ion to a reasonable radius (around $400\,\mu$m[2]) to observe a frequency shift of -3 Hz, and then this shift was compensated by charging the shim coil with a suitable current, in this case 25.22 mA. The null or minimal axial frequency shift indicates that B_2 is compensated and minimized.

To estimate the residual magnetostatic inhomogeneity, which adds to the systematics of the mass measurement, a calibration for the modified cyclotron radius r_+ should be made.

5.3.1 Cyclotron radius calibration

The modified cyclotron radius is calibrated to know the absolute cyclotron energy associated with a particular pulse strength (excitation strength); see section 3.2.1. The excitation strength $S^+_{t,U} = U \cdot t$, where U and t are the amplitude and duration of the excitation pulse, respectively, is related to the excited modified cyclotron radius, for an initially cold particle

[2]Estimated using the calibration from the previous measurement campaign [30]

as $r_+ = \kappa_+ U t = \kappa_+ S^+_{t,U}$, where κ_+ is a calibration constant. To acquire information about κ_+, the straightforward procedure is to measure the modified cyclotron frequency shifts as a function of $S^+_{t,U}$. At an excited r_+, the modified cyclotron frequency shift, assuming $\omega_+ \gg \omega_-$, can be noted as follows (see Eq. (2.27), Eq. (2.46) and Eq. (3.49))

$$\frac{\Delta\omega_+}{\omega_+} = \left(\frac{C_4}{C_2} \frac{3}{2d^2_{\text{char}}} \frac{\omega_-}{\omega_+ - \omega_-} - \frac{B_2}{2B_0} \frac{\omega_+ + \omega_-}{\omega_+ - \omega_-} - \frac{\omega_+^2}{2c^2} \right) r_+^2. \tag{5.10}$$

In a trap with an optimized electric field ($|C_4| < 1 \times 10^{-5}$) and minimized B_2, the relativistic mass increase is the dominant contribution to $\Delta\omega_+$ leading to

$$\frac{\Delta\omega_+}{\omega_+} = -\left(\frac{\omega_+^2}{2c^2}\right) r_+^2 \Rightarrow \frac{\Delta\omega_+}{\omega_+} = \frac{\Delta\nu_+}{\nu_+} = -\left(\frac{\omega_+^2}{2c^2}\right) (\kappa_+ S^+_{t,U})^2. \tag{5.11}$$

To study the frequency shifts, the PnA method discussed in section 3.3 is used to measure the phase evolution for different excitation strengths. From the phase information, the modified cyclotron frequency can be determined. The frequencies were repeatedly measured for four different excitation strengths in a randomly chosen order. The result of such a measurement is shown in Fig. 5.4, where the linear dependency of the frequency shift to the square of the cyclotron radius or $(S^+_{t,U})^2$ is explicit. A fit to the measured data can be used to extract the calibration constant κ_+. From Eq. (5.11)

$$\kappa_+ = \sqrt{\frac{2c^2}{\omega_+^2} \frac{1}{\nu_+} \frac{\Delta\nu_+}{{S^+_{t,U}}^2}}, \tag{5.12}$$

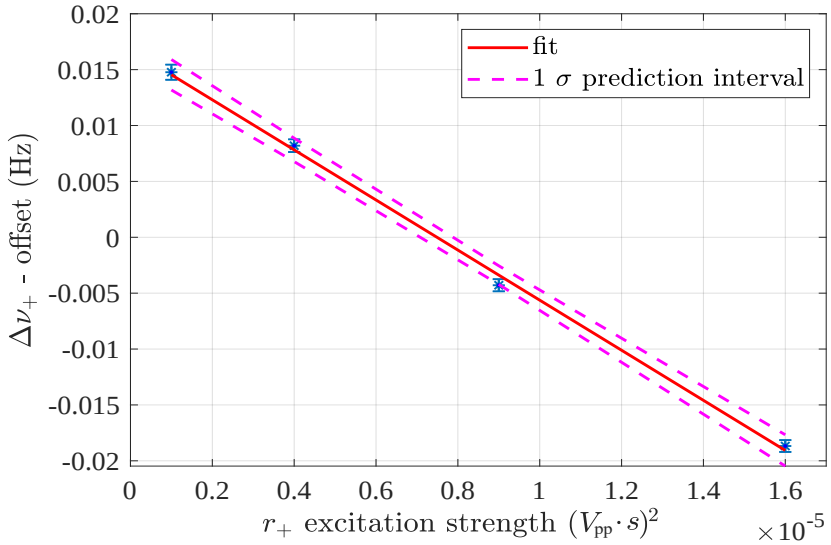

Figure 5.4. Calibration of modified cyclotron radius. The shift in modified cyclotron frequency as a function of cyclotron radius (expressed as excitation strengths). The fitted slope of this line enables the estimation of κ_+. The dotted line (magenta) shows the 1σ prediction interval derived from the data set.

where $\frac{\Delta\nu_+}{{S^+_{t,U}}^2}$ is the fitted slope (see Fig. 5.4). Multiple κ_+ measurements were performed during the mass measurement campaign and were found to be consistent. The value determined for $\kappa_+ = 0.020\,49(43)\,\mathrm{m\,{V_{pp}}^{-1}\,s^{-1}}$.

5.3.2 Estimating residual magnetostatic inhomogeneity

To study the inhomogeneity in the magnetic field, axial frequency shifts as a function of modified cyclotron mode radius r_+ are determined. Initially, the axial frequency of the cold ion is measured. In the next step, an excitation pulse is triggered to excite the modified cyclotron mode, and the shifted axial frequency of the excited ion is measured. This is repeated for different radii from about 10 µm to close to 1 mm. The excitation strengths are calibrated using the κ_+ discussed in section 5.3.1. Results of such measurements are shown

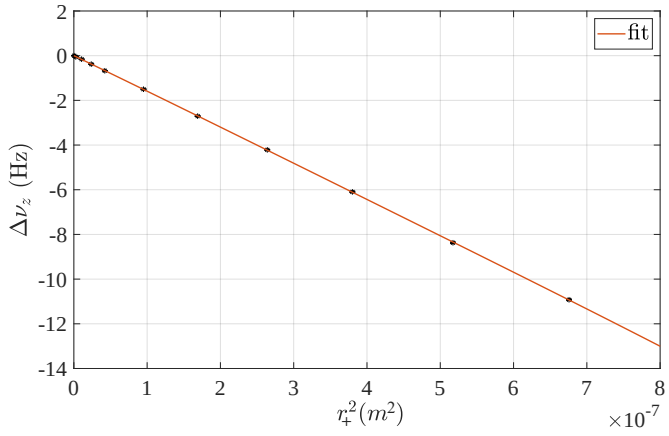

(a) Uncompensated B_2 measurement

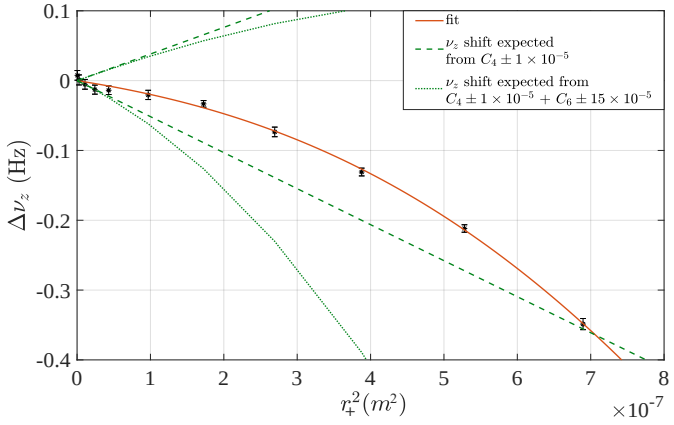

(b) Compensated B_2 measurement

Figure 5.5. Estimation of the magnetic inhomogeneity due to the quadratic component B_2. The axial frequency shift is measured as a function of the modified cyclotron radius. In (a), this effect is measured without compensation from the shim coil. In (b), the residual inhomogeneity is measured after charging the B_2 shim coil, thus compensating B_2. This is the usual setting during the mass measurement. The green lines demonstrate how the residual electrostatic anharmonicity limits the determination of B_2 and further optimization of the magnetic field.

in Fig. 5.5, here Fig. 5.5a was performed without charging the in situ shim coil and Fig. 5.5b was measured after minimizing B_2 by charging the compensation coil.

At an excited r_+, the axial frequency shift can be noted as follows (see Eq. (2.25), Eq. (2.32), Eq. (2.45), and Eq. (3.50))

$$\frac{\Delta\nu_z}{\nu_z} = \left(-\frac{C_4}{C_2}\frac{3}{2d_{\text{char}}^2} + \frac{B_2}{4B_0}\frac{\nu_+ + \nu_-}{\nu_-} - \frac{\omega_+^2}{4c^2} + \frac{9}{8}\frac{C_3^2}{C_2^2 d_{\text{char}}^2}\right) r_+^2 \tag{5.13}$$

The axial frequency shift due to relativistic mass increase (the second last term in Eq (5.13)) is minor. The shift is $\leq$10 mHz for $r_+ \leq 500\,\mu$m. Assuming a perfectly tuned electric field (combined effect of C_4 and C_3 is 0) in our precision trap, the significant contribution to the axial frequency shift would be from the term associated with B_2. Therefore, the linear term of a polynomial fit to the axial frequency shift as a function r_+^2 (Fig. 5.5) can be used to determine the value for B_2. When B_2 is compensated and close to zero, the axial frequency shift as a function of r_+ depends strongly on the electrostatic anharmonicities. This is evident from Fig. 5.5b, where the green lines indicate the axial frequency shift due to C_4 and a combination of C_4 and C_6. Thus the limit to which we can tune out B_2 or give a limit to the magnetostatic inhomogeneity depends on the uncertainty in the electrostatic anharmonicity. Here, terms that scale quadratically in r_+ are relevant. These are dominantly the C_4 and C_3^2 terms. Since the effective contribution of these has been previously nulled in the electrostatic field optimization using r_- excitations, here, the individual terms do not contribute separately (refer to Eq. (5.13) and section 2.2.1).

Measurements to extract the value of B_2 were repeated throughout the mass measurement campaign and were found to be consistent. The uncompensated B_2 in our PT was measured to be $B_{2,uncomp} \approx -0.078(13)\,\text{T}\,\text{m}^{-2}$, and after compensation by charging the in situ shim coil, the residual $B_2 = -0.0004(20)\,\text{T}\,\text{m}^{-2}$.

The same principle can be applied to extract the value of B_2 by comparing axial frequency shifts caused by excitations of the magnetron mode and modified cyclotron mode because the cyclotron mode is particularly sensitive to magnetic inhomogeneities and the negligible relativistic mass increase. Therefore, the comparison can give limits to magnetic inhomogeneities. The previously discussed method uses the same principle. The only difference is that in the firstly discussed measurement, the electric field optimization is done first, and the optimal tuning ratio is found at which the estimation of residual magnetic inhomogeneity is performed. In this case, magnetron and cyclotron excitations are performed for three different tuning ratios (TRs) for a set of radii, and the axial frequency shifts are recorded. See Fig. 5.6. These shifts are fitted with $f(r_\pm) = \Delta\nu_z(r_\pm) = P_1 r_\pm^2 + P_2 r_\pm^4$. The $P_1^{\nu_-}$ coefficients are plotted for different TR for both magnetron and modified cyclotron mode. In the magnetron mode excitations, TR_{opt} at which $P_1^{\nu_-} = 0$ is where the combination of C_4 and C_3^2 is nulled. A detailed explanation of this will be found in section 5.2.
the standard B_2 measurement discussed previously.

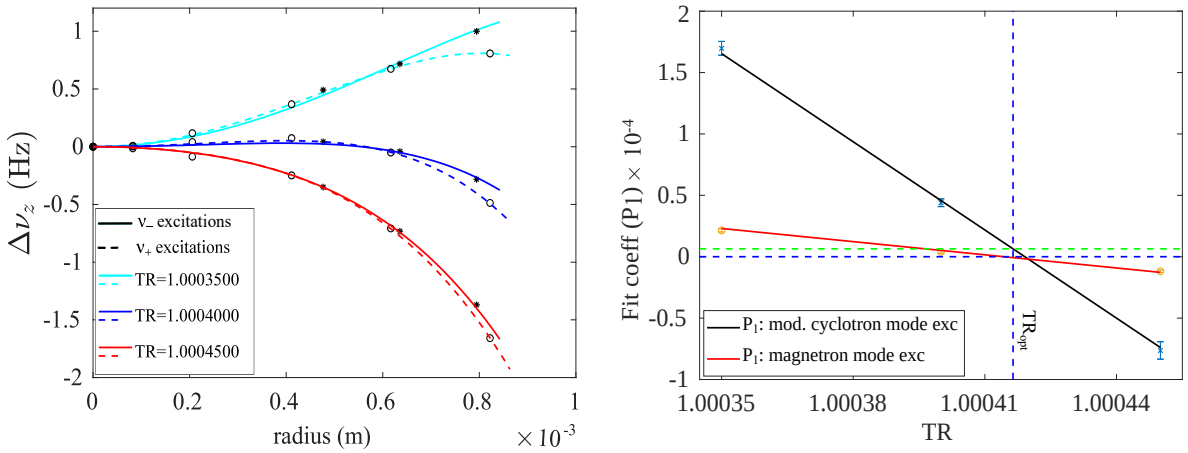

(a) Axial frequency shift for ν_+ and ν_- excitations

(b) Fit Coefficient P_1 vs TR

Figure 5.6. Extraction of B_2 from the comparison of axial frequency shifts measured for different magnetron radii and axial frequency shifts measured for different modified cyclotron radii. In (a), the solid lines correspond to ν_- excitations, and thus the x-axis denotes r_- and the dotted lines correspond to ν_+ excitations, and thus the x-axis denote r_+. These are plotted for different settings of TR. In (b), the fit coefficients $P_1^{\nu_-}$ (red) and $P_1^{\nu_+}$ (black) (from (a)) for different TRs are plotted. The blue dotted lines mark the TR_{opt} at $P_1^{\nu_-} = 0$. The green dotted line marks the $P_1^{\nu_+}$ for this TR_{opt}.

Rearranging Eq. (5.13)

$$B_2 = \frac{\Delta\nu_z}{r_+^2}\frac{4B_0\nu_-}{\nu_+\nu_z} + \frac{C_4}{C_2}\frac{3}{2d_{\text{char}}^2}\frac{4B_0\nu_-}{\nu_+} - \frac{9}{8}\frac{C_3^2}{C_2^2 d_{\text{char}}^2}\frac{4B_0\nu_-}{\nu_+}, \tag{5.14}$$

where $\frac{\Delta\nu_z}{r_+^2} \propto P_1^{\nu_+}$. Therefore, when the combination of C_4 and C_3^2 terms is zero, the $P_1^{\nu_+}(\text{TR}_{\text{opt}})$ can be used to extract the residual B_2. The $P_1^{\nu_+}$ corresponding to the optimal TR obtained from magnetron mode excitations will not be zero but slightly shifted due to the different slopes in the different cases, as seen in Fig. 5.6b. Therefore, once the electrostatic field is optimized, we can obtain B_2 as

$$B_2 = 4B_0 P_1^{\nu_+}\frac{\nu_-}{\nu_+\nu_z}. \tag{5.15}$$

The B_2 value obtained from this comparison agrees within 1σ with the value extracted from the standard B_2 determination previously discussed.

Although we have a shim coil to compensate for the residual linear magnetic field gradient B_1 of the magnet field, this was not used during the mass measurements because it cannot be operated in persistent mode due to technical reasons (see section 4.7). The magnetostatic inhomogeneity B_1 can be mapped by measuring the cyclotron frequency of the ion at different positions along the z-axis. The position of the ion can be shifted by supplying asymmetric voltages on the correction electrodes. The ion's equilibrium positions at the offset voltages can be calculated by simulating the cylindrical trap potential. The

free cyclotron frequency of the ion at the different positions was determined using the PnA method, where the cyclotron radius was excited to only about 20 µm. See Fig. 5.7, the frequencies were measured at three different axial positions and the value of B_1 can be determined from the fitted slope because $\frac{\Delta B}{B} \simeq \frac{B_1}{B_0}\Delta z \simeq \frac{\Delta\omega_c}{\omega_c}$ (section 2.2.2). From this measurement, the linear inhomogeneity $B_1 = 0.002\,13(11)\,\mathrm{T\,m^{-1}}$ was determined while the B_2 shim coil was still charged. The estimation indicated that the magnetic field increases towards the creation trap. The measurement was repeated after discharging the shim coil and then $B_1 = 0.002\,24(16)\,\mathrm{T\,m^{-1}}$.

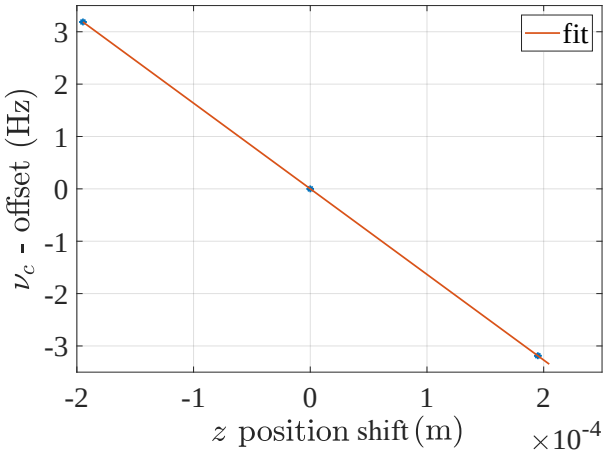

Figure 5.7. Measurement of linear magnetic field gradient B_1. The cyclotron radius is measured at shifted ion positions along the axial direction as a result of different offset voltages.

The B_1 together with the electrostatic anharmonicity C_3 can cause axial frequency shifts, as discussed in section 2.2.3. Like the residual electrostatic anharmonicities limit how precisely we can obtain the value for B_2, this combination of $B_1 \cdot C_3$ could mimic a B_2 in these measurements. For example, with a $C_3 \sim 10^{-3}$ and $B_1 \sim 2 \times 10^{-3}\,\mathrm{T\,m^{-1}}$, we will have a $B_2^{\mathrm{eff}} \sim 10^{-3}\,\mathrm{T\,m^{-2}}$. To set a better limit from the combination $B_1 \cdot C_3$, a better estimate or measurement of C_3 has to be performed, or B_1 has to be compensated.

5.4 Temperature measurement of an ion

The ion's modified finite cyclotron mode temperature (T_+) relates to relativistic frequency shifts, a significant systematic effect, especially for light ions. The temperature measurement involves studying the axial frequency jitter caused by the Boltzmann-distributed modified cyclotron energy (see section 3.4). The axial frequency of an ion thermalized in all modes is recorded initially. The shifted frequency is measured following a dipolar excitation of the modified cyclotron mode to better resolve the axial frequency jitter. As discussed in section 5.3.2, when the ion is excited in the modified cyclotron mode, the axial frequency shifts are mainly induced by C_4 and B_2 and the relativistic shifts are negligible. Thus, the expectation value of the axial frequency shift at modified cyclotron mode energy $E_+ = \frac{m\omega^2 r_+^2}{2}$

is

$$\langle \Delta\nu_z \rangle = a(C_4, B_2)\langle r_+^2 \rangle \sim \langle E_+ \rangle, \tag{5.16}$$

where a is a proportionality constant. The excited cyclotron radius r_+ depends on the thermal cyclotron radius and the phase relation ($\Delta\phi$) between the excitation pulse and the ion's random thermal motion at the excitation's beginning. If r_{therm} is the thermal radius and r_{exc} is the excitation radius, the excited modified cyclotron radius is

$$r_+^2 = |\vec{r}_{\text{exc}} + \vec{r}_{\text{therm}}|^2 = r_{\text{exc}}^2 + 2r_{\text{exc}}r_{\text{therm}}\cos(\Delta\phi) + r_{\text{therm}}^2. \tag{5.17}$$

Therefore, the expectation value of the axial frequency shift can be rewritten as [30],

$$\begin{aligned} \langle \Delta\nu_z \rangle &= a\langle r_{\text{exc}}^2 + r_{\text{therm}}^2 \rangle \\ \because\ r_{\text{exc}} &\gg r_{\text{therm}} \\ \Rightarrow \langle \Delta\nu_z \rangle &= a r_{\text{exc}}^2, \end{aligned} \tag{5.18}$$

where r_{exc} is constant for a particular excitation strength and a is dependent on C_4 and B_2. The standard deviation of the axial frequency shift is

$$\delta(\Delta\nu_z) = b r_{\text{exc}}, \tag{5.19}$$

where b is dependent on C_4, B_2, T_+ and

$$b \approx 2a\sqrt{\frac{4}{\pi} - \frac{1}{2}}\sqrt{\frac{\pi k_B T_+}{2m\omega_+^2}}. \tag{5.20}$$

The details on this definition of b can be found in [30].

The measurement of the axial frequency shift is repeated numerous times and also for several modified cyclotron radii to determine the axial frequency jitter. The observed jitter results from the thermal fluctuations and uncertainties involved in the dip measurements, mainly voltage fluctuations and dip fits. The thermal fluctuations are related to the excitation amplitudes, whereas the fluctuations associated with the axial frequency determination are independent of the small excitation amplitudes we use for the temperature measurement. These different fluctuations sum in quadrature, and Eq. (5.19) can be modified to

$$\delta(\Delta\nu_z) = \sqrt{(b\, r_{\text{exc}})^2 + b_0^2}, \tag{5.21}$$

where b_0 denotes the technical jitter. The Eq. (5.18) and (5.21) can be fitted to the axial frequency shift as a function of modified cyclotron radius squared r_+^2 and the standard deviation of axial frequency shifts as a function of modified cyclotron radius, respectively. If higher-order contributions are involved in the frequency shifts at slightly larger

excitation radii, Eq. (5.18) and (5.21) can be modified as $\Delta\nu_z \approx a\, r_{\text{exc}}^2 + a_1\, r_{\text{exc}}^4$ and $\delta(\Delta\nu_z) = \sqrt{(b\, r_{\text{exc}} + b_1\, r_{\text{exc}}^3)^2 + b_0^2}$, which are used in this work. The constants 'a' and 'b' can then be extracted from these fits. To further amplify the frequency shifts and the associated jitter, the trap was detuned by artificially introducing a large well-defined C_4 by adjusting the TR away from the TR_{opt}. Then $C_4 = D_4(\text{TR} - \text{TR}_{\text{opt}})$ (see section 5.2). An example of such a measurement is shown in Fig. 5.8, where $C_4 = 3.0(1) \times 10^{-3}$ was chosen.

The modified cyclotron temperature can be deduced from Eq. (5.20) as

$$T_+ = \frac{2m\omega_+^2 b^2}{4\pi k_B a^2 \left(\frac{4}{\pi} - \frac{1}{2}\right)}. \tag{5.22}$$

The expectation value of the axial energy in thermal equilibrium can be determined from

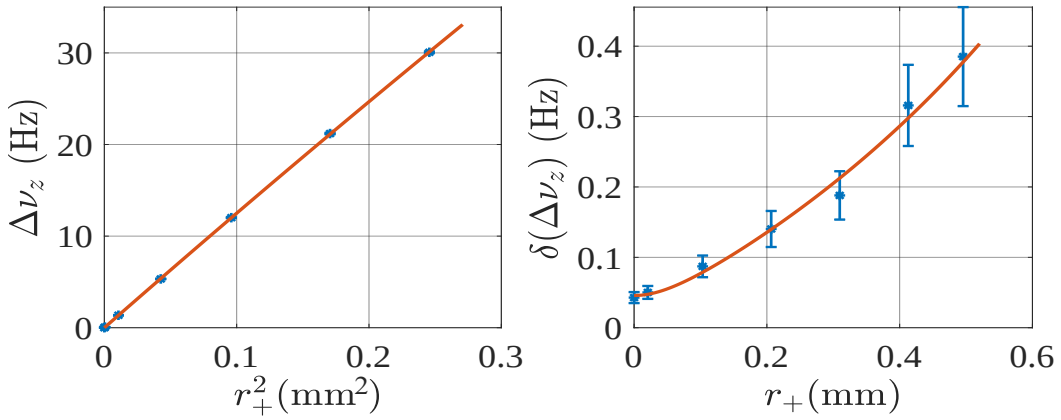

(a) Temperature measurement of the ion with electronic feedback.

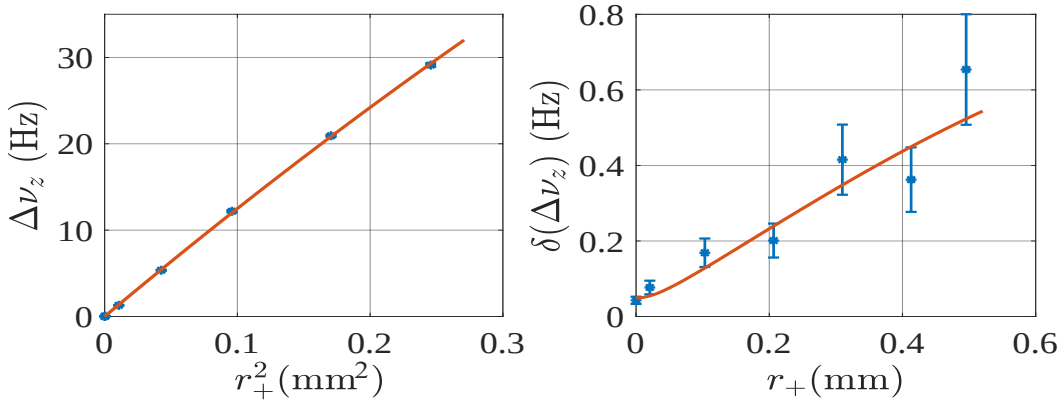

(b) Temperature measurement of the ion without electronic feedback.

Figure 5.8. Temperature measurement of a $^{12}C^{6+}$ ion. The axial frequency shift is measured as a function of the modified cyclotron radius r_+ in a detuned trap. On the left inset of (a) and (b) is the axial frequency shift plotted as a function of r_+^2. The parameter a can be estimated from the fitted slope of this dependency. On the right inset of (a) and (b), The measured frequency jitter is plotted against r_+; with a fit to this data set, the parameter b can be estimated. The fit functions are described in the text. In this measurement, the axial temperature without feedback, $T_z = 4.22(2.06)$K and with feedback, $T_{z,FB} = 1.25(67)$K.

Table 5.1. A summary of the temperature of the axial motions of $^4He^{2+}$ and $^{12}C^{6+}$ ions. For details, see text.

	$T_z(K)$	
Ion	Feedback	No Feedback
Helium	1.7(4)	3.3(1.1)
Carbon	1.5(6)	5.9(1.5)
wtd avg[3]	1.7(3)	4.3(9)

the radial energy and the ratio of frequencies (see section 3.4):

$$T_z = \frac{\omega_z}{\omega_+} T_+. \tag{5.23}$$

Such measurements were repeated for $^{12}C^{6+}$ and $^4He^{2+}$ multiple times during the campaign, both with and without electronic feedback. In table 5.1, the axial temperatures are summarised for both ions. Although the same detection system thermalizes both ions, different varactor settings are used, which could lead to a slight difference in the temperature between the ions. The results can be crosschecked using Eq. (5.13), as we know the C_4 and compensated B_2 during the temperature measurement. Taking the measurement plotted in Fig. 5.8a as an example, the fitted slope ($P_1 = \frac{\Delta\nu_z}{r_+^2}$) is $127(1)\,\mathrm{Hz\,mm^{-2}}$ whereas the slope calculated using Eq. (5.13) is $134(5)\,\mathrm{Hz\,mm^{-2}}$. The uncertainty in the calculated slope includes the uncertainty of B_2 and C_4 (which arise from the uncertainty of D_4). The values of the measured and calculated slopes are in reasonable agreement and form a good crosscheck for our systematics.

5.5 Trap alignment

The tilting mechanism described in section 4.8 can be used to achieve alignment between the magnetic field axis and the electric field axis in situ. Initially, to check the tilt of the trap and roughly align the trap, we used a $^{12}C^{4+}$ ion and measured its eigenfrequencies. Using Eq. (2.53) and the assumption $\epsilon = 0$, $\theta = 0.83(3)^\circ$ was estimated considering a $0.2\,\mathrm{Hz}$ uncertainty for ν_-. The adjustments to align the trap are then made by measuring the axial frequency as a function of the tilt θ [58] as

$$\begin{aligned} \nu_{z,tilt} &= \nu_{z,0}\sqrt{1-\frac{3}{2}\sin^2\theta} \approx \nu_{z,0}\left(1-\frac{3}{4}\theta^2\right) \\ \Rightarrow \nu_{z,0} &= \frac{\nu_{z,tilt}}{\left(1-\frac{3}{4}\theta^2\right)}. \end{aligned} \tag{5.24}$$

where $\nu_{z,tilt}$ is the axial frequency in the tilted trap and $\nu_{z,0}$ is the axial frequency in an aligned trap when $\theta = 0$. To find $\nu_{z,0}$, the frequency that should be achieved to align the trap, Eq. (5.24) can be used along with the estimated θ, in this case, $0.83(3)^\circ$. We evaluated

that about $74(5)$ Hz shift in the axial frequency should be achieved to align the trap. An attempt was made by turning the mechanical feedthroughs (adjustment screws) of the tilting mechanism discussed in section 4.8. Once we attained an axial frequency shift of 55.4 Hz, it got challenging to turn the adjustment screws further as stress was built on the fiber-glass rods that helped the adjustment process.

In due course, all the eigenfrequencies were measured with higher precision and accuracy, which could be used to get an exact measure of the tilt of the trap. Using the frequencies, the right-hand-side of the following Eq. (5.25) was solved

$$\begin{aligned} \frac{9}{4}\theta^2 - \frac{1}{2}\epsilon^2 &= \frac{1}{\omega_-}\left(\omega_+ - \omega_- - \sqrt{\omega_+^2 + \omega_z^2 + \omega_-^2}\right), \\ \frac{9}{4}\theta^2 - \frac{1}{2}\epsilon^2 &= 1.558(8) \times 10^{-4}. \end{aligned} \tag{5.25}$$

This result is a positive number indicating that θ is dominant over ϵ from which $\theta = 0.477(1)^\circ$ is evaluated when neglecting ϵ.

5.6 Image charge shift measurement

Image charge shift (ICS) is one of the leading order energy-independent shifts at LIONTRAP, as described in section 3.1.9. This effect was directly measured during the proton mass measurement campaign with a relative precision of 5% [81]. Then, the contribution from the tilt fluctuations was believed to be the limiting factor. Therefore, the tilting mechanism (section 4.8) was installed to adjust the tilt and improve the alignment for the next measurement campaign of the deuteron mass. A new measurement in the better-aligned trap was performed to improve the precision level for the image charge shift, which will be detailed in this section. This measurement occurred towards the end of the deuteron (d) mass measurement campaign and before the experiment was adjusted for the ^{4}He mass measurement.

5.6.1 Measurement principle of ICS

The ICS measurement was carried out by measuring the eigenfrequencies of both (d and $^{12}C^{6+}$) ions, which have significantly different masses. The frequencies of these single ions were measured alternately at the same trapping potential, and the frequency difference between the ions enables a precise determination of the ICS [81]. Due to translational symmetry in the axial direction, the ICS is negligible for the axial frequency (10^{-6} - 10^{-7} Hz) but notably large for the radial frequencies ($\sim 10^{-4}$ Hz) [81]. Due to the magnetic fluctuations and uncertainty in the literature mass, the measurement of ICS using the modified cyclotron frequency would be limited. Neglecting the retardation effects, [4] the ICS remains same for

[4] Due to the eigenmotions of the ion, the image charges are not static and could lead to frequency-dependent 'cavity shifts' (retardation effects), which become significant for electrons. However, due to the small trap size and comparatively low frequencies of atomic ions, the wavelength associated with eigenmodes of the trapped ion are much larger than the trap size and these effects can be neglected. See section 3.1.9.

magnetron and modified cyclotron mode with a difference in sign. Thus, the magnetron frequency ($\Delta\nu_-^{\text{exp}} = \nu_-(^{12}\text{C}^{6+}) - \nu_-(d)$) is studied to evaluate ICS.

To achieve a relative precision of below 5%, a more sensitive measurement than the double-dip technique was employed. This method involved a Ramsey-like phase-sensitive measurement of the magnetron frequency. The PnA technique usually used in our experiment is avoided, as the magnetron frequency is small, and the second pulse in the PnA routine with frequency $\nu_- + \nu_z$ is very close to the axial frequency of the ion, which results in axial excitation and thus causes changes in the magnetron phase. Recently it was demonstrated that such a measurement becomes possible when applying pulse shaping for the excitation [99].

In the Ramsey-like phase-sensitive measurement, two identical dipolar pulses at the magnetron frequency ν_-, separated by an evolution time T_{evol}, are applied to the ion. The first pulse excites the thermalized magnetron mode (see section 3.2.3) and imprints a phase. Then the ion evolves freely during T_{evol}, until the second pulse is applied. The magnetron motion increases or decreases depending on the relation between the ion's phase after T_{evol} and the phase of the second pulse. The final magnetron radius oscillates periodically with the magnetron frequency depending on the T_{evol} as [81]:

$$(r_-^{\text{exc}})^2 = \frac{(r_-^{\text{max}})^2}{2}\left(1 + \cos\left[2\pi\nu_- T_{\text{evol}} + \phi_0\right]\right) + (r_-^{\text{therm}})^2, \tag{5.26}$$

where r_-^{max} is the maximum excited radius and r_-^{therm} is the thermal magnetron radius. The excited radius is detected by measuring the axial frequency shift in an artificially detuned trap by introducing large C_4 and C_6. The frequency shift due to this deformed potential is given by Eq. (5.3) for different r_-^{exc}.

The magnetron frequency can be determined from the phases at different evolution times:

$$\nu_- = \frac{1}{2\pi}\frac{\phi(T_{\text{evol},1}) - \phi(T_{\text{evol},2})}{T_{\text{evol},1} - T_{\text{evol},2}}. \tag{5.27}$$

Every phase is determined from the measurement of one period of the Ramsey-like oscillations. The T_{evol}s are chosen such that a set of times around a short evolution time and a set of times around the long evolution time is formed by adding a fixed offset from 0 to $\frac{1}{\nu_-}$ equally spaced depending on the number of frequency shift measurements required and a random offset between 0 and 1 period of the oscillation ($\frac{1}{\nu_-}$) to make these measurements randomly spaced.

5.6.2 ICS measurement cycle

The measurement cycle is described in Fig. 5.9. A random ion is chosen to be measured first in the PT, and at the same time, the second ion is stored in one of the STs. The first step is to cool the ion's motions. The axial frequency of the cold particle in an optimized trap, which

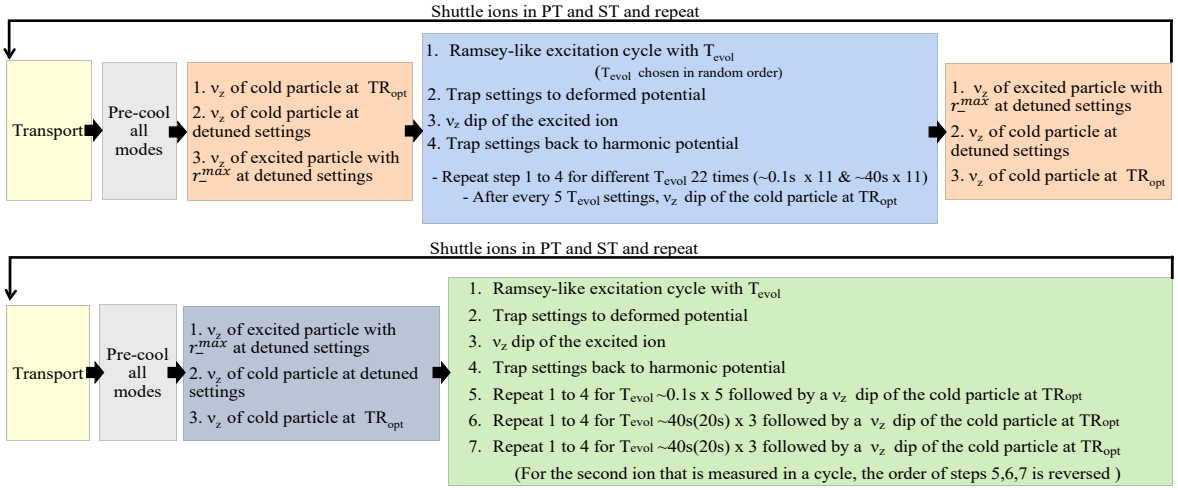

Figure 5.9. Sequences performed in a measurement cycle. On the top, a measurement routine where the magnetron phase measurements with different evolution times were performed in a random order is depicted. 66 measurement cycles were performed using this routine. On the bottom, a measurement routine with a fixed order of the magnetron phase measurement is shown. 98 measurement cycles were performed using this routine.

is used to normalize the magnetron frequency, is recorded. This is followed by the axial frequency measurement of the cold and then the maximally excited particle in a detuned trap. The $r_-^{\max}$ used in this measurement is $\sim$270 µm. The thermal radius of deuteron and carbon at 4 K is $\sim$8 µm and $\sim$3 µm, respectively. Then, the Ramsey-like excitation cycles are performed with evolution times around $\sim$0.1s ($T_{\text{evol},1}$) and $\sim$40s or $\sim$20s ($T_{\text{evol},2}$) and corresponding measurements of the axial frequency of the excited ion in a detuned trap are performed. The axial frequency of the cold ion is recorded in both tuned and detuned trap at specific intervals, as shown in Fig. 5.9. In the next part of the measurement cycle, the same procedure is repeated with the second ion, which is moved into the PT from the ST. Such measurement cycles are performed for both ions numerous times.

Hardware changes: When switching between the optimized trap setting and the deformed potential setting, the high-precision voltages on the electrodes must be manipulated, which could lead to voltage fluctuations and drifts. To avoid this effect, the voltage manipulations between the two settings were done by mixing voltages from different channels of the voltage source via a voltage divider and relay, as shown in Fig. 5.10. The anharmonic coefficients introduced to detune the trap are C_4 = -0.00276 and C_6 = 0.0125.

5.6.3 Evaluation of ICS

The measured axial frequency shifts are then plotted as a function of the evolution times but corrected for voltage fluctuations ($T_{\text{evol}}^{\text{corr}}$); see Fig. 5.11. From a fit to this plot, the phase can be determined, and consequently, the magnetron frequency using Eq. (5.27). Here, the measured magnetron frequencies of the ions are corrected for voltage fluctuations, which

helps to reduce the statistical uncertainty. Intermediate measurement of axial frequencies during the measurement cycle helps to monitor voltage fluctuations. Based on the known frequency values from the intermediate axial frequency measurements, the axial frequency during the Ramsey-like measurements of the magnetron frequency is interpolated (using the 'interp1' MATLAB function). Using the interpolated axial frequencies (ν_z^{interp}), the magnetron frequency can be corrected by correcting the magnetron phase evolution time as[5]:

$$T_{\text{evol}}^{\text{corr}} = \frac{T_{\text{evol}}}{1 - \frac{2(\nu_z^{\text{interp}} - \nu_z^{\text{off}})}{\nu_z^{\text{off}}}}, \tag{5.28}$$

where ν_z^{off}(C) = 462453.8 Hz and ν_z^{off}(d) = ν_z^{off}(C)/R Hz and R is axial frequency ratio. Here, the measured axial frequency ratio $R_{\text{meas}} = \frac{\nu_z(^{12}\text{C}^{6+})}{\nu_z(d)} = 1.003520155(10)$ is used for the voltage corrections. R_{meas} is used so that no systematic shifts, known or unknown, or any unaccounted drifts are excluded. The frequency ratio is extracted from about 800 ν_z measurements of the cold ion at optimum TR.

After performing 164 ICS measurement cycles, the statistical result of the magnetron frequency diffrence is (see Fig. 5.12):

$$\Delta\nu_-^{\text{stat}} = \nu_-(^{12}\text{C}^{6+}) - \nu_-(d) = 0.960(50)\ \text{mHz}. \tag{5.29}$$

The total statistical uncertainty that is presented is the statistical uncertainty of 46 µHz scaled up by the factor $\sqrt{\chi^2} = \sqrt{1.2}$.

To find the exact shift due to ICS, the difference in the ideal magnetron frequencies of the ions, $\Delta\nu_-^{\text{ideal}}$= -3.339 mHz, is subtracted. Then

$$\Delta\nu_-^{\text{meas}} = 2.379(50)\ \text{mHz}. \tag{5.30}$$

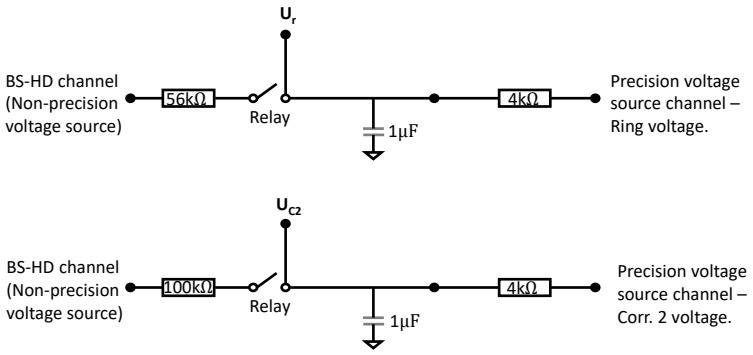

Figure 5.10. Schematic of the relay setup used during ICS measurement to switch between different voltage settings of the trap without disturbing the settings of the high-precision-voltage source.

[5]More details of how this correction is carried out are given in Appendix A of [81]

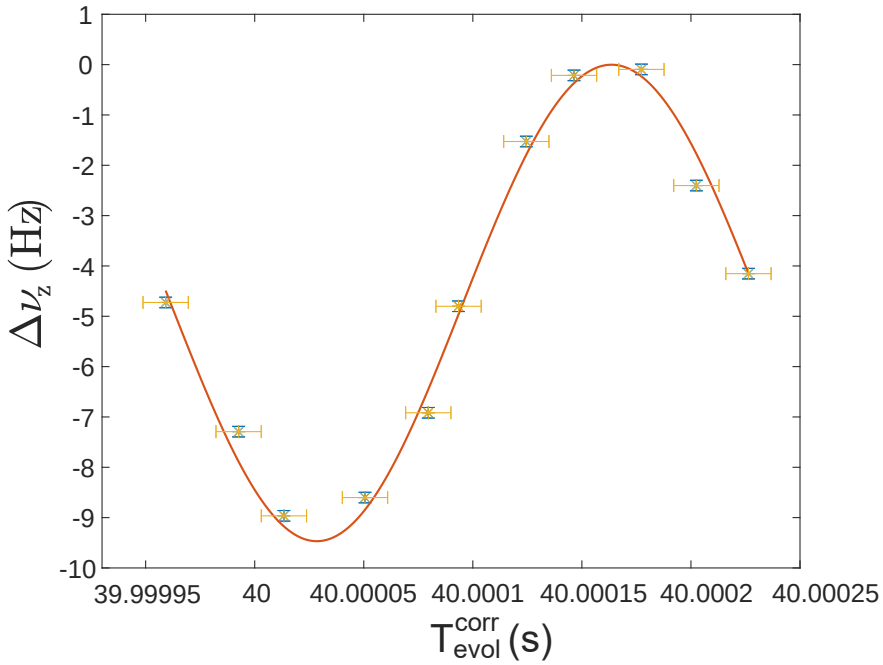

Figure 5.11. An example of magnetron phase determination. The axial frequency shifts (on the y-axis) are observed after Ramsey-like excitations at different evolution times (on the x-axis). The uncertainty in the y-axis is due to the uncertainty of 100 mHz in the axial frequencies measured in the detuned trap and the intrinsic thermal distribution of the magnetron radius. The error bars on the x-axis are due to the uncertainty of 70 mHz in the axial frequency measurements at the $\mathrm{TR}_{\mathrm{opt}}$. These points are then fitted to extract the magnetron phase.

Systematic uncertainties of magnetron frequency difference: The resulting magnetron frequency difference should be further corrected for systematic shifts due to the residual magnetostatic inhomogeneity, electrostatic anharmonicity, special relativity effects, tilt, and ellipticity to find the shifts from ICS alone. In this campaign, with the tilting mechanism installed, the tilt of $0.56(7)^\circ$ during the ICS measurement in the proton mass campaign was reduced to the order of $0.05(5)^\circ$ [30]. With this, the ellipticity could be estimated with better precision in a way that does not limit the ICS measurements [30]. The magnetostatic inhomogeneity was also minimized by installing a shim coil [22]. As a result, residual shifts due to special relativity, the quadratic component of the magnetic field B_2, and electrostatic anharmonicity in total amount to <1 µHz.

Uncertainties from voltage correction: The axial frequency ratio R_{meas} (voltage correction) is also susceptible to systematic shifts such as energy-dependent shifts caused due to imperfections in the fields, shifts dependent on the uncertainty in the resonance frequency of the detection system, and trap tilt. The shifts due to magnetostatic inhomogeneity and tilt are negligible in this campaign, as explained above. Another systematic uncertainty arises from the fitting routine of the dip. The axial frequencies recorded during the ICS measurement in the detuned trap occur in the presence of a large C_4. The fit model assumes a tuned trap with

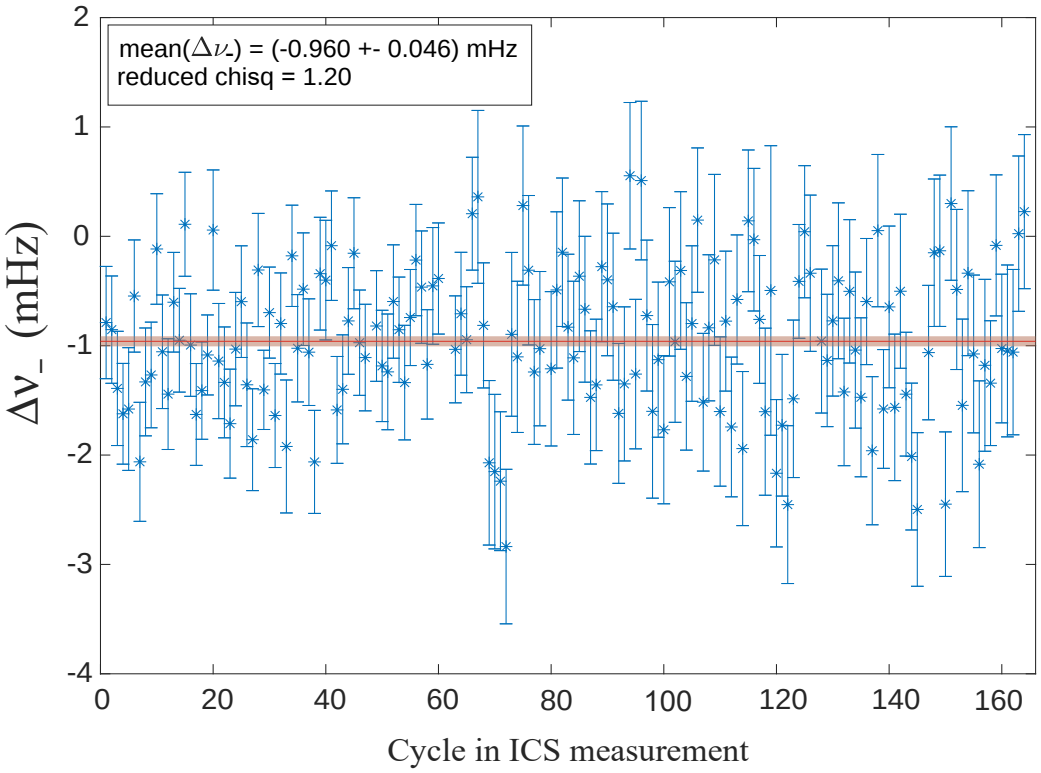

Figure 5.12. Measurement of magnetron frequency differences. The red line indicates the mean value, and the shaded red region indicates the statistical uncertainty. For details, see text.

negligible C_4. This deviation causes a small systematic error that shifts the magnetron frequency by $<20\,\mu$Hz. As mentioned earlier, the T_{evol} is corrected using R_{meas}, which mainly influences the long evolution times; see Eq. (5.27). This then causes uncertainty in the magnetron frequency which can be derived by performing error propagation on Eq. (5.27) and Eq. (5.28) as $\delta\nu_m = 2\nu_m \delta R_{\text{meas}} \approx 80\,\mu$Hz [81].

Adding up all the uncertainties gives the following magnetron frequency difference:

$$\Delta\nu_-^{\text{exp}} = 2.379(96)\ \text{mHz}. \tag{5.31}$$

The theoretical value predicted by a full COMSOL simulation of our trap geometry described in section V of [81] is

$$\Delta\nu_-^{\text{theo}} = 2.377(21)\ \text{mHz}. \tag{5.32}$$

The ICS is measured with a relative precision of 4% and entirely agrees with the theory. Suppose we include the axial frequency ratio measured during the deuteron mass campaign, the total uncertainty in $\Delta\nu_-^{\text{exp}}$ drops to $\approx 70\,\mu$Hz and the relative precision of the measured ICS would be 3.2%. Although the agreement with the theory is excellent, the precision is not improved significantly compared to the previous ICS measurement. The limiting factor

is the uncertainty in the measured axial frequency ratio. One of the main reasons for this uncertainty arises from the axial frequency extraction using a lineshape model. It is often limited by the lack of knowledge of the resonator parameters, such as resonance frequency and quality factor (section 6.4.5).

A different approach was then tried, which does not involve systematics from the dip lineshape. Here, the axial frequency measurement of an ion thermalized in its magnetron mode at TR_{opt} is extracted from the peak instead of the dip. To this end, in the new measurement cycles, each intermediate dip measurement was replaced by four consecutive peak measurements with decreasing SNR as the ion cools slowly to extract the axial frequency and to avoid dependence on the lineshape model. However, on detailed analysis, it was found that using this method, the shot-to-shot precision of the axial frequency ratio was worse and was limited by the axial frequency stability between measurement cycles and sub-cycles with different ions. The main reasons for axial frequency instability could be (1) The precision achieved in axial frequency measurement per shot and the jitter between individual shots. (2) The fluctuations in the trapping potential (voltage drifts). (3) Jitter due to transports in a measurement cycle, the jitter was observed to be $\sim$80 mHz due to transport compared to $\sim$40 mHz without transport. Hence, the shot-to-shot precision and the jitter between the runs of the axial frequency measurements need to be improved for further improvements in ICS measurement. Measuring ICS using ions with larger mass difference can also lead to improved results.

6. Mass measurement

This chapter discusses the mass measurement principle, the measurement routine, the statistical analysis of the data, and the evaluation of shifts due to systematic effects. Towards the end of the chapter, I present the final results of the mass measurement campaign, the limitations of the mass measurement, and possible improvements. The results discussed in this chapter are reported in a paper that has been recently accepted for publication [92].

6.1 Measurement principle

The high-precision mass determination of a stable ion is based on comparing cyclotron frequencies of the ion of interest and a reference ion in the same magnetic field, allowing the cancellation of the magnetic field in $\nu_c = \frac{1}{2\pi}\frac{qB}{m}$ (Eq. (2.1)). The mass of the ion of interest is

$$m = \frac{q}{q_{\text{ref}}}\frac{\nu_c^{\text{ref}}}{\nu_c} m_{\text{ref}}. \tag{6.1}$$

$\frac{q}{q_{\text{ref}}}$, the charge ratio is a ratio of integers. The goal of the experiment is to measure the cyclotron frequency ratio $R^{\text{CF}} = \frac{\nu_c^{\text{ref}}}{\nu_c}$ with the highest precision. Usually, the reference ion is chosen such that its mass, m_{ref}, is well known. In this work, we choose a carbon $^{12}C^{6+}$ ion as a reference for a $^{4}He^{2+}$ ion. This way, the result can be given directly in the atomic mass unit (u), which is defined to be $\frac{1}{12}$ of the mass of a ^{12}C atom. The mass of $^{4}He^{2+}$ can be expressed as

$$m(^{4}\text{He}^{2+}) = \frac{2}{6}\frac{\nu_c(^{12}\text{C}^{6+})}{\nu_c(^{4}\text{He}^{2+})} m(^{12}\text{C}^{6+}). \tag{6.2}$$

The mass of an atom is related to the mass of its ion via the ionization energies [98] and the mass of the missing electrons [32] without relevant loss of precision in the low Z regime. Here, we can relate the mass of the atom to that of the fully stripped $^{12}C^{6+}$ ion by adding the total electronic binding energy E_b and subtracting the masses of the missing electrons. The individual binding energies $E_{b,i}$, which are summed to get E_b, are given in table 6.1. The masses of the missing electrons are taken from the current CODATA2018 compilation: $m_e = 5.485\,799\,090\,65(16)\times10^{-4}\ u$ [32].

$$\begin{aligned} m(^{12}\text{C}^{6+}) &= 12\ u - 6m_e + \sum_{i=1}^{6}\frac{E_{b,i}}{c^2} \\ &= 11.996\,709\,626\,412\,47(35)\ u \end{aligned} \tag{6.3}$$

The relative uncertainty of the mass of $^{12}C^{6+}$ is in sub-parts-per-trillion. Further details on the calculation of the atomic masses will be discussed in 6.5.

Table 6.1. Electronic binding energies of carbon and helium atoms [98]. The values in the table are related to atomic mass units (u) as $eV/c^2 = 1.073\,544\,102\,33 \times 10^{-9}$ u

Charge state	Binding energy (eV) C	Binding energy (eV) He
+1	11.2602880(11)	24.587389011(25)
+2	24.383143(12)	54.4177655282(10)
+3	47.88778(25)	
+4	64.49352(19)	
+5	392.090518(25)	
+6	489.99320779(22)	

6.2 Measurement procedure

As mentioned in the previous section, the cyclotron frequency measurement of both ions should take place in the same magnetic field to be able to use Eq. (6.1) to find the mass of the ion of interest. The ideal scenario would be to measure both ions **simultaneously at the same position**. The group of David Pritchard at MIT has successfully implemented and used a method that comes very close to this ideal condition by storing both ions together in a trap in a common magnetron orbit and simultaneously measuring the cyclotron frequencies [100, 101]. In this case, the impact of any spatially homogeneous, temporal fluctuations of the magnetic field will be nulled. However, the additional systematics due to the interactions between the ions in the same trap has to be carefully identified and treated. Moreover, this measurement principle requires using q/m doublets, and additionally, it is advantageous to use mass doublet to avoid the effects of inhomogeneities like B_2. A test of such a simultaneous measurement was conducted at LIONTRAP and is presented in section 6.7.1

For the comparison of ^{4}He and ^{12}C, which have a large mass difference, at LIONTRAP, we use a shuttling method to measure the cyclotron frequencies. The method minimizes the ion-ion interactions and almost achieves the ideal condition in the following way:

Same (similar) time: In the shuttling method, the measurements are not simultaneous, but short shuttling times are used to come close to the ideal condition. Here, single ions are prepared and stored in separate potential minima before the measurements. Then the cyclotron frequency measurement occurs in the PT on one ion, while the second ion is stored in one of the STs. Once the cyclotron frequency of the first ion, ν_c (ion-I), is measured, it can be transported to the unoccupied ST, and the second ion can be transported to the PT, where ν_c (ion-II) is measured. See Fig. 6.1, where an example is given with ion-I as $^4He^{2+}$ and ion-II as $^{12}C^{6+}$. The measurement sequence is arranged such that the modified cyclotron frequency measurements with long evolution time, which gives the highest precision but at the same time is most susceptible to magnetic field drifts, are performed in quick succession. As the ions are stored adjacently, they can be transported between the traps in a short time,

reducing the effect of temporal magnetic field fluctuations.

Same position: For both ν_c measurements, the same trap configuration with identical trapping potential ensures the ions are at the same position in the trap. Using the same trapping potential allows us to circumvent shifts in equilibrium position due to patch potentials, as discussed in section 2.2. The ν_c measurement method we use requires the ion's axial frequency to be in resonance with the detection system. However, since both ions have slightly different axial frequencies, either the trap potential needs to be adjusted to bring the ion in resonance to the tank circuit, or the frequency of the detector tank circuit(s) has to be tuned to the ions individually. The latter method is chosen because keeping the trapping potential constant makes sure that the position of the ions within the trap is unchanged. For ions with

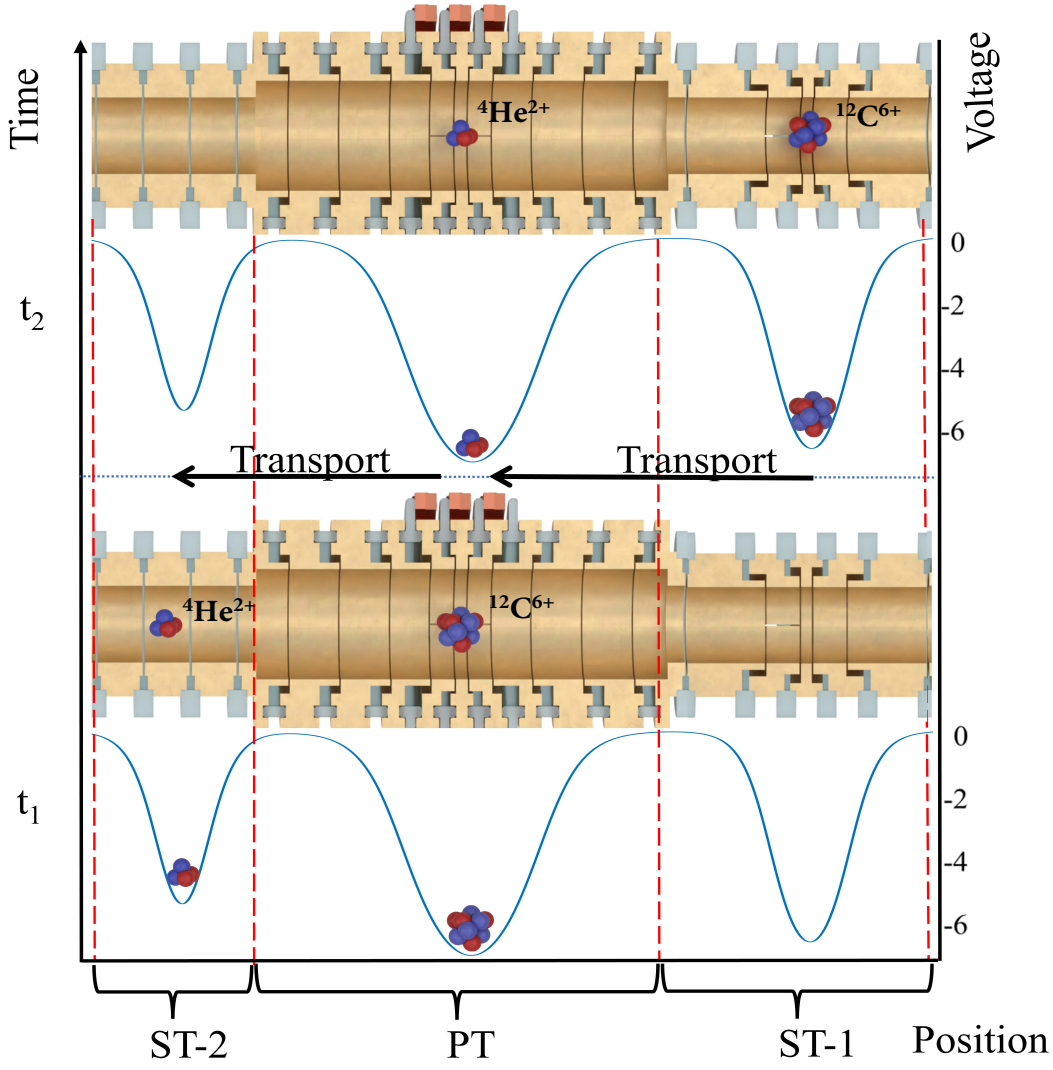

Figure 6.1. An example of shuttling of ions for cyclotron frequency measurements. At the beginning of the mass measurement campaign, ions of interest are loaded into the trap and stored simultaneously in separate traps. While $\nu_c(^4He^{2+})$ is being measured in the PT during time t_1, $^{12}C^{6+}$ is stored in one of the STs. After the measurement, $^4He^{2+}$ is moved to the other ST, and $^{12}C^{6+}$ is moved into the PT to measure $\nu_c(^{12}C^{6+})$ during time t_2.

large q/m mismatch, such as in [21], it requires two separate resonators. In this work, it suffices to use a varactor diode to tune a single resonator to get it in resonance with the ions.

The shuttling method with a tunable resonator (or multiple resonators) has the advantage that the ions do not require to be a mass doublet or a q/m doublet.

6.2.1 Measurement cycle

A measurement cycle includes the measurement of the cyclotron frequency of individual helium and carbon ions, and each cycle generates a cyclotron frequency ratio, $R^{\mathrm{CF}} = \frac{\nu_c(^{12}\mathrm{C}^{6+})}{\nu_c(^{4}\mathrm{He}^{2+})}$. Several such cycles are performed in a run. These measurement cycles are completely automated until interrupted for refilling the liquid helium and nitrogen into the apparatus or magnet reservoirs. Usually, the measurement cycles between two fillings of the apparatus form a run. Each run has a fixed excitation amplitude setting; more details are in section 6.3.

At the beginning of each run, the resonator spectra without the ion in resonance are recorded with and without electronic feedback (see section 3.2.5). The resonator spectra are recorded to extract the resonator parameters by fitting them with a lineshape model (see section 3.1.2.1 and section 3.1.2.2). This is followed by setting all the devices and voltages in the required configuration. The measurement cycle is described in steps below and is also summarised in Fig. 6.2

1. One of the ions is **randomly chosen** at the start of every cycle to avoid systematic errors caused by linear drifts of the magnetic field or transports in a fixed direction at the beginning of each cycle.

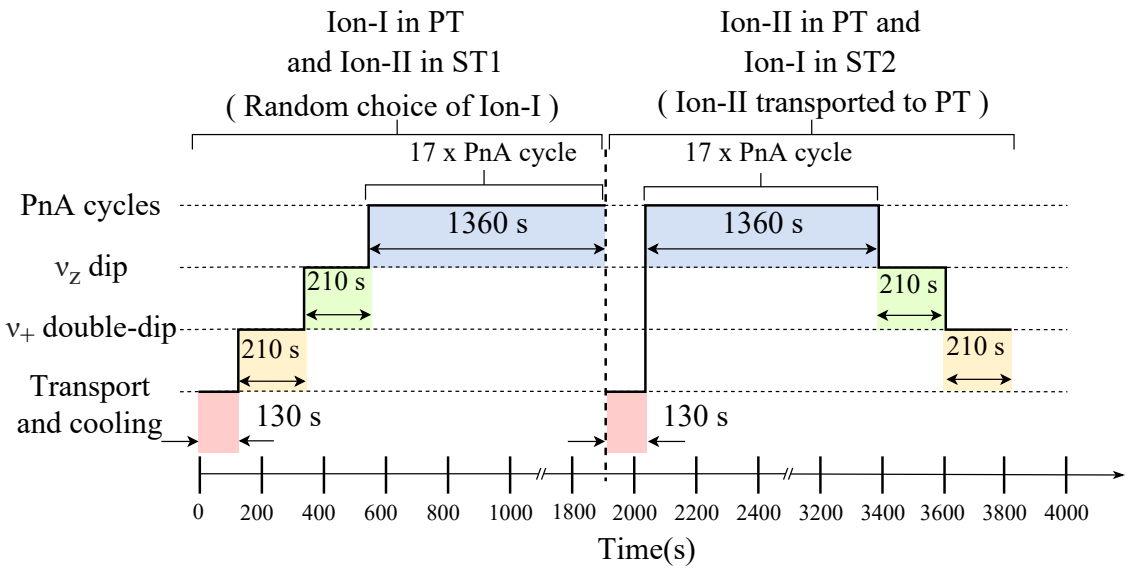

Figure 6.2. Timeline diagram of a measurement cycle [92]. At the beginning of a cycle, ion-I is selected randomly and transported to PT, where all the modes are cooled, and the ν_z (dip) and ν_+ (double-dip) are measured, followed by a ν_+ (PnA) measurement. Ion-I is then moved away, ion-II is transported to the PT, and the frequencies are measured in the inverse sequence. The time periods mentioned are only approximate.

2. If that ion is not already in the PT, it is **transported** there from the ST, and the ion in PT is moved to the other ST. All the eigenmodes of the ion are **cooled** in the PT by coupling to the axial resonator. The magnetron and cyclotron modes' cooling times were 30 s each.
3. ν_+ is measured using the **double-dip** method. The ν_+ measured using double-dips are not used for the final mass determination due to the disadvantages mentioned in section 3.2.4. Nevertheless, the double-dip measurement is a strong cross-check and a starting point for the phase-sensitive determination of ν_+.
4. ν_z is measured via recording a **dip**. The dip and double-dip are recorded with an averaging time of 209 s, and FFT spectra of length 32.8 s are taken.
5. Finally, the ν_+ is measured phase-sensitively using the **PnA method**. In every measurement cycle, the PnA measurement of ν_+ consists of 17 PnA cycles described in section 3.3, each performed with a different evolution time T_{evol} : 6×0.1 s, 0.5 s, 1 s, 2 s, 5 s, 10 s, 6×20 s. The short evolution times (0.1 s) are used for initial phase determination, and the long evolution times (20 s) enable the determination of ν_+ with the highest precision. The other evolution times in between allow phase unwrapping. The slightly longer short evolution time compared to the previous measurement campaigns [30, 90] was chosen to avoid any effects from the rectifying action of the cryogenic switch in our excitation lines (see section 4.4.3.1).
6. Afterwards, the ion in the PT is transported to the unoccupied ST, and the second ion is moved into the PT, where frequency determinations (steps 3, 4, and 5) are performed in reverse order. This process is done so that the high precision ν_+ measurements of the two ions are performed as close in time as possible to minimize the jitter of the magnetic field. The time between the measurements of the two modified cyclotron frequencies is around 5 min.

After one cycle of 63 min, the whole procedure repeats continuously until interrupted for filling or otherwise. The magnetron frequency is not measured in each cycle but occasionally during the measurement campaign using the double-dip method (see section 3.2.4). It is calculated from the measured axial and modified cyclotron frequencies for every cycle using Eq. (2.16). The measured axial and modified cyclotron frequencies and the calculated magnetron frequency can be used to calculate the free cyclotron frequency using the invariance theorem.

The mass measurement campaign used two ion pairs stored in different spatial orders. Different ion arrangements are chosen to avoid any systematic effects originating from the order of ions or unnoticed contaminant ions.

6.3 Statistical evaluation

The final mass analysis uses 32 runs with a total of 482 R^{CF} measurements. 208 measurements were performed with $^4He^{2+}$ as the upper ion and 274 measurements with $^{12}C^{6+}$ as the

upper ion. An 'upper ion' indicates that during its cyclotron frequency measurement in PT, the lower ion will be stored in ST-II.

As the first step in the analysis, the resonator spectrum recorded for each run is fitted, and the resonator parameters such as resonance frequency ν_{res} and quality factor Q are extracted. Then these resonator parameters are used to fit all the dips and double-dips in that run. These steps are performed for every run in the mass measurement campaign. The phases that resulted from the PnA measurement are then unwrapped and analyzed to determine ν_+. Some quality cuts are performed on the data for the final analysis. If the standard deviation (jitter) of multiple phases measured within a cycle obtained with long evolution times (20 s) exceeds the expected value due to possible unwrapping errors, the cycle is disregarded. The accepted tolerance of phase jitter is $55°$. The cycles where the dip fits did not converge correctly, which are identified by exit flags of the fit function, are also excluded. Measurement cycles performed for 3 to 4 hours right after filling are avoided. On average, we get a jitter[1] of $\sim 1.4 \times 10^{-10}$ for the measured R^{CF}.

Between different runs, the strength $S^+_{t,\hat{U},i}$ of the modified cyclotron frequency excitation during the PnA measurement and, consequently, the ion's cyclotron amplitude was varied. Here, $\hat{U}$ and t are the amplitude and duration of the excitation pulse, respectively, and the different excitation settings are denoted as i. This method allows us to extrapolate to zero excited modified cyclotron mode energy to find the ν_+ at zero cyclotron energy. These runs are then sorted based on the excitation settings. For each excitation setting i, the mean R^{CF}_i with uncertainty (standard error of the mean) was calculated for all the individual ratios generated from the measurement cycles in the sorted runs. The excitation strengths are related to the excited modified cyclotron radii as $r^+_{i,\text{exc}} = \kappa_+ S^+_{t,\hat{U},i}$, where κ is a calibration constant, which is known from a separate measurement (see section 5.3.1). The amplitude of the parametric amplification (Qxz) sideband pulse is adjusted to yield reasonable SNR for each cyclotron excitation strength (see section 3.3). During the measurement campaign, the r^+_{exc} of both ions were varied over a range of $10\,\mu$m to $80\,\mu$m between the runs.

6.3.1 Surface fit

Different motional amplitudes of the ions in different runs result in different relativistic shifts of the cyclotron frequency of the ions. This shift is treated using a three-parameter surface fit that relates the individually shifted measurements R^{CF}_i to R^{CF}_{stat}, which is the frequency ratio extrapolated to zero cyclotron excitation energy (Fig. 6.3). This extrapolation to zero excitation energies helps to cancel out the shifts dependent on the excitation energies of the modified cyclotron mode. The frequency ratio is related to the squared excitation strengths of the ions as [30]:

$$R^{CF}_i = R^{CF}_{\text{stat}} + a[S^+_{t,\hat{U},i}(^4\text{He}^{2+})]^2 + b[S^+_{t,\hat{U},i}(^{12}\text{C}^{6+})]^2. \tag{6.4}$$

[1] The jitter is the average of the standard deviations of each run for all the measured R^{CF}s.

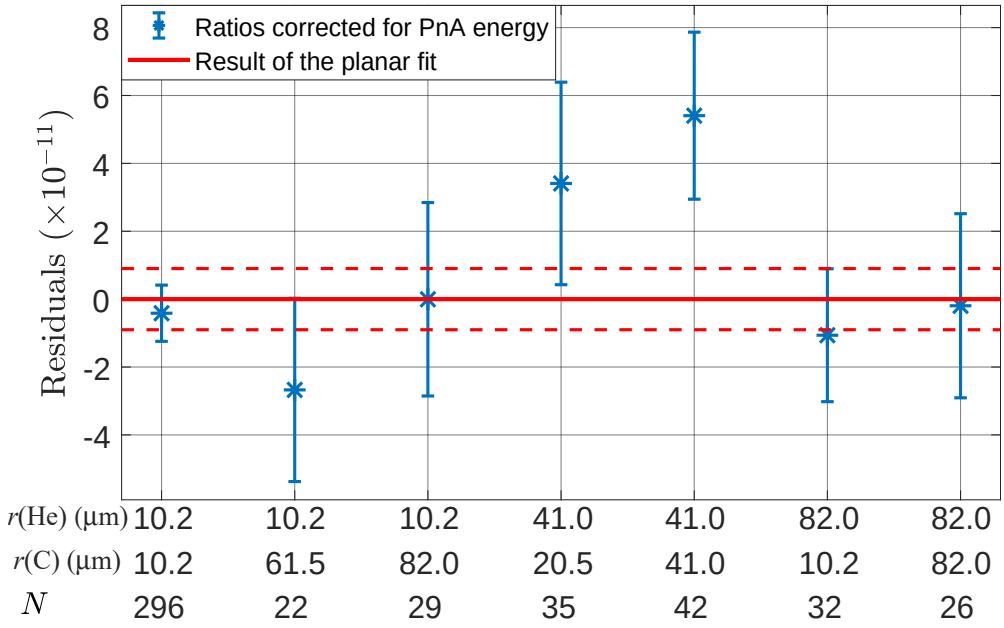

Figure 6.3. Residuals of the 3-parameter surface fit [92]. Individual points in the plot correspond to different PnA settings. The x-axis marks the respective cyclotron radii of $^4He^{2+}$ r(He) and $^{12}C^{6+}$ r(C) and the number of cyclotron frequency ratios used to obtain each value (N). Each point is the mean of the corresponding N measurements, and the error bar is the standard error of the mean. The y-axis shows the residuals of the surface fit for different excitation settings. The region between the dotted lines indicates the 1σ confidence interval of the frequency ratio extracted from the fit (R^{CF}_{stat}).

where R^{CF}_i and the excitation strengths $S^+_{t,\hat{U},i}(^4He^{2+})$ and $S^+_{t,\hat{U},i}(^{12}C^{6+})$ serve as input data for the three-parameter (R^{CF}_{stat}, a, b) fit. The frequency ratio extrapolated to zero cyclotron excitation energy is the result of the surface fit:

$$R^{CF}_{\text{stat}} = 1.000\ 650\ 921\ 128\ 8(90). \tag{6.5}$$

The data passes the null hypothesis test using the Kolmogorov-Smirnov and χ^2 goodness-of-fit tests. In other words, these tests do not reject the null hypothesis that the input data (R^{CF}_i) is normally distributed at a 5% significance level. The reduced χ^2 is 1.9 after performing the surface fit on the data. The probability of observing a χ^2 value as large or larger than the observed value is 11%.

The slopes a and b from the fit can be used to extract the calibration constant κ_+, and this can be compared to the direct measurement of the same described in section 5.3.1. Since the frequencies of $^4He^{2+}$ and $^{12}C^{6+}$ are not very far apart, and the same excitation lines are used for both species, the κ_+ values are approximately equal for both ions and the direct measurements were mainly performed on $^{12}C^{6+}$ [2]. The values of κ_+ from the mass measurement and direct measurements (section 5.3.1) are given in table 6.2 and are found to be in good agreement.

[2] Short measurements were performed with $^4He^{2+}$ to crosscheck.

Table 6.2. Calibration constant for the modified cyclotron excitation from surface fit.

κ_+ direct	κ_+ surface fit	
$^{12}C^{6+}$	$^{4}He^{2+}$	$^{12}C^{6+}$
0.02049(43)	0.02062(35)	0.02043(40)

6.4 Systematic shifts

The observed cyclotron frequency ratio, R^{CF}_{stat}, still needs to be corrected for systematic shifts. These shifts are summarized in table 6.3.

6.4.1 Relativistic shifts

While the nominal excitation radius is treated using the surface fit, the finite thermal radius of the ion leads to a residual relativistic shift in the cyclotron frequency. Before every PnA cycle, the ion's thermal cyclotron and axial amplitudes are reduced by thermalizing the ion with the axial tank circuit. To minimize the shift, electronic feedback cooling is implemented to lower the axial temperature of the ion; see section 3.2.5 and [63, 75]. This way, the axial temperature T_z is reduced from $4.2\,\text{K}$ to $T_{z,FB} = 1.7(3)\,\text{K}$. The relativistic shift is inversely proportional to mass and is smaller for carbon than helium (see section 3.4). The temperature measurements of the ions described in section 5.4 can be used to estimate the shift of $-1.77(31)$ ppt in the cyclotron frequency ratio.

6.4.2 Anharmonic electrostatic potentials

The PT in the LIONTRAP experiment is one of the most harmonic traps. It can be optimized to minimize the electrostatic anharmonicities to the extent that it does not significantly contribute to the uncertainty, as described in section 5.2. The residual electrostatic anharmonicities can be described by C_i-coefficients (i > 2) (see section 2.2.1). In the measurement campaign, the trap was optimized to have the combination of C_3^2 and $C_4 \leq 0(1) \times 10^{-5}$ and $C_6 \leq -4(15) \times 10^{-5}$ (see section 5.2.1). The exceptional harmonicity enables us to use larger excitation during the second PnA pulse. By this, we can achieve axial amplitudes large enough to observe a sufficiently strong peak signal even for the light lowly charged ions and have a reduced phase readout jitter (see section 6.6 and [30]). The C_i-coefficients only lead to a shift of $0(1) \times 10^{-13}$ in the cyclotron frequency ratio.

6.4.3 Residual magnetostatic inhomogeneity

The frequency shift in first order caused by the cylindrically symmetric magnetic field imperfections is contributed by the quadratic component B_2 of the magnetic field ($B = B_0 + B_1 z + B_2 z^2$ +..). At LIONTRAP, a superconducting shim coil has been implemented around the trap chamber to minimize B_2 in situ. The residual B_2 = $(-0.4 \pm 2.0)\,\text{mT}\,\text{m}^{-2}$. This method drastically reduced the frequency shift from the residual quadratic magnetic field

inhomogeneity and the axial thermal amplitude. The limit to which the magnetic field homogeneity can be optimized or B_2 can be nulled is given by the uncertainty in the electrostatic anharmonicities (mainly C_4 and C_3). The inhomogeneities can generate shifts of all the eigenfrequencies. The largest contribution is from the shift of the modified cyclotron frequency due to the finite axial energy. The contributions to the modified cyclotron and axial frequencies from the modified cyclotron mode energy drop out, and the shift of the magnetron frequency is negligible. The evaluated shift in the cyclotron frequency ratio due to the residual magnetostatic inhomogeneity is $0.03(19)$ ppt.

6.4.4 Image charge shifts

The image charge shift makes a significant contribution to the systematic error budget. This energy-independent shift is caused by the charges induced on the trap electrodes due to the oscillating ion. The shift in cyclotron frequency and its corresponding relative uncertainty depends on the trap geometry and is determined from numerical simulations [81]. This effect has also been experimentally tested to a relative precision of 5% during the proton measurement campaign [81] and remeasured to a relative precision of 3.2% reported in section 5.6. The cyclotron frequency shift due to the image charge effect is $65.8(33)$ ppt[3].

6.4.5 Lineshape systematic

A systematic effect also arises from the detection technique of the axial frequency as a result of the interaction of the ion with the axial detection system. Due to the complex impedance of the tank circuit, there is a phase shift in the voltage generated by the induced ion current. As the phase-shifted voltage acts back on the ion, the ion's eigenfrequency is shifted (frequency pulling). While this shift is null when the ion is in resonance with the tank circuit, it becomes sizeable for a slightly detuned ion. The effect is detailed in section 3.1.5. The theoretical lineshape model used for the dip fit includes this effect and nominally corrects for any detuning between ion and resonator (see section 3.1.7). The line shape model of a dip signal uses the resonance frequency ν_{res} and the quality factor Q of the tank circuit as input parameters. Therefore, it requires accurate values of these resonator parameters. Since these values are only known to a certain precision from dedicated fits to the thermal noise spectrum of the resonator, it causes uncertainty for the corrected axial frequency.

The extracted ν_{res} is sensitive to the number of data points included on either side of the center of the noise spectrum (the 'fit range'). Using a reasonable fit range, one can evaluate that the ν_{res} varied $\pm$ 3 Hz between runs during the measurement campaign contributing to the systematic error. As the axial frequency ν_z is dependent on $\Delta\nu_{\text{res}}$, it enters the free cyclotron frequency ν_c through the invariance theorem. Fig. 6.4 shows two exaggerated cases of incorrect ν_{res}. These fits are asymmetric, and thus the axial frequency obtained is inaccurate. The dependence of axial frequency extracted from the dip fit on the resonator

[3] To make a conservative estimate, the relative uncertainty of 5% is used.

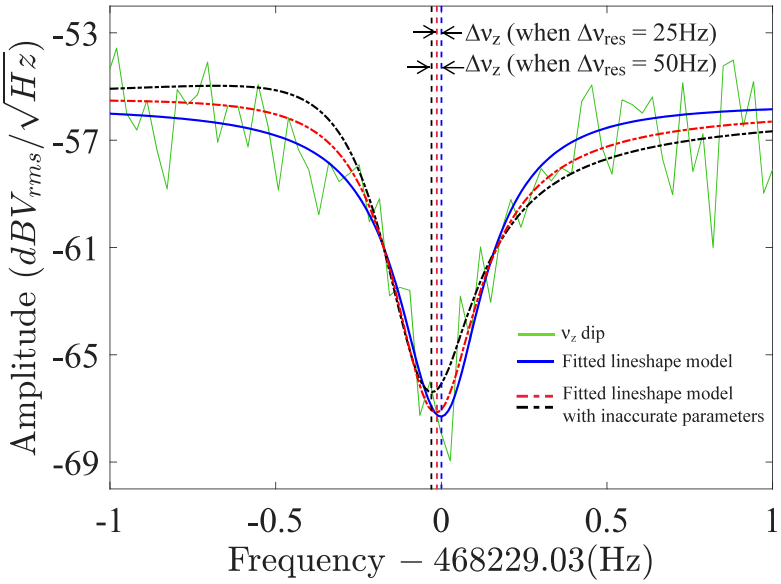

Figure 6.4. An axial dip spectrum of $^4He^{2+}$ [92]: The ion signal (green) enables the measurement of the axial frequency when in thermal equilibrium with the tank circuit. The tank circuit has a back action on the ion, slightly altering its frequency. The lineshape model (blue) nominally corrects this shift. To this end, the tank circuit's parameters must be precisely known. The black and red lines indicate the lineshape that results from a resonance frequency of the tank circuit shifted artificially by 50Hz and 25Hz, respectively. The resulting asymmetry of these fits results in systematically shifted axial frequency values.

frequency for $^4He^{2+}$ and $^{12}C^{6+}$ are $\sim$1 mHz Hz^{-1} and $\sim$2 mHz Hz^{-1} respectively. The resulting relative uncertainty in ν_c is 4.8×10^{-12} and 2.4×10^{-12}, for carbon and helium ions, respectively, when ν_+ is measured via PnA and axial frequency enters only through the invariance theorem. As the source of both uncertainties is common, we sum them linearly to give a conservative estimate of relative uncertainty of 7.1 ppt in the cyclotron frequency ratio. The Q of our resonator was relatively low during this work, $Q \approx 2300$. This indirectly contributes to the effect because the Q-value determines how accurately the resonator parameters can be extracted, including the ν_{res}. Some additional measurements were performed to find the influence of varactor voltage and the local oscillator frequency on the extracted resonator frequency. The varactor voltage was switched between $^4He^{2+}$ and $^{12}C^{6+}$ settings repeatedly, and after every switch, a resonator spectrum was recorded to check the repeatability and see if the resonance frequency in both settings remained constant. We also checked for drifts in the resonance frequency by recording multiple spectra after a varactor voltage change. No significant jitter or drift was found from the change of the varactor settings. Also, no dependency of the resonator frequency on the local oscillator frequency was found.

To cross-check the effect of dip lineshape, we also studied the axial frequency measurements during the mass measurement cycles. As we use the same trapping potential (U_r) for both ions, the mass ratio can also be extracted with low precision from the axial frequency

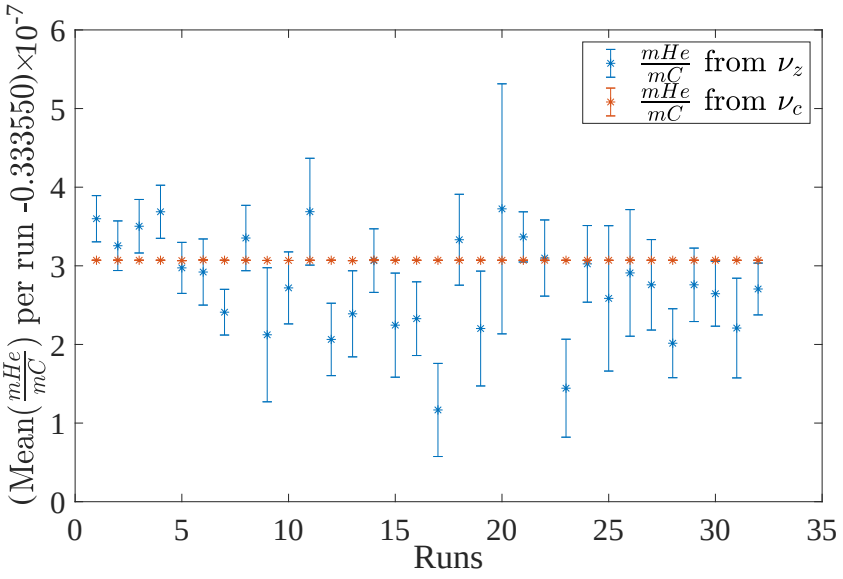

Figure 6.5. Comparison of mass ratios extracted from ν_z and ν_c for all runs. The weighted means are $\left(\frac{m(^4\mathrm{He}^{2+})}{m(^{12}\mathrm{C}^{6+})}\right)_{\nu_z} = 0.333\,550\,289(8)$ and $\left(\frac{m(^4\mathrm{He}^{2+})}{m(^{12}\mathrm{C}^{6+})}\right)_{\nu_c} = 0.333\,550\,307\,0626(19)$.

ratio, see Fig. 6.5. Using Eq. (2.10), we can derive:

$$R^z = \left(\frac{\nu_z(^{12}\mathrm{C}^{6+})}{\nu_z(^4\mathrm{He}^{2+})}\right)^2 = 3\frac{m(^4\mathrm{He}^{2+})}{m(^{12}\mathrm{C}^{6+})}. \tag{6.6}$$

The effect of dip lineshape can be studied by comparing this ratio with the mass ratio extracted from R^{CF}. In principle, these ratios must be equal, but lineshape-related issues would cause a discrepancy $R^{CF} \neq R^z$. The observed difference $R^{CF} - R^z = 1.8 \times 10^{-8}$ indicates a differential shift of the axial frequencies of ≤ 13 mHz, well in agreement with the estimated uncertainties due to ν_{res} and Q.

6.4.6 Magnetron frequency

The contribution of systematic shifts due to magnetron frequency is negligible. The magnetron frequency is not measured as often as the axial and modified cyclotron frequencies during the campaign. In fact, for each mass measurement cycle, the current magnetron frequency is calculated from the measured axial (ν_z) and modified cyclotron (ν_+) frequencies using the ideal Penning trap relation $\nu_-^{ideal} = \frac{\nu_z^2}{2\nu_+}$. Although in a real Penning trap, the magnetron frequency is subject to systematic shifts from trap imperfections such as tilt and ellipticity [67], the calculated value only deviates ≤ 600 mHz from the actual measured value. Since this shift is almost independent of q/m of the ions, the effect on the cyclotron frequency ratio is only of order $\sim 10^{-15}$ and is thus not considered in the systematic error budget.

Table 6.3. Summary of the systematic shifts and their uncertainties for the cyclotron frequency ratio [92]. R^{CF}_{stat} is the measured cyclotron frequency ratio (statistical result), and R^{CF}_{corr} is the cyclotron frequency ratio corrected for systematic shifts. All values presented in the table are relative. The shifts due to the nominally excited cyclotron radius are not included, as it is accounted for by the extrapolation (see section 6.3.1).

Effect	Rel. shift in ν_c ($\nu_c^{\text{real}} - \nu_c^{\text{noshift}}$ in ppt)		Rel. shift in R_{CF} (in ppt) $\left(\frac{R^{CF}_{\text{stat}} - R^{CF}_{\text{corr}}}{R^{CF}_{\text{stat}}}\right)$	Uncertainty (in ppt)
	He	C		
Image charge	-32.91	-98.67	65.76	3.29
Relativistic	-2.49	-0.72	-1.77	0.31
Magnetic inhomogeneity	-0.04	-0.01	-0.03	0.19
Electrostatic anharmonicity	0	0	0	0.13
Dip lineshape	0	0	0	7.11
Total	-35.44	-99.40	63.96	7.84

6.5 Helium-4 mass value

The final cyclotron frequency ratio with systematic and statistical uncertainties is:

$$R^{CF}_{\text{Final}} = 1.000\ 650\ 921\ 192\ 8(90)_{\text{stat}}(78)_{\text{sys}}(119)_{\text{tot}}. \tag{6.7}$$

The numbers in brackets denote statistical, systematic, and total uncertainty, respectively.

Using Eq (6.2) and the value of R^{CF}_{Final}, we can derive the mass of $^4\text{He}^{2+}$ with a total relative precision of 12 ppt:

$$m(^4\text{He}^{2+}) = 4.001\ 506\ 179\ 651(36)_{\text{stat}}(31)_{\text{sys}}(48)_{\text{tot}}\ \text{u}. \tag{6.8}$$

The mass of the atom can be derived by accounting for the mass of the two missing electrons [32] and the binding energies ($E_{b,i}$) [98] (summarized in table 6.1):

$$\begin{aligned} m(^4\text{He}) &= m(^4\text{He}^{2+}) + 2m_e - \sum_{i=1}^{2} \frac{E_{b,i}}{c^2}, \\ m(^4\text{He}) &= 4.002\ 603\ 254\ 653(36)_{\text{stat}}(31)_{\text{sys}}(48)_{\text{tot}}\ \text{u}. \end{aligned} \tag{6.9}$$

6.5.1 Comparison with other high-precision helium-4 mass values

The mass of ^{4}He has been measured before by several groups. Some of these are the group of Van Dyck at the University of Washington (UW) [37, 38, 39], the group of Günter Werth in Mainz [40], and SMILETRAP in Stockholm [41, 42]. The results of these groups show tension

of about 3σ (combined standard deviations [4]). Fig. 6.6a presents a comparison of the mass values from these experiments to the result of this work. The LIONTRAP result agrees with the SMILETRAP results within 1σ. In the SMILETRAP experiment, the helium mass value was obtained from the cyclotron frequency ratios of $^4He^{2+}$ and H_2^+. Thus, the ^{4}He mass values of SMILETRAP can be re-evaluated using the latest proton mass from CODATA [32]. The agreement between our mass value and the SMILETRAP mass value (re-evaluated) is still true. However, our result disagrees with the second-most precise ^{4}He mass measured at UW with a precision of 16 ppt. Our value is a factor of 1.3 more precise than the UW value but deviates from the same by 6.6 σ.

6.5.2 Deviation from literature value

The result from UW currently (2023) yields the accepted literature value by CODATA [32]. As previously stated, compared to the CODATA18 value, the ^{4}He mass reported in this work deviates notably (6.6 σ). The comparison is plotted in Fig. 6.6b. The literature value reported by the AME (Atomic Mass Evaluation) is identical to the one in CODATA18 but with an increased error bar [43]. For other light ion masses, an agreement was observed between the results from the FSU trap and LIONTRAP, as described in section 1.1.2. However, these values showed large inconsistencies compared to the results of UW. Therefore, to compensate for a possible error in the mass values from UW, in AME2020 [102], the 63 pu uncertainty for the mass of ^{4}He given in the previous editions of AME [103] has been increased to 158 pu. Still, our result deviates by 3.2 σ from the AME2020 value.

6.6 Constraints on the statistical uncertainty

The jitter on the cyclotron frequency ratio can originate from the ν_+ and ν_z measurements or from fluctuations of the magnetic or electrostatic fields between successive measurements. The total relative statistical precision achieved in the cyclotron frequency ratio measurement is 9×10^{-12}. Since the lineshape systematics limited us, an attempt to improve the statistical precision was not made during this measurement campaign. However, there are several constraints to reaching a low part-per-trillion in total statistical precision, which will be discussed in this section.

6.6.1 Phase and frequency jitter during PnA measurement

The statistical precision achieved per shot of the cyclotron frequency ratio measurement is related to the PnA measurements of ν_+ of both ions. The jitter of the measured phase is estimated as the standard deviation (std) of subsequently measured phase differences (diff)

[4] **All the 'σ' (standard deviation) values reported in this chapter are estimated from the combined uncertainty, i.e., $\sigma = |a-b|/\sqrt{\sigma_a^2 + \sigma_b^2}$, where a and b are two mass values and σ_a and σ_b are their respective uncertainties.**

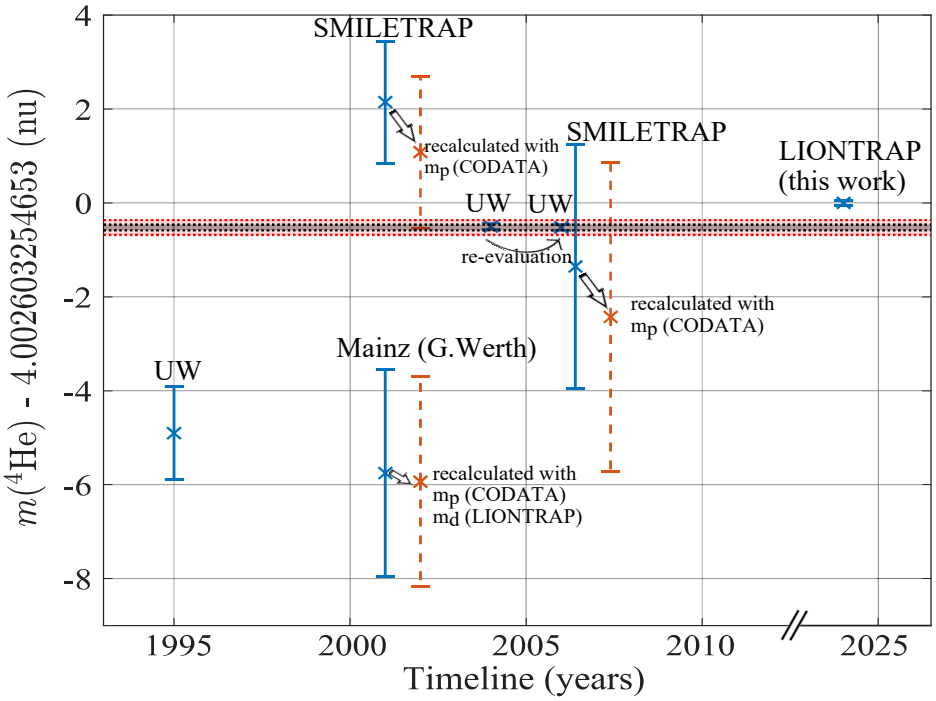

(a) Timeline of the most precise ^{4}He mass measurements

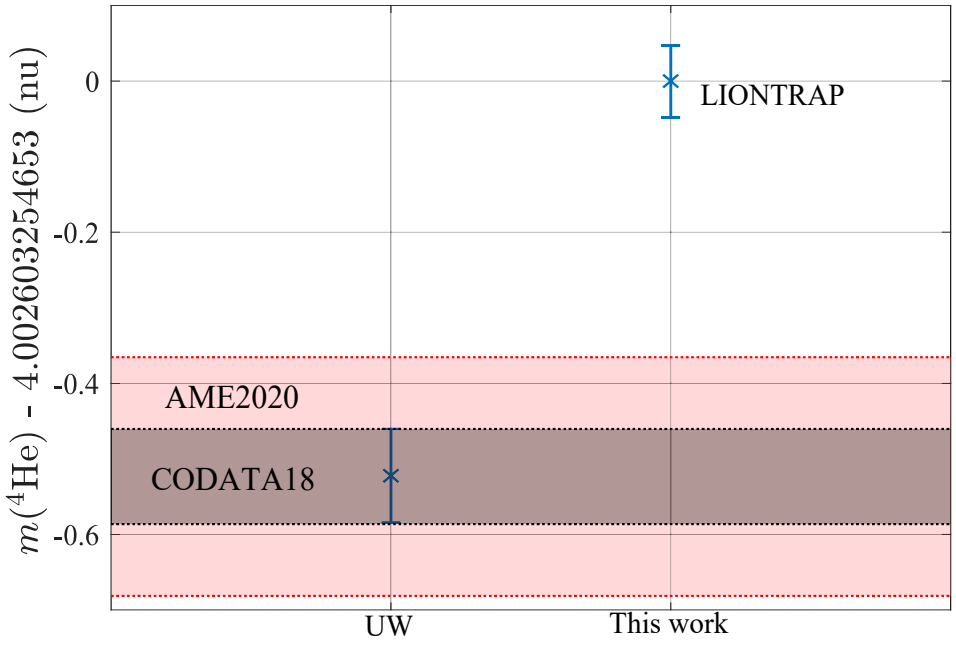

(b) Zoomed into the result of this work

Figure 6.6. High-precision ^{4}He mass values from different experiments [92]. In (a), ^{4}He mass measurements over the years are plotted as blue points. The red points (error bars: red dotted lines) indicate the mass of ^{4}He corrected for the most recent proton mass [32] and deuteron mass or both [22] in the cases where these were used as reference ion(s). The red shaded area indicates the AME2020 value, and the grey shaded region indicates the CODATA18 value. In (b), a zoom-in view of the result of this work, which deviates from the literature value, is shown. The CODATA18 value coincides with the latest UW result. The AME2020 is also given by the same measurement but with an increased error bar (see text).

divided by the square root of two ($\sqrt{2}$),

$$\delta\phi = \frac{\text{std}(\text{diff}(\phi_i, \phi_{i+1}))}{\sqrt{2}}, \tag{6.10}$$

where i and $i+1$ denote successive measurements.This jitter limits the achievable resolution on the ν_+.

$$\frac{\delta\nu_+}{\nu_+} = \frac{\delta\phi}{\phi} = \frac{\delta\phi}{360°\nu_+ T_{\text{evol}}}. \tag{6.11}$$

These jitters occur during different parts of the PnA measurement.

6.6.1.1 Jitter at start of PnA

At the beginning of the PnA pulse sequence, a dipolar excitation imprints a phase and excites the modified cyclotron mode of the ion. The ion, which was cooled via the axial tank circuit prior to the excitation, possesses a thermal distribution resulting in a phase distribution and leads to a phase jitter $\delta\phi_{\text{therm}}$ after the dipolar excitation. The phase jitter from imprinting a phase is lower if the excitation amplitude is much larger than the thermal amplitude. However, larger modified cyclotron energies lead to increased systematic shifts while measuring the ion's mass. Reducing the thermal amplitude by improving the cooling before the excitations would also help reduce this imprinting jitter.

6.6.1.2 Jitter during evolution time

Special relativity and field imperfections: The thermal distribution of the modified cyclotron mode results in different final energies of the excited particle. The energy-dependent shifts due to relativistic mass increase, magnetic inhomogeneity B_2, and electrostatic anharmonicity C_4, C_6 thus cause a frequency jitter. As the field imperfections are minimized in the PT, the jitter is dominated by relativistic effects. The phase jitter $\delta\phi_{\text{rel}}$ is linearly proportional to this frequency jitter times the T_{evol}. The $\delta\phi_{\text{rel}}$ is negligible for short evolution times.

Magnetic field stability: The magnetic field fluctuations cause a frequency jitter from shot to shot. The magnetic field instability leads to phase ambiguities and thus imposes an upper limit on the long T_{evol} that can be used. Further details on magnetic field stability can be found in section 6.6.2.

6.6.1.3 Jitter at detection

The jitter at the detection stage $\delta\phi_{\text{tech}}$ arises from the read-out of the phase. This jitter is purely technical and not dependent on the ion. During the phase detection from the peak of the axially excited ion signal, the limited SNR leads to this phase jitter. The amplitude of the second PnA pulse can be increased to reduce the jitter until affected by field imperfections. The doubly compensated highly harmonic trap allows us to perform larger axial excitations to minimize this jitter.

The measured phase jitter results from the combination of all the jitters mentioned earlier. In table 6.4, the measured phase jitter ($\delta\phi_{\text{meas}}$) is compared to the results of the simulation of the jitters for a few settings. The simulated jitter ($\delta\phi_{\text{tot}}$) is the squared sum of read-out jitter ($\delta\phi_{\text{tech}}$), thermal jitter ($\delta\phi_{\text{therm}}$), and the relativistic frequency jitter expressed as phase jitter ($\delta\phi_{\text{rel}}$).

Table 6.4. The measured phase jitter and SNR for single $^{12}C^{6+}$ and $^{4}He^{2+}$ ions at the smallest and largest modified cyclotron excited radius used in the measurement campaign are calculated for the short (red) and long (blue) T_{evol}. A comparison to simulated jitter is also presented. All phase jitters are given in degrees.

		Measurement			Simulation					
Ion	r_+^{exc}	SNR	$\delta\phi_{\text{meas}}$ at Tevol		$\delta\phi_{\text{tech}}$	$\delta\phi_{\text{therm}}$	$\delta\phi_{\text{rel}}$ at Tevol		$\delta\phi_{\text{tot}}$ at Tevol	
			100 ms	20 s			100 ms	20 s	100 ms	20 s
$^{12}C^{6+}$	10 µm	18.9	16.1	19.2	6.5	12.3	<0.1	1.1	13.9	14.0
	80 µm	18.8	7.1	14.7	6.6	1.5	<0.1	9.1	6.8	11.4
$^{4}He^{2+}$	10 µm	13.1	29.6	29.6	13.3	23.3	<0.1	2.1	26.7	26.8
	80 µm	12.1	13.9	26.5	15.5	2.6	≤0.1	15.7	15.7	22.2

- The uncertainties of $\delta\phi_{\text{rel}}$ and $\delta\phi_{\text{therm}}$ are temperature dependent (T = 1.7(3) K, see section 5.4), and the combined uncertainty of the phase jitters for carbon $\lesssim 2°$ and helium $\lesssim 4°$ for both 10 µm and 80 µm.
- The readout jitter is determined from the SNR of every cycle with similar settings and then averaged. The SNR to phase jitter relation is described in [63].
- The measured phase jitters are in reasonable agreement with the simulated jitters within the given uncertainties.
- The resolution of the modified cyclotron frequency measurement can be calculated from the measured phase jitters. The 6 short T_{evol}s and 5 long T_{evol}s[5] result in $\frac{\delta\nu_+}{\nu_+} \approx 5.2\times10^{-11}$ for carbon at 10 µm and $\frac{\delta\nu_+}{\nu_+} \approx 8.6\times10^{-11}$ for helium at 10 µm. The phase jitter at 10 µm is dominant, and most measurements are done with this amplitude, and thus, the resulting jitter of the cyclotron frequency ratio is 1×10^{-10}.

6.6.2 Magnetic field drifts

Frequency resolution remains unaffected by magnetic field fluctuations, as the mean of the magnetic field during the evolution time is acquired in a PnA measurement. Moreover, the fluctuations in the cyclotron frequency caused due to the stability of the magnet average out over several measurement cycles with randomized order of ions and thus do not cause a systematic shift. But with time, the magnetic field changes and cause a frequency jitter from shot to shot. The slow linear drifts of the magnetic field during the PnA cycles are suppressed

[5]The innermost PnA cycles are avoided in the final analysis to eliminate effects due to voltage drifts caused by transport. This is explained in section 6.6.3.

by considering the standard deviation of the difference of phases measured successively divided by $\sqrt{2}$ as given in Eq. (6.10).

The magnet in use was charged almost 26 years ago, and therefore, effects due to decay and fresh charging are negligible. However, the change in liquid helium and nitrogen levels in the magnet reservoirs can influence the magnetic field due to temperature fluctuations. The PnA measurements with long T_{evol} are more sensitive to these magnetic field drifts. One can try to estimate the phase jitter due to magnetic field jitter and thus the stability of the magnetic field during the high precision ν_+ measurement by either comparing the measured jitter and the jitter simulated from first principles or by comparing the phase jitter of long and short T_{evol}'s.

Comparing measured and simulated jitter: For the long evolution time, the modeled phase jitter $\delta\phi_{\text{tot}}^{20\text{s}}$ does not include the magnetic field jitter $\delta\phi_{\text{mag}}$ and is thus smaller than the measured phase jitter $\delta\phi_{\text{meas}}^{20\text{s}}$.

$$\begin{aligned}
\delta\phi_{\text{tot}}^{20\text{s}} &= \sqrt{\delta\phi_{\text{therm}}^2 + \delta\phi_{\text{rel}}^2 + \delta\phi_{\text{tech}}^2}, \\
\delta\phi_{\text{meas}}^{20\text{s}} &= \sqrt{\delta\phi_{\text{therm}}^2 + \delta\phi_{\text{rel}}^2 + \delta\phi_{\text{tech}}^2 + \delta\phi_{\text{mag}}^2}, \\
\therefore \delta\phi_{\text{mag}} &= \sqrt{\delta\phi_{\text{meas}}^{20\text{s}\,2} - \delta\phi_{\text{tot}}^{20\text{s}\,2}}.
\end{aligned} \tag{6.12}$$

The jitter estimated is the largest for helium at a modified cyclotron radius of $80\,\mu\text{m}$. From different settings and using Eq. (6.11) one can estimate a magnetic field jitter for both ions $\frac{\delta\nu_+}{\nu_+} \approx \frac{\delta B}{B} \lesssim 7 \times 10^{-11}$ throughout the measurement campaign.

Comparing jitter at long and short T_{evol}'s: The measured phase jitters at 100ms ($\delta\phi_{\text{meas}}^{100\text{ms}} = \sqrt{\delta\phi_{\text{therm}}^2 + \delta\phi_{\text{tech}}^2}$) are far less influenced by magnetic fluctuations, as well as relativistic jitter compared to measured phase jitters at 20s (Eq. (6.12)). The readout and thermal jitters are common to long and short evolution times. Therefore,

$$\therefore \delta\phi_{\text{mag}} = \sqrt{\delta\phi_{\text{meas}}^{20\text{s}\,2} - \delta\phi_{\text{meas}}^{100\text{ms}\,2} - \delta\phi_{\text{rel}}^{20\text{s}\,2}}, \tag{6.13}$$

which results in $\frac{\delta B}{B} \lesssim 7 \times 10^{-11}$.

The drift in ν_+ frequency between cycles is $\approx \pm\, 9\,\text{mHz}$. One of the runs consisted of measurements where carbon was always measured first after transport in the measurement cycles[6]. This run was chosen to evaluate the drift between cycles. Both ions always faced a transport before the cyclotron frequency measurement, and therefore the evaluated ν_+ drift would include any magnetic field fluctuations due to transport as well. The magnetic field change due to transport occurs if the change in potential leads to an equilibrium position change when a residual magnetic field gradient is present. However, in our experiment, this

[6]This was the first and the only measurement in the campaign before randomizing the order of the ion.

is highly suppressed. Moreover, the interesting drift is between the two ions' high precision ν_+ measurements, and since the measurement time between the two high precision ν_+ measurements is one-quarter of the whole measurement time, the drift would also be suppressed by the same factor [30], leading to a magnetic field jitter $\frac{\delta B}{B} \lesssim 7.5 \times 10^{-11}$, which translates to the jitter in cyclotron frequency ratio.

6.6.3 Voltage drifts

The voltage drifts or fluctuations occur during the PnA measurement and throughout the campaign. During the measurement campaign, an axial frequency jitter ${}^{\delta\nu_z}/_{\nu_z} \approx 2 \times 10^{-7}$ occurs, leading to jitter of 5×10^{-11} in ν_c. This corresponds to a relative voltage stability of our voltage source ${}^{\delta U}/_{U} \leq 4 \times 10^{-7}$ between two consecutive axial frequency measurements of an ion in a mass measurement run separated by about an hour, including transports. This value is similar for both ions. The jitter in cyclotron frequency ratio is thus 7.1×10^{-11}.

In our mass measurement cycle, after the ion I is chosen and transported into the PT, it is cooled. A double-dip measurement of ν_+ followed by a dip measurement of ν_z is carried out prior to the PnA cycles. For ion II, the case is reversed, and the PnA cycles occur first so as to measure the ν_+ of ion I and II as closely as possible. It is followed by the measurement of a dip and a double-dip measurement, respectively. Different voltages are applied on the trap electrodes during transport, and the precooling after transport also acts as a settling time for the voltages. However, the first long T_{evol} measurement of the second measured ion in the cycle is not used during the analysis to avoid voltage drifts after transport. For the simplicity of the analysis, the last long T_{evol} PnA cycle of the first ion is also removed. Thus the most inner PnA cycles in a measurement cycle are eliminated for the final analysis. Thus, the voltage drifts due to transport did not play a significant role in statistical uncertainty. However, the effect can be estimated as follows.

The ν_z measurement (dip) is always closer to the PnA cycles than the ν_+ measurement (double-dip). Once the ion for measurement is in the PT, the double-dip is measured after $\sim$1 min. The dip measurement takes place $\sim$3.5 min after that, and the PnA cycles with long evolution time, which determine the ν_+ with the highest precision, start almost 14 min after the dip measurement. During the measurement cycle, the first measured ion is chosen randomly, and depending on this, there might or might not be a transport involved, and the second ion always sees a transport. Now when the transport occurs, there are voltage drifts possible and thus drifts in the ν_z. These drifts take time in the minutes-scale to settle, and this would mean that if a transport occurred, the trapping voltage during the double-dip measurement is incorrect and less incorrect during the dip measurement as the drift slowly settles down by then and during PnA cycles there is no more voltage drift due to transport. Let the shift in ν_z during the double-dip measurement be $\Delta\nu_{z,\text{DD}}$ and during the dip measurement be $\Delta\nu_{z,\text{Dip}}$. The dip and double-dips are fitted after the measurement, and the fitted frequencies serve as inputs for the PnA measurements. Therefore, the $\Delta\nu_{z,\text{Dip}}$ is

directly related to the $\nu_{+,\mathrm{PnA}}$ whereas $\Delta\nu_{z,\mathrm{DD}}$ is directly related to $\nu_{+,\mathrm{DD}}$. Therefore if one compares the $\nu_{+,\mathrm{DD}} - \nu_{+,\mathrm{PnA}}$ with and without transport before measurement, the voltage drift and thus axial frequency jitter due to the same can be estimated. Hence, $|\Delta\nu_{z,\mathrm{Dip}}| \leq |\Delta\nu_{z,\mathrm{DD}} - \Delta\nu_{z,\mathrm{Dip}}| \leq |25\,\mathrm{mHz}|$ indicates that the voltage drift causes 1.4×10^{-11} relative uncertainty in ν_c per shot. However, this has to be averaged over both the ion pairs for the final frequency ratio as the transports are in opposite directions for the two ion pairs, resulting in relative uncertainty of the cyclotron frequency ratio of 2×10^{-12}.

6.7 Summary of the limitations of mass measurement and possible improvements

The statistical uncertainty of the R^{CF} per measurement cycle during this campaign was 1.4×10^{-10}, which is evaluated as the average of the standard deviations of each run for all measured R^{CF}'s (see section 6.3). The main statistical limitations discussed in the previous section were magnetic field drift, phase and frequency jitters during PnA, and voltage drifts (axial frequency stability). Although the magnetic field fluctuates, this does not impact the frequency resolution as the phase measurement during PnA gives the mean of the magnetic field during the evolution time with high precision (provided there is no readout jitter). However, this is only true for a single measurement. For the measurement at a different time, the field will have changed to some extent. Consequently, there is a frequency jitter and hence R^{CF} jitter from shot to shot, which can only be improved by better magnetic field stability or simultaneous cyclotron frequency measurements. To improve the resolution of the PnA to reach better statistical precision, the jitters dominating the measurement at long evolution times should be minimized. The long evolution times are dominated by frequency jitter due to special relativity followed by phase imprinting jitter[7]. The temperature of the ion should be further reduced to achieve better phase stability by reducing the effects of special relativity and the phase imprinting jitter. In other words, a lower ion temperature helps in two ways. Firstly, when all other parameters remain constant, it helps to excite the ion to a similar radius from shot to shot and thus, resulting in a lower imprinting jitter. Secondly, if there are no other constraints, the excitation radius can be reduced until limited by imprinting jitter and then benefit from the lower relativistic shift. The voltage drifts must also be further minimized to improve the statistical precision. This can be achieved by adopting a more stable voltage source for trap voltages, which is already set up for the next measurement campaign. Using an independent voltage source for performing transports could help; however, dielectric soakage of the capacitors in the circuits could pose a restriction and introduce voltage drifts. We are currently assessing different commercially available capacitors for their cryogenic soakage behavior to mitigate this limitation. These electric field drifts can also be suppressed to a large extent when the cyclotron frequencies of the ions are

[7] This is true for small cyclotron mode amplitudes.

measured simultaneously, such as in the two-ion-balance method (see section 6.7.1).

The dominant systematic shift in this measurement campaign was due to the dip lineshape. The remaining sources of systematic uncertainties at LIONTRAP do not pose a restriction on achieving a mass measurement with a relative precision below 5 parts per trillion (ppt). The next campaign will use an improved detection system with a better quality factor. With this, the accuracy with which the resonator parameters can be extracted will be improved. To further reduce the systematic uncertainty due to the dip lineshape, axial phase-sensitive measurements are a way to go. There one would extract the axial frequency from the phase information of the excited ion, similar to the PnA technique for ν_+ measurements. This way, the dependence on the lineshape model is completely avoided. Another method to reduce the systematic uncertainty due to lineshape is to use the axial frequency of one ion to calculate the axial frequency and, consequently, the cyclotron frequency of the second ion, as they share the same trap voltage configuration. However, in the shuttling method, the measurement of the frequencies occurs at different times, making it sensitive to voltage drifts and parasitic voltage offsets, which will have to be investigated carefully. In a simultaneous measurement, such offsets and drifts are naturally avoided.

The magnetic and electric field instabilities limiting the statistical precision and the limiting systematic shift caused by the dip lineshape are best resolved by implementing a two-ion-balance method, where the ions are measured simultaneously in the same trap. Here, if the relativistic jitter and the systematics due to Coulomb interactions are under control, the statistical precision per shot can be reduced to the low 10^{-11} range, about an order of magnitude better than possible in the shuttling method (in the LIONTRAP magnet). At LIONTRAP, the first successful test for deploying this technique was made and is presented in section 6.7.1. The succeeding sections also elaborate on how the simultaneous measurement techniques address and mitigate the limitations discussed above.

6.7.1 Test of two-ion-balance method

As mentioned before, simultaneous measurement of ions in one trap is highly favorable in reducing the influence of magnetic and electric field instability. The two-ion-balance method discussed here is based on the work of S. Rainville and J. Thompson at MIT in the group of David Pritchard. The method was originally proposed by Eric Cornell in [104] and has been recently re-implemented at FSU [4] and ALPHATRAP [105]. The detailed derivations of the theory and description of the techniques addressed briefly in this section can be found in [65, 106, 107]. Here, two ions of interest are stored and measured together in a single trap. The magnetron modes of the ions can be easily coupled due to the q/m independence of the magnetron frequency in the first order. Therefore, the magnetron frequencies are almost degenerate for ions with similar charge and mass. Then, for typical radii, the Coulomb force causes strong coupling of the magnetron modes of both ions. However, the axial and modified cyclotron modes remain independent but with frequency shifts that depend on the

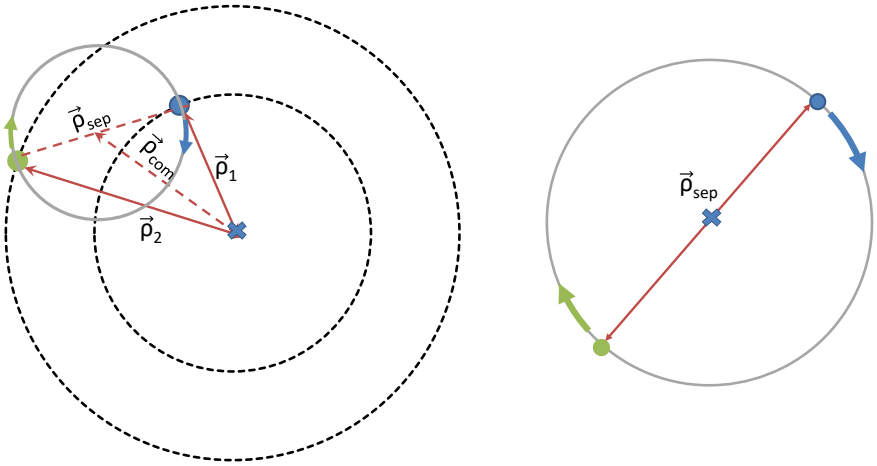

Figure 6.7. Magnetron mode dynamics of two ions. The picture on the left shows two ions parked with a non-zero common mode, resulting in each ion moving in and out of the center of the trap. The grey circle depicts the coupled magnetron mode, and the dotted black circle depicts the original individual magnetron modes. The ideal configuration for making cyclotron frequency ratio measurement at $\rho_{\text{com}} = 0$ is shown on the right side.

distance between the ions. Thus, the relative orbit of the ions has to be suitably defined to avoid excessive shifts in the cyclotron frequency ratio. Hence, the ions are usually arranged on the opposite sides of a magnetron orbit with the diameter in the order of a millimeter. This separation is large enough to avoid significant ion-ion interactions yet sufficiently small to keep the effect of magnetic inhomogeneity under control.

The Coulomb interaction between the ions causes the coupled magnetron mode to mix into two collective modes, common mode and separation mode. The common mode radius ρ_{com} is the radius of the center of mass motion of the coupled ions orbiting the electrostatic center of the trap, and ρ_{sep} is the separation distance between the ions (see Fig.6.7). For similar masses, these amplitudes are approximately constant in time, with a residual modulation that depends on the mass mismatch. The separation mode results from $\vec{E} \times \vec{B}$ drift of the ions about the center of mass due to their Coulomb interaction. If $\vec{\rho_0}$ and $\vec{\rho_1}$ are vectors in the radial plane from the center of the trap to the positions of the ions, then $\vec{\rho_{\text{com}}} = (\vec{\rho_1} + \vec{\rho_0})/2$ and $\vec{\rho_{\text{sep}}} = \vec{\rho_1} - \vec{\rho_0}$ (given $m_0 > m_1$).

If $\rho_{\text{com}} = 0$, the ions possess only ρ_{sep} and will be configured on opposite sides of the same magnetron orbit, such that the center of mass is at the center of the trap as shown in Fig. 6.7 (right). This way, the ions are exposed to almost the same fields on average (for time scales $< \frac{1}{\nu_-}$) and thus form the ideal configuration to measure cyclotron frequencies. The ions will periodically vary their individual magnetron amplitudes if $\rho_{\text{com}} \neq 0$. This slow modulation happens in the time scales of the beat frequency

$$\Omega_m = \frac{q}{2\pi\epsilon_0 B {\rho_{\text{sep}}}^3}, \tag{6.14}$$

where ϵ_0 is the electric constant. For example, if $\rho_{\text{com}} \approx \rho_{\text{sep}}/2$, the ions move in and

out of the center of the trap as shown in Fig. 6.7 (left). Although the ion is not in the ideal configuration when the common mode is not nulled, the swapping ensures that the mismatch of the magnetron radii is averaged to zero, for similar masses.

6.7.1.1 Measuring and controlling the magnetron motion

Measuring and manipulating the two collective modes is very important to bring the ions into the required configuration for measurement and have control over the systematics.
The separation distance can be obtained by observing each ion's axial frequency shift compared to their single ion frequency at the same voltage (refer to section 5.4 in [65]). A numerical simulation result of the axial frequency shift as a function of the separation distance is plotted in Fig. 6.8. A very small separation distance leads to a strong Coulomb interaction and deterioration in the quality of the ion signals, whereas a large separation distance leads to significant systematic errors as they get more exposed to field imperfections.

As the ion motions are not at the center of the trap, they are sensitive to magnetic field inhomogeneities and electrostatic anharmonicities. Therefore, artificially generated small imperfections which cause frequency shifts depending on the magnetron radius can be utilized to control and determine the modes. To park the ion in the desired magnetron orbit, a coupling method has been developed at MIT. It utilizes the fact that the axial frequency shift depends on the magnetron radius in an anharmonic trap. When $\rho_{\text{com}} \neq 0$, the magnetron radius modulation causes the axial frequency to modulate at the same beat frequency. By off resonantly exciting the axial motions of the ion in the presence of such an anharmonicity, the energy conservation is violated, but the canonical angular momentum is still con-

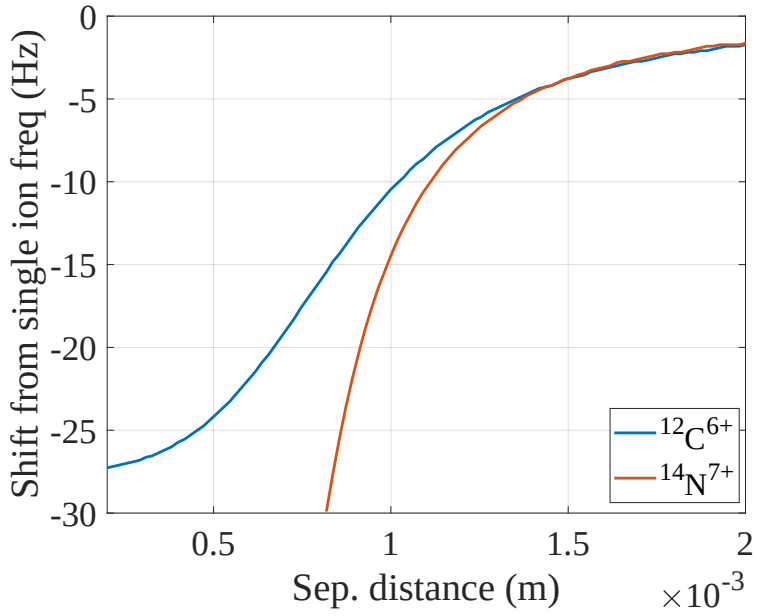

Figure 6.8. Simulated results of the axial frequency shifts for carbon and nitrogen ions as a function of the separation distance.

served [104, 106]. Thus, the total energy in the coupled magnetron modes can be changed, and the angular momentum can be redistributed between the two collective modes. I will address this method as 'MIT coupling' hereafter. To control the direction of momentum transfer between the common mode and separation, the value of introduced C_4 can be changed and the drive frequency (either above or below resonance frequency) can be adjusted.

To increase the separation mode, angular momentum can be injected into the common mode with a resonant magnetron drive, and then the MIT coupling can be applied to transfer the angular momentum from the common mode to the separation mode. To reduce the separation mode, sideband drives can be applied to each ion at a frequency of $\omega_{\text{rf}} = \omega_z + \omega_-$, where ω_z represents the damped axial mode frequency and ω_- corresponds to the magnetron frequency of the respective ion. In doing so, angular momentum is removed from the separation mode. Such a sideband drive will be referred to as a 'cooling sideband drive' hereafter. However, such cooling drives are not straightforward because the response of the ions depends on the ratio of the collective mode radii.

After performing the MIT coupling and increasing the separation mode to the maximum (possible), until no more change can be observed, the residual common mode radius can be measured by reintroducing the anharmonicity as the axial frequency shift can be related to the collective mode amplitudes [107] as:

$$\frac{\Delta\omega_z}{\omega_z} \sim \frac{-3C_4}{2d^2}(\rho_{\text{com}}^2 + \rho_{\text{sep}}^2/4). \tag{6.15}$$

6.7.1.2 Simultaneous cyclotron frequency measurement: Dual PnA

After positioning the ions on a shared magnetron orbit, we can employ the PnA technique to simultaneously measure their cyclotron frequencies. The PnA technique has been explained in section 3.3 and [85]. As a reminder, this technique involves a cyclotron mode excitation to define a phase that accumulates over an evolution time T_{evol} and is read out by transferring the phase information from the modified cyclotron mode to the axial mode with a coupling pulse that parametrically amplifies both modes. The phase information for both ions is then extracted from the FFT bins corresponding to the axial frequencies of the two ions.

In the alternating measurement technique (section 6.2), the upper limit of the T_{evol} that can be used in a PnA measurement is usually limited by the 2π jumps of the phase caused due to the magnetic field fluctuations. However, in a dual PnA measurement, the ions trapped together on a well-defined magnetron orbit experience the same variations in the magnetic field and fluctuations or drift in the electric field (trapping voltage) during T_{evol}. Thus, the phases remain well correlated with each other and the cyclotron frequency ratio can be determined with high precision [106, 107]. If $\Delta\phi_{\text{diff}}$ is the jitter of the measured phase difference in degrees and $\bar{\nu}_+$ is the average modified cyclotron frequency, the relative uncertainty on the cyclotron frequency ratio and, consequently, the uncertainty on mass ratio with a single

measurement can be estimated as

$$\frac{\Delta R}{R} \simeq \frac{\Delta\phi_{\text{diff}}}{360^{\circ} T_{\text{evol}} \bar{\nu}_{+}}. \tag{6.16}$$

6.7.1.3 Test measurement

In order to overcome the present limitations in the mass measurements at LIONTRAP (see section 6.7), the above-mentioned simultaneous measurement can be employed, and an attempt was made to implement its basic principles. As the first steps, two ions were mixed in the magnetron mode, the MIT coupling was carried out to park the ions on opposite sides of the magnetron orbit, and a simultaneous PnA measurement was performed on both ions. The resulting phase jitters for different evolution times were measured as proof of principle.

Firstly, single $^{12}C^{6+}$ and $^{14}N^{7+}$ ions were produced[8]. The $^{12}C^{6+}$ was stored in the PT, and $^{14}N^{7+}$ was stored in ST-II. The magnetron mode of the ion in the PT was then excited to a large radius ($\rho_{\text{m}} \approx 600\,\mu\text{m}$) and combined with $^{14}N^{7+}$ in ST-II, and the combined ions were transported back to the PT for detection and measurement. However, during the transport in the mixing process, the defined magnetron amplitudes tend to change due to changes in effective potential. Once the two ions are in the PT, they can be thermalized with the axial detection system. If the ρ_{sep} is large enough that the Coulomb interaction is minimum, as expected from the initial magnetron mode excitation, the ions can be detected as two separate dips, as seen in Fig. 6.9a, with minimum deviation from their nominal single ion frequencies observed at identical voltages. If the two ions are very close, i.e., if ρ_{sep} is too narrow, the axial frequency shifts are large, resulting in a single smeared-out dip as seen in Fig. 6.9b. The

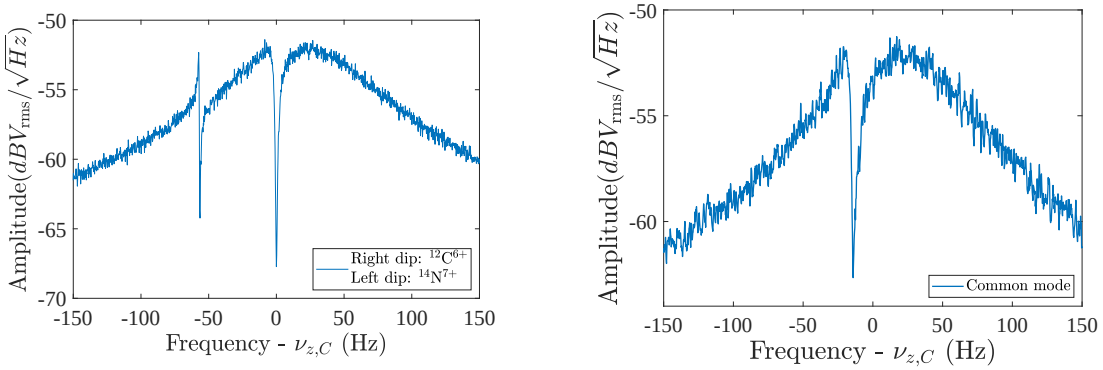

(a) $\rho_{\text{com}} \approx 0$ **(b)** $\rho_{\text{com}} \gg 0$

Figure 6.9. (a) shows the detected signal of two ions with a separation distance large enough such that the ions go around the trap center on almost the same magnetron orbit (b) shows a detected signal when the separation distance between the ions is small, resulting in a smeared-out single dip at an intermediate frequency.

[8]The $^{12}C^{6+}$ and $^{14}N^{7+}$ ions were chosen to perform the tests because they are more convenient to work with due to their larger dip widths compared to lighter ions. These ions are a good q/m doublet but not a good mass doublet. $^{16}O^{8+}$ was also used for tests.

second dip, corresponding to the axial out-of-phase motion, is too small and too far-shifted to be detected. Ideally, after the combination of the two ions, we expect $\rho_{\text{sep}} = 2\rho_{\text{com}} = \rho_{\text{m}}$. The actual ρ_{sep} can be determined from the shifts in the axial frequencies of the ions from their single ion frequency, see Fig. 6.8. During our attempts to combine two ions on three occasions, twice the separation distance was too large and once too small, indicating that our mixing process was not optimized. When ρ_{sep} was too large, we started with a cooling sideband drive (see section 6.7.1.1) a few Hz above the resonant sideband frequency with an amplitude of around 5 mVpp. When the separation distance was too small, a resonant magnetron excitation nominally to $380\,\mu$m was applied first to inject angular momentum into the common mode. Depending on the remaining collective mode amplitudes, the MIT coupling was performed to reach $\rho_{\text{com}} = 0$ and $\rho_{\text{sep}} \approx 1\,$mm. For the coupling, an anharmonicity of $C_4 \approx -1 \times 10^{-3}$ and an axial excitation drive $10\,$Hz below the dip frequency with an amplitude of 10 -100 mVpp with a 60 dB attenuation was applied. These settings gave the best coupling results but were not necessarily optimized. The coupling process had to be repeated several times with different anharmonicity and excitation settings until the required configuration was reached. However, it turns out that a sudden change of the potential to introduce C_4 causes a random change in angular momentum distribution between common and separation modes. Ramping the voltages slowly improves the situation. Due to the characteristics of our voltage source, changing the harmonicity adiabatically is not trivial. So, some hardware changes using relays and another bias supply, similar as shown in Fig. 5.10,[9] was implemented to adiabatically introduce C_4.

Fig. 6.9a shows an example of a detected signal of $^{12}C^{6+}$ and $^{14}N^{7+}$ ions coupled in a magnetron orbit after applying the MIT coupling. This indicates a $\rho_{\text{sep}} \approx 1\,$mm which is deduced from a $-9.8\,$Hz and $-15.9\,$Hz frequency shift of the right and the left dip, respectively, with respect to their single cold ion axial frequency. The unperturbed frequencies of the two species are separated by $50.3\,$Hz, and their dips in the coupled mode are separated by $56.7\,$Hz with $^{12}C^{6+}$ having the higher frequency. From the axial frequency shift caused by detuning the trap (at $\rho_{\text{sep,max}}$), $\rho_{\text{com}} < 200\,\mu$m was deduced. The mass mismatch between $^{12}C^{6+}$ and $^{14}N^{7+}$ causes significant modulation of ρ_{com}, resulting in $\rho_{\text{com,min}} > 0$.

In this magnetron orbit configuration, the coupled ions are separated enough to have minimum interaction, and we performed a PnA measurement on each ion simultaneously (dual PnA). With the initial dipolar pulse to imprint a phase, the modified cyclotron mode radii of the $^{14}N^{7+}$ and $^{12}C^{6+}$ ions were excited to $28\,\mu$m and $21\,\mu$m, respectively[10]. Two dual-channel function generators $80\,$MHz Agilent 33600A and $30\,$MHz Agilent 33552A were used to perform PnA on $^{14}N^{7+}$ and $^{12}C^{6+}$ ions, respectively. An example of a Fourier-transformed spectrum of the resultant axial signals is shown in Fig.6.10b. The phase information is extracted

[9] The $1\,\mu$F capacitor was replaced with a $10\,\mu$F capacitor. This way, the switching of the relays is buffered with a time constant of $\sim$1 s.

[10] Although the excitation strength used for both the ions were (in Vpp*t) the same, due to the lower sampling rate of one of the AWG's, the corresponding amplitude is a bit smaller.

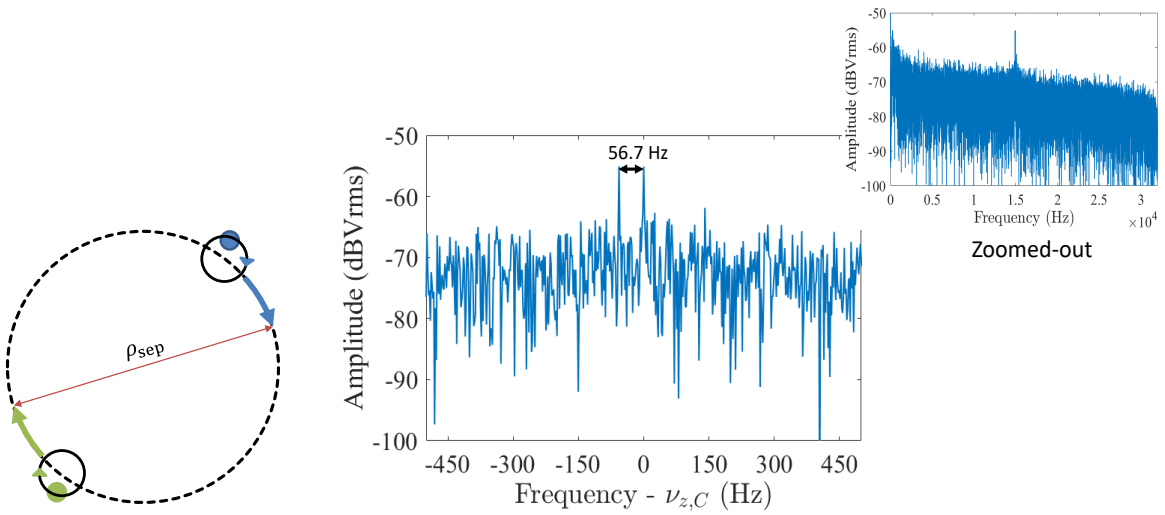

(a) Application of dipolar pulse

(b) FFT signal after PnA pulses

Figure 6.10. (a) shows the superposition of cyclotron orbits on the coupled magnetron mode with minimal common mode and the separation mode close to a millimeter. (b) shows the FFT signal of $^{14}N^{7+}$ and $^{12}C^{6+}$ ions after the phase-sensitive pulse routine has been applied. The ion signals are 56.7 Hz apart, as observed in their thermalized signal.

from such FFT spectra. The findings from the dual PnA measurements are as follows:

- The total phases accumulated by individual ions are random (with 2π jumps) after some tens of seconds, but phases of both ions are well correlated and vary in the same manner even for large T_{evol} (100's of seconds). See Fig. 6.11.

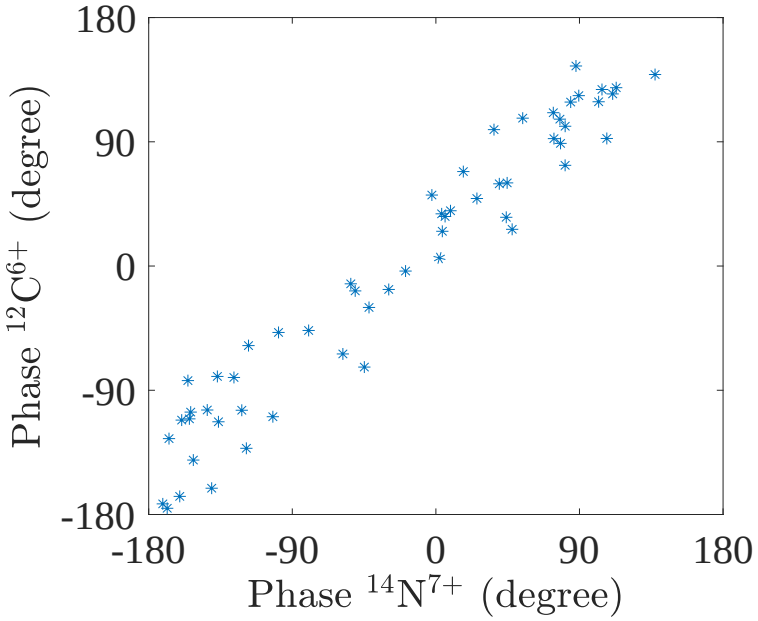

Figure 6.11. The measured phase of nitrogen ion vs the phase of carbon ion. This raw data is recorded after several PnA measurements with T_{evol} = 98 s.

- The individual phase jitter of the ions is higher compared to what one can achieve with single ions, possibly due to the two-ion interaction[11], but the jitter in the phase difference is less than $50°$ for times as long as $250\,\mathrm{s}$.

The standard deviation (std) of individual phases, SNR of the peak signals, and the std of the phase differences are tabulated in table 6.5. The measured phase differences for different T_{evol}'s are shown in Fig. 6.12. Due to fluctuations in the magnetic field, the precise total phase accumulated by an individual ion over a few minutes becomes random. However, we can consider T_{evol} of several minutes and still unambiguously unwrap the phase difference. With the longest $T_{\mathrm{evol}} = 250\,\mathrm{s}$ a cyclotron frequency ratio Eq. (6.16) with 3×10^{-12} relative precision within 3.2 h (40 PnA cycles) was possible. Moreover, the uncertainty in the cyclotron frequency ratio is mostly defined by the precision of the cyclotron frequency difference obtained from the phase difference, and the mode frequencies of the individual ions only need to be known to $< 1 \times 10^{-9}$ relative precision, reducing the influence of the magnetic and electric field stability [106]. One of the biggest advantages of the two-ion balance method is that the shifts due to lineshape systematics can be avoided to a large extent because the axial frequency of one ion can be used to calculate the frequency of the other, and as the ions are measured simultaneously drifts and fluctuations due to the voltage stability completely drop out.

From the results of this test measurement, it is clear that a significant improvement in precision can be achieved by using the two-ion-balance method compared to the shuttling method. This test is only the tip of the iceberg; considerable efforts need to be made to analyze and understand the ion-balance measurement system at LIONTRAP. On that note, it is valid to point out that the systematics arising from the field instabilities is lower if the measured ions have similar masses such as $\Delta m/m \leq 10^{-3}$ due to common mode rejection. However, if the masses are too close, individually addressing the axial and modified cyclotron motion of the two ions, which are also too close, gets complicated. Moreover, the Coulomb interaction results in the resonant coupling of the cyclotron motions leading to significant frequency shifts.

Table 6.5. Results of PnA measurement on the magnetron mode coupled $^{14}N^{7+}$ and $^{12}C^{6+}$.

T_{evol}	No. of cycles	std(ϕ_C)	std(ϕ_N)	SNR$_C$	SNR$_N$	std(ϕ_C-ϕ_N)
10 ms	10	21.3	10.4	12.2	19.3	22.1
20 s	20	32.5	32.9	15.1	18.9	18.6
98 s	60	68.2	71.3	14.7	18.8	25.8
130 s	26	66.8	63	14.6	17.0	31.4
250 s	40	68	64.2	15.3	15.0	49.1

[11] The jitter due to the ion-ion interaction is probably because one ion causes a significant $C_{4,\mathrm{eff}}$ on the other ion. Also, after each cyclotron excitation, the magnetron orbit alters, causing a fluctuation in axial frequency.

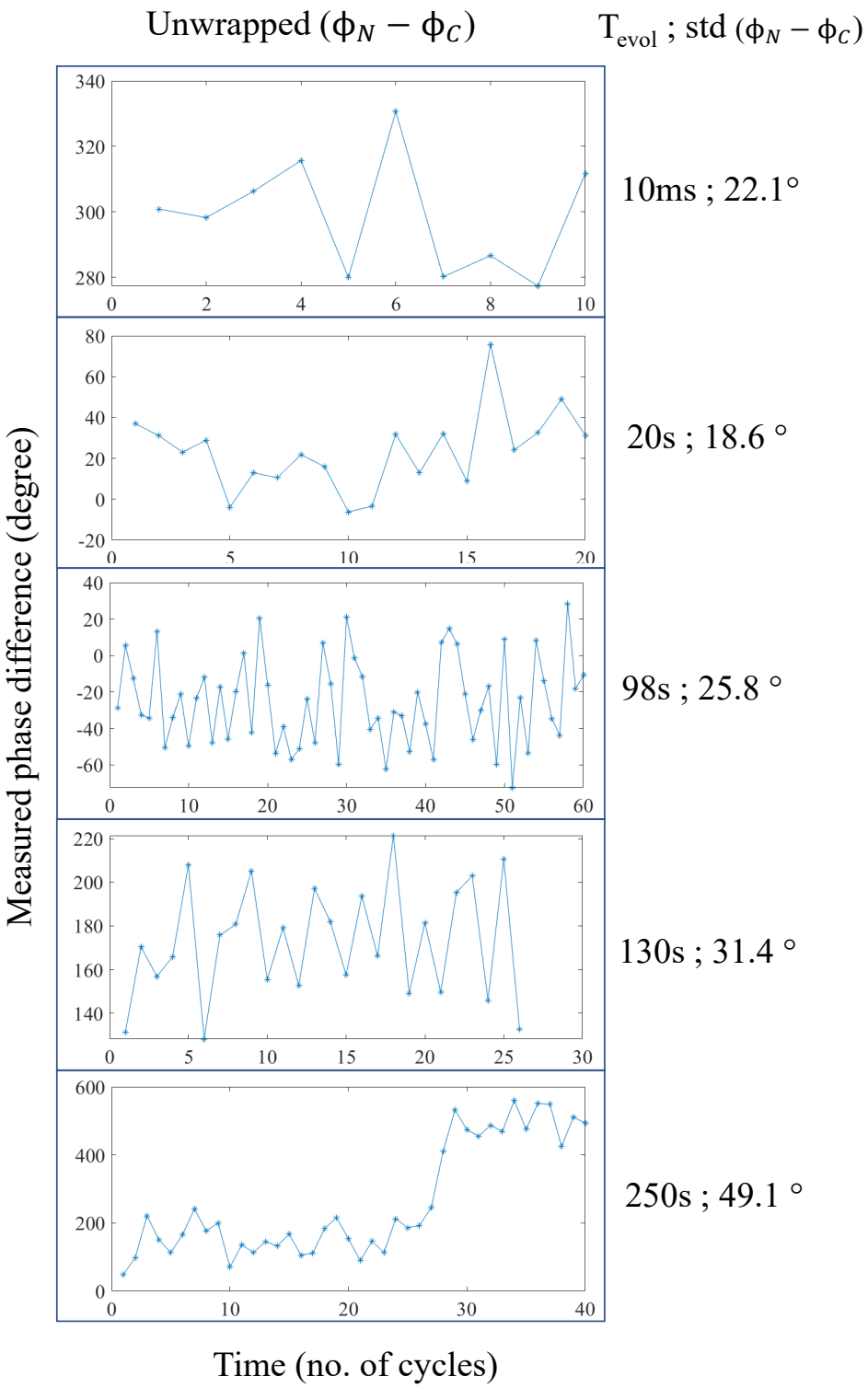

Figure 6.12. The measured phase difference (unwrapped) accumulated during different T_{evol} as a function of the number of PnA cycles. The jitter of the difference in phase is also noted against each data set.

6.8 Upcoming mass measurement at LIONTRAP

The inconsistencies observed in the light ion mass values strengthen our motivation to re-measure the mass of ^{3}He with reference to ^{12}C [17] as an attempt to resolve the light ion

mass puzzle (see section 1.1.1). This is the only link in the puzzle that has not yet been re-measured. In principle, there are two suitable measurement techniques, either the shuttling method discussed in section 6.2 or the ion-balance method discussed in section 6.7.1. The latter technique is promising for better statistical precision due to the cancellation of magnetic field fluctuations for the two simultaneously measured ions. However, as we plan to measure the mass of ^{3}He using ^{12}C as the reference ion, the significant mass mismatch, in this case, would lead to significant systematics when using the two-ion-balance technique, which still needs to be analyzed. In our experiment, HD^{+} would be the most convenient candidate to form a balance with ^{3}He, but this does not contribute to the missing link in the light ion mass puzzle. Further potential improvements to achieve a better relative precision of the ^{3}He mass have already been discussed in section 6.7. To perform the ^{3}He mass measurement, a source of gaseous ^{3}He atoms is essential. Such a source for gaseous atoms was developed during this work (see section 4.3). In the following section, a slight modification in the design of the source is presented, aimed at rectifying a technical error that occurred during the campaign. Additionally, the section provides detailed insights into the development of an alternative method for producing ^{3}He atoms.

6.8.1 Upgrades for the helium-3 mass campaign

6.8.1.1 Modification of the source for gaseous atoms

As mentioned in section 4.3, we could not produce ^{3}He ions using the source during this campaign for which it was initially planned. By design (see section 4.3.1), a wire runs through the titanium piercing head, which is attached to heating pads on a PCB via low-temperature solder. On heating of the low-temperature solder, the spring-loaded piercing head is supposed to be released, but we learned during the thermal cycle of the experiment after the ^{4}He mass campaign that this process failed. Only one side of this wire got entirely disconnected, and the other remained intact, holding back the piercing head. The main reason for this could be that only a single heating resistor was attached to one side of the wire, and it was expected that the solder on the other side would melt due to the heat conduction

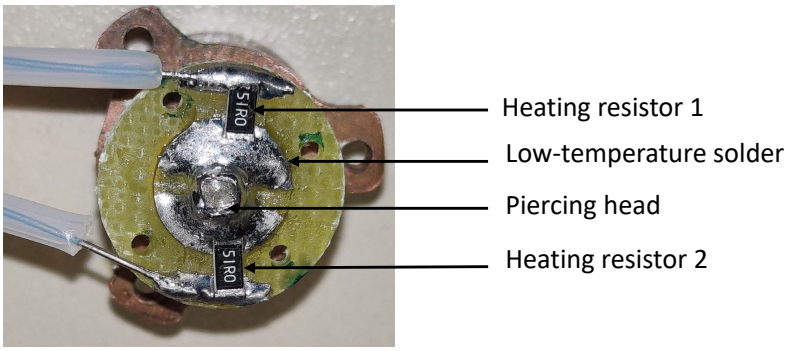

Figure 6.13. Modified release mechanism of the piercing head. An extra heating resistor is added to melt the low-temperature solder.

through the wire to trigger the piercing mechanism. However, it turned out that the wire got disconnected only from the side which was directly heated by the resistor, and as soon as the contact was lost, it cooled down immediately, and no more heat was transferred to the opposite side, keeping the connection intact and thereby failing the piercing system.

In this campaign, the source was once again filled with ^{3}He gas, and the triggering mechanism was modified by removing the wire that held the piercing head. Instead, the titanium piece attached to a copper sleeve is now directly held by low-temperature solder on both sides. And so as to not rely on heat conduction to melt the solder joint on both sides, we have placed heating resistors on both contact points of the piercing head to make sure they melt and do not prevent the triggering process. The modifications become apparent when comparing Fig. 4.5b and Fig. 6.13.

6.8.1.2 Helium-3 glass sphere

An alternative source for ^{3}He was planned while the ^{4}He measurement campaign was running, as the fault in the adsorption model source was identified only after warming up the experiment after the measurement. This alternate source is a fused silica glass sphere filled with ^{3}He gas. Such a glass sphere exhibits high permeability to helium which is strongly dependent on the temperature. At extremely low temperatures of around 4 K, the permeation rate is negligible, but as the temperature rises, there is a notable increase in the release of helium atoms from the glass sphere's walls. These atoms can be ionized and trapped using our mEBIS (see section 4.2.5). This method has been successfully implemented in [108]. The glass sphere technique is slightly disadvantaged compared to the adsorption model because not all gases permeate glass efficiently; however, it works elegantly for helium gas.

Permeation through glass involves several steps: Firstly, the gas atoms strike the wall of the sphere. These then get adsorbed and start to dissolve in the solid material of the wall. As the surface gets saturated, the gas atoms move within the bulk of the wall due to a concentration gradient and reach the outer surface of the wall, where the gas atoms get desorbed and escape to the low-pressure region. As a whole, permeation refers to the continuous and steady flow process that takes place from the gas phase on one side of a membrane (wall) to the gas phase on the other side. The diffusion process contributes to the overall permeability of the gas through the solid material. Diffusion in a solid refers to the internal process by which atoms or molecules navigate through the inter-atomic or inter-molecular spaces, thereby redistributing from one lattice position to another within the solid material. The following definitions and explanations of diffusion or permeation through solids are based on [109, 110, 111, 112].
Fick's law describes the diffusion of a substance through a medium and can be applied to the diffusion of helium through glass. The equation for Fick's law in 1-dimensional form is:

$$J = -D \cdot \frac{\partial C}{\partial x}, \tag{6.17}$$

where J represents the flux of helium atoms per unit area per unit time (atoms/cm^2/s), D is the diffusion coefficient (cm^2/s), $C = Sp$ is the concentration of helium (atoms/cm^3) which is the product of the solubility S and partial pressure p, and $\frac{\partial C}{\partial x} = \frac{S\Delta p}{d}$ denotes the concentration gradient (atoms/cm^4) when the thickness of the glass sphere wall is d.

The diffusion coefficient is a material-specific property that determines the rate at which helium atoms diffuse through the glass. In many cases, the diffusion of helium through glass follows an Arrhenius-type relationship, where the diffusion coefficient is exponentially related to temperature, given as:

$$D = D_0 \exp\left(-\frac{Q}{RT}\right), \tag{6.18}$$

where D_0 is a constant (cm^2/s), Q is the activation energy (J/mol), R is the gas constant (R = 8.314 J/mol·K), and T is the absolute temperature (K). Several factors influence helium diffusion through the glass. These include the glass composition, temperature, helium concentration gradient, and the presence of defects or imperfections in the glass structure. Higher temperatures generally enhance diffusion, while different glass compositions can exhibit varying diffusion properties. The permeability of a gas through a material, including helium diffusion through glass, is then given as:

$$K(T) = DS = K_0 \exp\left(-\frac{Q}{RT}\right). \tag{6.19}$$

From [109, 110], the coefficients for fused silica can be estimated. The activation energy at any given temperature is $Q \approx 20515.3$ J/mol, and at T_0 = 293 K, the permeability coefficient $K_0 = 5.18\times10^{-7}$ cm^3(NTP) cm s^{-1} cm^{-2} cmHg^{-1}[112, 113]. Sometimes K_0 is also simply

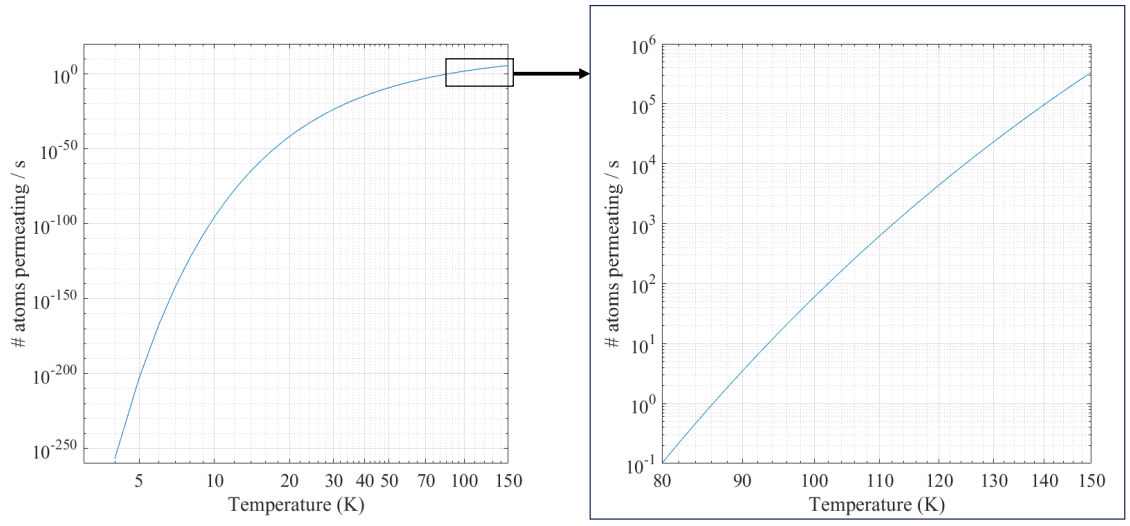

Figure 6.14. Permeation rate of helium atoms through glass sphere as a result of different temperatures is plotted in double logarithmic axes.

given in the units $cm^2\ s^{-1}$. The unit $1\ cm^3(NTP)\ cm\ s^{-1}\ cm^{-2}\ cmHg^{-1} = 1 \times 10^{10}$ barrer.

The number of helium atoms flowing through the wall per unit time can be estimated from Eq. (6.17) and Eq. (6.19) as

$$\dot{N} = A \cdot J = \frac{K(T)A\Delta p}{d} \tag{6.20}$$

where A is the area of the wall. Δp is the pressure difference on either side of the wall. In our case, it is the absolute pressure inside the sphere because outside the sphere there is a vacuum better than 10^{-17} mbar. The glass sphere used in the experiment is filled with 150 mbar of ^{3}He gas and has a radius of 5 mm and wall thickness of 0.5 mm. The initial amount of gas using ideal gas laws is $N_0 = pV/k_B/T_0 \approx 2 \times 10^{16}$ atoms, where V is the volume of the sphere. The number of atoms permeating through the wall as a function of temperature is plotted in Fig. 6.14. It is very clear that at 4 K the permeation rate is insignificant, and on increasing temperature, the flow also increases. Between 110 K and 150 K, there is a significant amount of atoms released; for example, at about 140 K 10^5 atoms are released per second, which is sufficient to create a single ion in our mEBIS.

For the preparation of the glass sphere, the same filling scheme as the adsorption model source described in the thesis was used (see Fig. 4.3), but instead of the charcoal-filled copper chamber, a blown-out glass cell of the required radius and wall thickness was placed and filled with 150 mbar of ^{3}He gas. The glass was melted using a heat torch by the glass-blowing technician to shut it and seal the gas (see Fig. 6.15). During the sealing procedure,

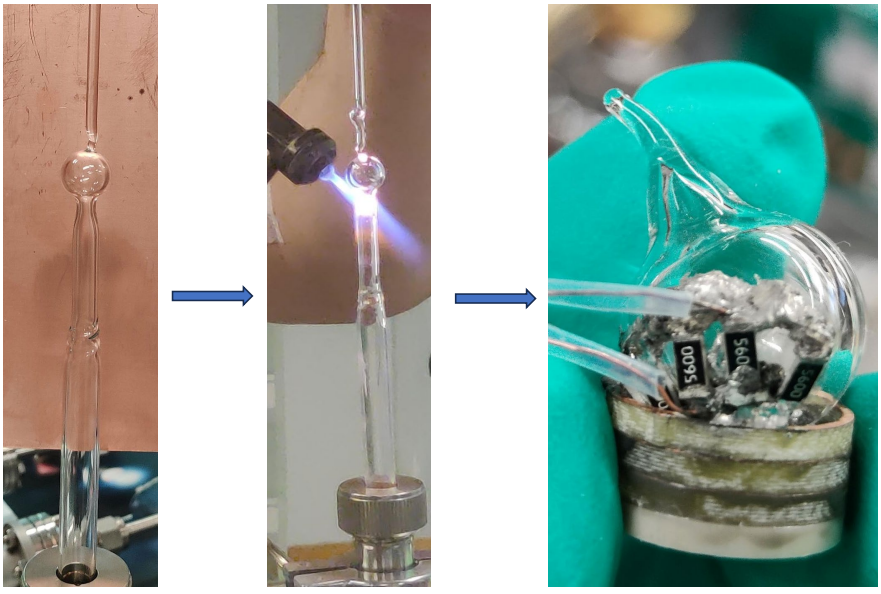

Figure 6.15. Preparation of ^{3}He glass sphere source. From left to right: a glass sphere is formed from a fused silica tube connected to the filling setup; the tube is then filled with 150 mbar ^{3}He gas and sealed shut with a heat torch; finally, heating resistors are soldered onto the glass sphere mounted on a holder that fixes the sphere in the trap chamber.

the temperature of the sphere is significantly elevated so the actual number of atoms will be somewhat lower than N_0. Once the glass sphere was prepared, SMD thin film heating resistors were soldered onto the glass using ultrasonic soldering (see Fig. 6.15). The resistors, with a total resistance of $\sim 100\,\Omega$ were chosen such that they can withstand powers in the order of $1\,\mathrm{W}$. Once prepared at room temperature, the glass sphere is carefully fixed at the outside of the trap tower at a location where there is a direct line of sight to the center of the electrodes in the production section, where the electron beam can ionize the atoms. At 4 K, due to the negligible permeation rate of gas through the walls, the sphere can be stored in the trap chamber for long periods and heated only when one needs to load ions of ^{3}He.

More technical details of the operation of the glass sphere in the trap are beyond the scope of this thesis and will be a part of the next measurement campaign.

7. Summary and outlook

In this thesis, I have presented a meticulous and successful determination of the atomic mass of ^{4}He. The fundamental principles underlying the measurement of light ion masses, in general, are also addressed in this thesis. Elaborate discussions are provided regarding the experimental setup and numerous measurements performed to optimize the trap and evaluate systematic shifts. These efforts lead to a high-precision measurement of the ^{4}He mass. Among the technical modifications made to the experiment for this measurement campaign, the most crucial was developing and installing a gas source. This source, by principle, enables our experiment to produce ions of any gaseous element which bonds very weakly and has low reactivity without compromising the exceptionally good vacuum in the trap chamber.

The ^{4}He mass measurement conducted during this work has a relative precision of 12 parts-per-trillion. The mass value exhibits a precision that is 1.3 times higher than the accepted literature value provided by the UW result. However, there is a notable deviation of our determined value from the UW result, amounting to a substantial 6.6 combined standard deviation. This discrepancy is reminiscent of the observed variations in the masses of the proton and deuteron measured at LIONTRAP.

Considering the current perspective, it seems probable that the observed discrepancies within the light ion mass puzzle (p / d / ^{12}C / ^{3}He / T system) primarily originate from the UW measurements. Recent measurements, particularly those conducted at FSU and within our research group, have agreement within their respective uncertainty levels. Nevertheless, it should be noted that measuring light masses in Penning traps presents inherent challenges. These challenges arise due to a combination of factors such as low signal intensity due to low charges and significant systematic uncertainties, which are inversely proportional to the mass. Consequently, there is a general possibility of overlooking or miscalculating relevant systematic effects, particularly within this mass regime. This also holds true for the ^{4}He mass, which has exhibited inconsistencies across multiple previous measurements. To reinstate confidence in the light ion mass regime, multiple independent and consistent measurements should be performed.

A precise and credible ^{4}He mass is of great interest. Our result with slightly improved precision can contribute towards restoring trust in the ^{4}He mass and, consequently, support the improvement of the electron mass via a g-factor determination of ^{4}He$^+$, as mentioned in the motivation of this thesis. It can serve as a strong cross-check once multiple other independent determinations of the same are performed. Moreover, bound electron magnetic moment measurement on ^{4}He$^+$ with relevant precision is planned and can be carried out by

Penning trap setups such as ALPHATRAP [105] and the experiment that recently measured the $^3He^+$ magnetic moment [108]. This makes the improvement of the electron mass possible in the near future.

As already discussed, the subsequent scientifically interesting measurement at LIONTRAP is the comparison of the masses of ^{3}He and ^{12}C to resolve the persisting uncertainties surrounding the light ion mass (light ion mass puzzle). The improved and newly developed ^{3}He sources are already installed in the trap setup, and successful production of ^{3}He using the glass sphere has already been possible. A few other potential improvements in the measurement methods were also discussed in section 6.7. The test of the two-ion-balance method opens up the possibility of significantly improved precision for the upcoming measurements.

Here, I conclude this thesis with great excitement and promising prospects for interesting measurements ahead.

Publications

1. S. Rau, F. Heiße, F. Köhler-Langes, **S. Sasidharan**, R. Haas, D. Renisch, C. Düllmann, W. Quint, S. Sturm, and K. Blaum, "Penning trap mass measurements of the deuteron and the HD+ molecular ion." Nature 585, 43–47 (2020).
   Cited as [22]

2. **S. Sasidharan**, O. Bezrodnova, S. Rau, W. Quint, S. Sturm, and K. Blaum, "Penning-Trap Mass Measurement of Helium-4", accepted (4 August 2023) by Physical Review Letters (2023).
   Cited as [92]

Bibliography

[1] J. J. Thomson, **Cathode rays**, Philos. Mag. **44**, 293 (1897).

[2] J. J. Thomson, **On the masses of the ions in gases at low pressures**, Philos. Mag. **48**, 547 (1899).

[3] P. Filianin, C. Lyu, M. Door, K. Blaum, W. J. Huang, M. Haverkort, P. Indelicato, C. H. Keitel, K. Kromer, D. Lange, Y. N. Novikov, A. Rischka, R. X. Schüssler, C. Schweiger, S. Sturm, S. Ulmer, Z. Harman, and S. Eliseev, **Direct q-value determination of the β^- decay of ^{187}Re**, Phys. Rev. Lett. **127**, 072502 (2021).

[4] D. J. Fink and E. G. Myers, **Deuteron-to-proton mass ratio from simultaneous measurement of the cyclotron frequencies of H_2^+ and D^+**, Phys. Rev. Lett. **127**, 243001 (2021).

[5] M. S. Safronova, D. Budker, D. DeMille, D. F. J. Kimball, A. Derevianko, and C. W. Clark, **Search for new physics with atoms and molecules**, Rev. Mod. Phys. **90**, 025008 (2018).

[6] S. G. Karshenboim and V. G. Ivanov, **Quantum electrodynamics, high-resolution spectroscopy and fundamental constants**, Appl. Phys. B: Lasers and Optics **123**, 18 (2017).

[7] E. Kessler, Jr, M. Dewey, R. Deslattes, A. Henins, H. Börner, M. Jentschel, C. Doll, and H. Lehmann, **The deuteron binding energy and the neutron mass**, Phys. Lett. A **255**, 221 (1999).

[8] X. Fan, T. G. Myers, B. A. D. Sukra, and G. Gabrielse, **Measurement of the electron magnetic moment**, Phys. Rev. Lett. **130**, 071801 (2023).

[9] R. H. Parker, C. Yu, W. Zhong, B. Estey, and H. Müller, **Measurement of the fine-structure constant as a test of the standard model**, Science **360**, 191 (2018).

[10] E. G. Myers, **CPT tests with the antihydrogen molecular ion**, Phys. Rev. A **98**, 010101 (2018).

[11] S. Ulmer, C. Smorra, A. Mooser, K. Franke, H. Nagahama, G. Schneider, T. Higuchi, S. Van Gorp, K. Blaum, Y. Matsuda, W. Quint, J. Walz, and Y. Yamazaki, **High-precision comparison of the antiproton-to-proton charge-to-mass ratio**, Nature **524**, 196 (2015).

[12] M. Jentschel and K. Blaum, **Balancing energy and mass with neutrons**, Nature Physics **14**, 524 (2018).

[13] S. Rainville, J. K. Thompson, E. G. Myers, J. M. Brown, M. S. Dewey, E. G. Kessler, R. D. Deslattes, H. G. Börner, M. Jentschel, P. Mutti, and D. E. Pritchard, **A direct test of E = mc^2**, Nature **438**, 1096 (2005).

[14] M. S. Dewey, E. G. K. Jr., R. D. Deslattes, H. G. Börner, M. Jentschel, C. Doll, and P. Mutti, **Precision measurement of the ^{29}Si, ^{33}S, and ^{36}Cl binding energies**, Phys. Rev. C **73**, 044303 (2006).

[15] E. Kessler, M. Dewey, R. Deslattes, A. Henins, H. Börner, M. Jentschel, and H. Lehmann, **The GAMS4 flat crystal facility**, Nucl. Instrum. Methods Phys. Res. **457**, 187 (2001).

[16] E. G. Myers, A. Wagner, H. Kracke, and B. A. Wesson, **Atomic Masses of Tritium and Helium-3**, Phys. Rev. Lett. **114**, 013003 (2015).

[17] S. L. Zafonte and R. S. Van Dyck, **Ultra-precise single-ion atomic mass measurements on deuterium and helium-3**, Metrologia **52**, 280 (2015).

[18] R. S. Van Dyck, D. L. Farnham, S. L. Zafonte, and P. B. Schwinberg, **High precision Penning trap mass spectroscopy and a new measurement of the proton's "atomic mass"**, AIP Conf Proc . **457**, 101 (1999).

[19] F. Heiße, S. Rau, F. Köhler-Langes, W. Quint, G. Werth, S. Sturm, and K. Blaum, **High-precision mass spectrometer for light ions**, Phys. Rev. A **100** (2019).

[20] E. G. Myers, **High-precision atomic mass measurements for fundamental constants**, Atoms **7** (2019).

[21] F. Heiße, F. Köhler-Langes, S. Rau, J. Hou, S. Junck, A. Kracke, A. Mooser, W. Quint, S. Ulmer, G. Werth, K. Blaum, and S. Sturm, **High-precision measurement of the proton's atomic mass**, Phys. Rev. Lett. **119**, 033001 (2017).

[22] S. Rau, F. Heiße, F. Köhler-Langes, S. Sasidharan, R. Haas, D. Renisch, C. Düllmann, W. Quint, S. Sturm, and K. Blaum, **Penning trap mass measurements of the deuteron and the HD$^+$ molecular ion**, Nature **585**, 43 (2020).

[23] D. J. Fink and E. G. Myers, **Deuteron-to-proton mass ratio from the cyclotron frequency ratio of H_2^+ to D$^+$ with H_2^+ in a resolved vibrational state**, Phys. Rev. Lett. **124**, 013001 (2020).

[24] S. Hamzeloui, J. A. Smith, D. J. Fink, and E. G. Myers, **Precision mass ratio of ^{3}He$^+$ to HD$^+$**, Phys. Rev. A **96**, 060501 (2017).

[25] M. Aker *et al.* (KATRIN), **Direct neutrino-mass measurement with sub-electronvolt sensitivity**, Nature Phys. **18**, 160 (2022).

[26] S. Patra, M. Germann, J.-P. Karr, M. Haidar, L. Hilico, V. Korobov, F. Cozijn, K. Eikema, W. Ubachs, and J. Koelemeij, **Proton-electron mass ratio from laser spectroscopy of HD^+ at the part-per-trillion level**, Science **369**, 1238 (2020).

[27] I. V. Kortunov, S. Alighanbari, M. G. Hansen, G. S. Giri, V. I. Korobov, and S. Schiller, **Proton-electron mass ratio by high-resolution optical spectroscopy of ion ensembles in the resolved-carrier regime**, Nature Phys. **17**, 569 (2021).

[28] S. Alighanbari, G. Giri, F. Constantin, V. Korobov, and S. Schiller, **Precise test of quantum electrodynamics and determination of fundamental constants with HD^+ ions**, Nature **581**, 152—158 (2020).

[29] S. Sturm, F. Köhler, J. Zatorski, A. Wagner, Z. Harman, G. Werth, W. Quint, C. Keitel, and K. Blaum, **High-precision measurement of the atomic mass of the electron**, Nature **506** (2014).

[30] S. Rau, **High-precision measurement of the deuteron's atomic mass**, Ph.D. thesis, Ruprecht-Karls-Universität, Heidelberg (2020).

[31] W. Huang, **Direct Mass Measurements and Global Evaluation of Atomic Masses**, Ph.D. thesis, Université Paris-Saclay (2018).

[32] E. Tiesinga, P. J. Mohr, D. B. Newell, and B. N. Taylor, **CODATA recommended values of the fundamental physical constants: 2018**, Rev. Mod. Phys. **93**, 025010 (2021).

[33] J. Zatorski, B. Sikora, S. Karshenboim, S. Sturm, F. Köhler-Langes, K. Blaum, C. Keitel, and Z. Harman, **Extraction of the electron mass from g factor measurements on light hydrogenlike ions**, Phys. Rev. A **96** (2017).

[34] J. Moreno, F. Schmid, J. Weitenberg, S. G. Karshenboim, T. W. Hänsch, T. Udem, and A. Ozawa, **Toward XUV frequency comb spectroscopy of the 1S-2S transition in He^+**, Eur. Phys. J. D **77**, 67 (2023).

[35] J. J. Krauth, K. Schuhmann, M. A. Ahmed, F. D. Amaro, P. Amaro, F. Biraben, T.-L. Chen, D. S. Covita, A. J. Dax, M. Diepold, *et al.*, **Measuring the α-particle charge radius with muonic helium-4 ions**, Nature **589**, 527 (2021).

[36] M. Hori and E. Widmann (ASACUSA), **Status report of the ASACUSA experiment - progress in 2021 and plans for 2022**, Tech. Rep. (CERN, Geneva, 2022).

[37] R. S. Van Dyck, D. L. Farnham, and P. B. Schwinberg, **Precision mass measurements in the UW-PTMS and the electron's "atomic mass"**, Phys. Scr. **T59**, 134 (1995).

[38] R. S. Van Dyck, S. L. Zafonte, S. Van Liew, D. B. Pinegar, and P. B. Schwinberg, **Ultraprecise atomic mass measurement of the α particle and ^{4}He**, Phys. Rev. Lett. **92**, 220802 (2004).

[39] R. S. Van Dyck, D. B. Pinegar, S. Van Liew, and S. L. Zafonte, **The UW-PTMS: Systematic studies, measurement progress, and future improvements**, Int. J. Mass Spectrom. **251**, 231 (2006).

[40] S. Brunner, T. Engel, A. Schmitt, and G. Werth, **Determination of the helium-4 mass in a Penning trap**, Eur. Phys. J. D **15**, 181 (2001).

[41] T. Fritioff, C. Carlberg, G. Douysset, R. Schuch, and I. Bergström, **A new determination of the ^{4}He and ^{3}He masses in a Penning trap**, Eur. Phys. J. D **15**, 141 (2001).

[42] S. Nagy, T. Fritioff, M. Suhonen, R. Schuch, K. Blaum, M. Björkhage, and I. Bergström, **New mass value for ^{7}Li**, Phys. Rev. Lett. **96**, 163004 (2006).

[43] W. Huang, M. Wang, F. Kondev, G. Audi, and S. Naimi, **The AME 2020 atomic mass evaluation (I). evaluation of input data, and adjustment procedures** $*$, Chin. Phys. C **45** (2021).

[44] E. Otten, **Searching the absolute neutrino mass in tritium β-decay - interplay between nuclear, atomic and molecular physics**, Hyperfine Interact. **196**, 3 (2010).

[45] **Measurement principle: model-independent neutrino mass** (2023), webpage accessed on May 28, 2023.

[46] M. Aker, K. Altenmüller, A. Beglarian, J. Behrens, A. Berlev, U. Besserer, B. Bieringer, K. Blaum, F. Block, B. Bornschein, *et al.* (KATRIN Collaboration), **Analysis methods for the first KATRIN neutrino-mass measurement**, Phys. Rev. D **104**, 012005 (2021).

[47] KATRIN Collaboration, **KATRIN design report 2004**, Tech. Rep. (Forschungszentrum Jülich, 2005).

[48] S. Earnshaw, **On the nature of the molecular forces which regulate the constitution of the luminiferous ether**, Camb. Phil. Soc. trans **7**, 97 (1842).

[49] M. J. Clerk, **VIII.A dynamical theory of the electromagnetic field**, Phil. Trans. R. Soc. **155**, 459–512 (1865).

[50] W. Paul and H. Steinwedel, **Ein neues Massenspektrometer ohne Magnetfeld**, Z. Naturforsch. A **8**, 448 (1953).

[51] W. Paul, **Electromagnetic traps for charged and neutral particles**, Rev. Mod. Phys. **62**, 531 (1990).

[52] F. Penning, **Die Glimmentladung bei niedrigem Druck zwischen koaxialen Zylindern in einem axialen Magnetfeld**, Physica **3**, 873 (1936).

[53] J. Pierce, **Theory and Design of Electron Beams**, Bell Telephone Laboratories series (Books on Demand, 1954) ed. by Nostrand, Van. New York.

[54] H. G. Dehmelt, **The Nobel Prize in Physics – Nobel Lecture** (1989).

[55] G. Gabrielse, **Relaxation calculation of the electrostatic properties of compensated Penning traps with hyperbolic electrodes**, Phys. Rev. A **27**, 2277 (1983).

[56] R. D. Knight, **The general form of the quadrupole ion trap potential**, Int. J. Mass Spectrom. and Ion Phys. **51**, 127 (1983).

[57] P. Ghosh, **Ion Traps**, Int. ser. monogr. phys. (Clarendon Press, 1995).

[58] L. S. Brown and G. Gabrielse, **Geonium theory: Physics of a single electron or ion in a Penning trap**, Rev. Mod. Phys. **58**, 233 (1986).

[59] G. J. Ketter, **Theoretical treatment of miscellaneous frequency-shifts in Penning traps with classical perturbation theory**, Ph.D. thesis, Ruprecht-Karls-Universität, Heidelberg (2015).

[60] J. Tan and G. Gabrielse, **One electron in an orthogonalized cylindrical Penning trap**, Appl. Phys. Lett. **55**, 2144 (1989).

[61] F. Major, V. Gheorghe, and G. Werth, **Charged Particle Traps: Physics and Techniques of Charged Particle Field Confinement**, Springer Series on Atomic, Optical, and Plasma Physics (Springer Berlin Heidelberg, 2005).

[62] J. Ketter, T. Eronen, M. Höcker, S. Streubel, and K. Blaum, **First-order perturbative calculation of the frequency-shifts caused by static cylindrically-symmetric electric and magnetic imperfections of a Penning trap**, Int. J. Mass Spectrom. **358**, 1 (2014).

[63] F. Köhler-Langes, **Bound-Electron g-Factor Measurements for the Determination of the Electron Mass and Isotope Shifts in Highly Charged Ions**, Ph.D. thesis, Ruprecht-Karls-Universität, Heidelberg (2015).

[64] K. S. Viswanathan, **The theory of the anharmonic oscillator**, Proc. Indian Acad. Sci. - Section A **46**, 203 (1957).

[65] T. Sailer, **Direct Bound-Electron g-Factor Difference Measurement of Coupled Ions at ALPHATRAP**, Ph.D. thesis, Ruprecht-Karls-Universität, Heidelberg (2022).

[66] J. Goldman and G. Gabrielse, **Optimized planar Penning traps for quantum-information studies**, Phys. Rev. A **81**, 052335 (2010).

[67] L. S. Brown and G. Gabrielse, **Precision spectroscopy of a charged particle in an imperfect Penning trap**, Phys. Rev. A **25**, 2423 (1982).

[68] G. Gabrielse, **The true cyclotron frequency for particles and ions in a Penning trap**, Int. J. Mass Spectrom. **279**, 107 (2009).

[69] G. Gabrielse, **Why is sideband mass spectrometry possible with ions in a Penning trap?**, Phys. Rev. Lett. **102**, 172501 (2009).

[70] W. Shockley, **Currents to Conductors Induced by a Moving Point Charge**, J. Appl. Phys. **9**, 635 (2004).

[71] S. Ramo, **Currents induced by electron motion**, Proc. of the IRE **27**, 584 (1939).

[72] H. Kolanoski and N. Wermes, **Signal formation by moving charges**, in **Particle Detectors: Fundamentals and Applications** (Oxford University Press, 2020).

[73] J. B. Johnson, **Thermal agitation of electricity in conductors**, Phys. Rev. **32**, 97 (1928).

[74] H. Nyquist, **Thermal agitation of electric charge in conductors**, Phys. Rev. **32**, 110 (1928).

[75] S. Sturm, **The g-factor of the electron bound in $^{28}Si^{13+}$: the most stringent test of bound-state quantum electrodynamics**, Ph.D. thesis, Johannes Gutenberg-Universität, Mainz (2012).

[76] D. J. Wineland and H. G. Dehmelt, **Principles of the stored ion calorimeter**, J. Appl. Phys. **46**, 919 (2008).

[77] V. Natarajan, **Penning trap mass spectroscopy at 0.1 ppb**, Ph.D. thesis, Massachusetts Institute of Technology (1993).

[78] S. R. Jefferts, T. Heavner, P. Hayes, and G. H. Dunn, **Superconducting resonator and a cryogenic GaAs field-effect transistor amplifier as a single-ion detection system**, Rev. Sci. Instrum. **64**, 737 (1993).

[79] D. Hanneke, S. Fogwell Hoogerheide, and G. Gabrielse, **Cavity control of a single-electron quantum cyclotron: Measuring the electron magnetic moment**, Phys. Rev. A **83**, 052122 (2011).

[80] L. S. Brown, G. Gabrielse, K. Helmerson, and J. Tan, **Cyclotron motion in a microwave cavity: Lifetime and frequency shifts**, Phys. Rev. A **32**, 3204 (1985).

[81] M. Schuh, F. Heiße, T. Eronen, J. Ketter, F. Köhler-Langes, S. Rau, T. Segal, W. Quint, S. Sturm, and K. Blaum, **Image charge shift in high-precision Penning traps**, Phys. Rev. A **100**, 023411 (2019).

[82] H. Häffner, **Präzisionsmessung des magnetischen Moments des Elektrons in wasserstoffähnlichem Kohlenstoff**, Ph.D. thesis, Johannes Gutenberg-Universität Mainz, Mainz (2000).

[83] E. A. Cornell, R. M. Weisskoff, K. R. Boyce, and D. E. Pritchard, **Mode coupling in a penning trap: π pulses and a classical avoided crossing**, Phys. Rev. A **41**, 312 (1990).

[84] M. Kretzschmar, **A quantum mechanical model of Rabi oscillations between two interacting harmonic oscillator modes and the interconversion of modes in a Penning trap**, AIP Conf Proc. **457**, 242 (1999).

[85] S. Sturm, A. Wagner, B. Schabinger, and K. Blaum, **Phase-sensitive cyclotron frequency measurements at ultralow energies**, Phys. Rev. Lett. **107**, 143003 (2011).

[86] E. A. Cornell, R. M. Weisskoff, K. R. Boyce, R. W. Flanagan, G. P. Lafyatis, and D. E. Pritchard, **Single-ion cyclotron resonance measurement of M(CO^+)/M(N_2^+)**, Phys. Rev. Lett. **63**, 1674 (1989).

[87] B. R. D'Urso, **Cooling and self-excitation of a one-electron oscillator**, Ph.D. thesis, Harvard University, Massachusetts (2003).

[88] B. D'Urso, B. Odom, and G. Gabrielse, **Feedback cooling of a one-electron oscillator**, Phys. Rev. Lett. **90**, 043001 (2003).

[89] J. Ketter, T. Eronen, M. Höcker, M. Schuh, S. Streubel, and K. Blaum, **Classical calculation of relativistic frequency-shifts in an ideal Penning trap**, Int. J. Mass Spectrom. **361**, 34 (2014).

[90] F. Heiße, **High-precision measurement of the proton's atomic mass**, Ph.D. thesis, Ruprecht-Karls-Universität, Heidelberg (2019).

[91] J. Alonso, K. Blaum, S. Djekic, H.-J. Kluge, W. Quint, B. Schabinger, S. Stahl, J. Verdú, M. Vogel, and G. Werth, **A miniature electron-beam ion source for in-trap creation of highly charged ions**, Rev. Sci. Instrum. **77**, 03A901 (2006).

[92] S. Sasidharan, O. Bezrodnova, S. Rau, W. Quint, S. Sturm, and K. Blaum, **Penning-trap mass measurement of helium-4** (2023), accepted (4 August 2023) by Phys. Rev. Lett.

[93] I. Vázquez, M. P. Russell, D. R. Smith, and R. Radebaugh, Helium adsorption on activated carbons at temperatures between 4 and 76 K, in **Advances in Cryogenic Engineering**, edited by R. W. Fast (Springer US, Boston, MA, 1988) pp. 1013–1021.

[94] S. Fukada and M. Terashita, **Mixed desorption of He, H_2, and CH_4 adsorbed on charcoal maximally cooled at 10K**, J. Nucl. Sci. Technol. **47**, 1219 (2010).

[95] **UM- Series; Ultrahigh Precision Multichannel Voltage Source**, Stahl-Electronics (2023).

[96] S. Sturm, I. Arapoglou, A. Egl, M. Höcker, S. Kraemer, T. Sailer, B. Tu, A. Weigel, R. Wolf, J. Crespo López-Urrutia, and K. Blaum, **The ALPHATRAP experiment**, Eur. Phys. J. Spec. Top. **227**, 1425 (2019).

[97] A. A. Wagner, **The g-factor of the valence electron bound in lithiumlike silicon $^{28}Si^{11+}$**, Ph.D. thesis, Ruprecht-Karls-Universität, Heidelberg (2013).

[98] A. Kramida, Yu. Ralchenko, J. Reader, and and NIST ASD Team, **NIST Atomic Spectra Database (ver. 5.10), [Online]** (2021), [accessed February 14, 2023].

[99] **Discussion of ICS measurement at PENTATRAP** (2023).

[100] S. Rainville, J. K. Thompson, and D. E. Pritchard, **An ion balance for ultra-high-precision atomic mass measurements**, Science **303**, 334 (2004).

[101] J. K. Thompson, S. Rainville, and D. E. Pritchard, **Cyclotron frequency shifts arising from polarization forces**, Nature **430**, 58 (2004).

[102] M. Wang, W. Huang, F. Kondev, G. Audi, and S. Naimi, **The AME 2020 atomic mass evaluation (II). tables, graphs and references** $*$, Chin. Phys. C **45**, 030003 (2021).

[103] M. Wang, G. Audi, F. G. Kondev, W. Huang, S. Naimi, and X. Xu, **The AME2016 atomic mass evaluation (II). tables, graphs and references**, Chin. Phys. C **41**, 030003 (2017).

[104] E. A. Cornell, K. R. Boyce, D. L. K. Fygenson, and D. E. Pritchard, **Two ions in a penning trap: Implications for precision mass spectroscopy**, Phys. Rev. A **45**, 3049 (1992).

[105] T. Sailer, V. Debierre, Z. Harman, F. Heiße, C. König, J. Morgner, B. Tu, A. V. Volotka, C. H. Keitel, K. Blaum, and S. Sturm, **Measurement of the bound-electron g-factor difference in coupled ions**, Nature **606**, 479 (2022).

[106] S. Rainville, **A two-ion balance for high precision mass spectrometry**, Ph.D. thesis, Massachusetts Institute of Technology (2003).

[107] J. K. Thompson, **Two-ion control and polarization forces for precise mass comparisons**, Ph.D. thesis, Massachusetts Institute of Technology (2003).

[108] A. Schneider, B. Sikora, S. Dickopf, M. Müller, N. S. Oreshkina, A. Rischka, I. A. Valuev, S. Ulmer, J. Walz, Z. Harman, C. H. Keitel, A. Mooser, and K. Blaum, **Direct measurement of the ^{3}He$^+$ magnetic moments**, Nature **606**, 878 (2022).

[109] F. J. Norton, **Helium diffusion through glass**, J. Am. Ceram. Soc. **36**, 90 (1953).

[110] V. O. Altemose, **Helium Diffusion through Glass**, J. Appl. Phys. **32**, 1309 (2004).

[111] K. Kawasaki and K. Senzaki, **Permeation of helium gas through glass**, Jpn. J. Appl. Phys. **1**, 223 (1962).

[112] W. A. Rogers, R. S. Buritz, and D. Alpert, **Diffusion Coefficient, Solubility, and Permeability for Helium in Glass**, J. Appl. Phys. **25**, 868 (2004).

[113] H. Yasuda, **Units of gas permeability constants**, J. Appl. Polym. Sci. **19**, 2529 (1975).

Acknowledgements

During my academic journey, I've come across numerous acknowledgments in various theses, and each time, they've left me with a pleasant feeling. However, I did not expect this seemingly routine task to become such an emotional experience. As I sit on a train, finally taking a trip outside my familiar office and lab after many months, I can't help but reflect on the rollercoaster of emotions that have accompanied me through this process. And now, as I write these words, having just finished my thesis, I realize that it's time for me to express my heartfelt gratitude to everyone who has supported me throughout the journey of my Ph.D.

Dear Dr. Wolfgang Quint, I want to take a moment to express my heartfelt gratitude to you. It feels like just yesterday when we met at the lab at Amrita University back in India more than five years ago during my master's degree. You mentioned the exciting work being done by the ion-trapping groups in Germany and little did I know that those conversations would shape my future. It is because of you that I am now here, working with the incredible team at LIONTRAP. You have always participated in discussions, provided valuable scientific input, and also supported and guided me during times of need throughout my Ph.D.. I want to thank you for being my supervisor and serving as a referee for this thesis.

I am grateful to Dr. Robert Moshammer for agreeing to be the second referee for this thesis and for dedicating time to review and assess my work. I also thank Prof. Joerg Jaeckel and Prof. André Butz for accepting my request to be a part of the examination committee.

I am immensely grateful to Prof. Norbert Herrmann for serving as my secondary supervisor and for diligently overseeing my scholarship.

Dear Sven, I feel incredibly fortunate to have had your mentorship throughout this journey. Your passion and brilliance as a scientist are truly remarkable and forever inspiring. I can't thank you enough for all the eye-opening discussions we've had and for the detailed clarifications of all the doubts raised. Your breadth of knowledge across various subjects never ceases to amaze me. The way you identify and approach problems and come up with some brilliant ideas is something I admire and aspire to learn from. Without your guidance, I don't think I would have made it through, and finally, this thesis wouldn't be as clear and error-free as it is now, all thanks to your careful review and feedback. I wish you all the best with Lsym and eagerly look forward to engaging in more exciting discussions with you.

Dear Klaus, Your contribution to the course of my Ph.D. has been huge. First of all, thank you for giving me this wonderful opportunity to be a part of your big ion-trapping team. Thank you for all your scientific contributions and for sharing your knowledge and expertise, whether it be during casual discussions, seminars, or MATS days. I am grateful for all the time and work you've put into reviewing the paper and providing suggestions for the abstracts and conferences. Throughout my academic journey, your willingness to offer assistance regarding any organizational issue has been inestimable. It's reassuring to know that you

are always available to help with any problem at any time. You have never failed to be the quickest to answer my emails and step up and give solutions to problems. Thanks a lot.

Dear Sascha, Thank you for your guidance through the major and the most important part of my Ph.D. journey. During the entire measurement period and analysis, you've been a great support, providing valuable mentorship and constructive criticisms that have taught me a lot. Your patience in clearing all my questions, no matter how trivial they may have seemed, is deeply appreciated. Your attention to detail, commitment, and systematic approach left a lasting impression. You have played a big role in making this work a success. Thank you.

Dear Olesia, Thank you for being an amazing teammate. We have spent countless hours together in the lab, and I genuinely cherish your companionship. It always felt good to talk to you about some problems and then get clarity from our discussions. It was also a lot of fun to break and fix things in the lab with you in our learning process. Your commitment and involvement in the experiment at all times is highly appreciated. I look forward to many more fruitful days ahead and eagerly await the exceptional outcomes that lie in the future, especially at this time with the ongoing mass measurement and promising progress so far.

Dear Florian, thank you for introducing me to the experiment and teaching me the basics of our trap. Despite it slowing you down, you generously took the time to sit with me and explain the details of each measurement and the experiment during the early days of my Ph.D., without any complaints. Beyond being a colleague, you (and Malu) have greatly eased my initial days in Germany. I am genuinely grateful for your kindness and support.

Dear Fabian, We didn't get much time to work with each other, but every discussion with you and your consistent input to the LIONTRAP group has been valuable. Your involvement and willingness to share your expertise is greatly appreciated. Thank you.

I also thank Gabi and the members of the international and personal office at MPIK for the exceptional support in making the administrative process incredibly smooth and easy.

I would like to acknowledge the assistance of the members of the MPIK and Uni Mainz technical units for helping out with fabrication work, even on short notice. Thank you, especially to Mr. Ruben Kankanyan (MPIK), Mr. Frank Müller (MPIK), Mr. Thorsten Spranz (MPIK), Mr. Yannick Steinhauser (MPIK) and Mr. Siegbert Felzer (Uni Mainz).

A big thanks to both the current and previous members of the proton experiment, namely Markus Wiesinger, Mathew Bohman, Christian Will, Hüseyin Yildiz, Peter Micke, and Christian Smorra, for all the lunchtime discussions and for helping out in filling the experiment whenever it was necessary and letting us use your lab whenever we needed, whether it was for the cold head or just borrowing some screws.

I am immensely grateful to my loving family and cherished friends, as their support and presence have made this all the more meaningful and rewarding.

Arya, all our sleepovers and gossip sessions at home have kept me sane in the last months. You have unfailingly sent reminders to finish my thesis, ensuring that I don't have to stress out at the last moment. Thanks for being there.

Tani (or Tanu, as you prefer), if this thesis has been an enjoyable read, it's all thanks to your exceptional proofreading skills. Your encouragement and wholehearted assistance, without any expectations in return, mean the world to me. I am fortunate to have you in my life.

Thank you, Sheba and Karan, for all those calls to keep in touch and for being there when I need you. It has always been fun to share each other's Ph.D. experiences. Ma (Sheela Nair), Pappa (Murali Nair), Sheba, and Karan, you have always reminded me to take breaks and to stop and smell the roses, of which I see the value and have made sure to implement in my life. Ma, thank you for praying for my success and blessing me with your kind words and Pappa for asking about my progress and wishing me luck each time.

Chechi (Indu), you have been my pillar of strength. You have stood by me through thick and thin, making me feel truly loved and cherished. You understand me like no one else, and it's crazy how you can read my emotions like a pro. To my beautiful nieces, Devu (Devika) and Bani (Shivani), thank you for being my solace in times of stress; your presence and smiles always bring comfort and joy to my heart. Chetta (Mahesh), you are an awesome brother. The way you care about everyone around you brings so much comfort. It's such a relief to have you around, taking charge of any issues that arise at home. Thanks a lot.

അമ്മേ (Maya Sasidharan) അച്ഛാ (P.V. Sasidharan), നിങ്ങളുടെ നിരന്തര പിന്തുണയും, സ്നേഹവും, പ്രോത്സാഹനവും ഇല്ലായിരുന്നെങ്കിൽ ഇതൊന്നും സാധ്യമാകുമായിരുന്നില്ല. അമ്മയുടെ പ്രാർത്ഥനയും അനുഗ്രഹവുമാണ് ഏത് പ്രശ്നത്തെയും നേരിടാനുള്ള കരുത്ത് എനിക്ക് എപ്പോഴും നൽകുന്നത്. ഞാൻ ഉടനെ 'Dr.ശശിധരൻ' ആകും എന്ന് അച്ഛൻ തമാശയായി പറയുന്നത് സത്യമാക്കാൻ ഇനി ഏതാനും മാസങ്ങൾക്കുളളിൽ സാധിക്കും എന്ന് ഞാൻ വിശ്വസിക്കുന്നു. ഈ യാത്രയിൽ കാലിടറി വിണാലും എന്നെ പിടിച്ച് എഴുനേൽപ്പിക്കാൻ നിങ്ങളുണ്ടാകും എന്ന് എനിക്കുറപ്പുണ്ട്. 'അവസാനം എല്ലാം ശരിയാകും' എന്ന് നിങ്ങൾ രണ്ടുപേരും പറയുമ്പോൾ, അത് എനിക്ക് ഒരുപാട് ആത്മവിശ്വാസം നൽകുന്നു. എപ്പോഴും എനിക്കൊപ്പം ഉണ്ടായിരുന്നതിന് നന്ദി.

Words fail to convey my gratitude, Siddharth. From the moment our paths crossed during my Ph.D. days, you have been an incomparable support system. Your love and presence have brought immense joy and warmth into my life. Thanks for tolerating my bad moods, listening to my countless rants, and offering opinions whenever I am confused. Your sacrifices did not go unnoticed – from handling household tasks on your own when I was buried in writing to cheering me up with small gestures on hectic days. Your patience and understanding have made it easier. In all those moments of self-doubt, you have offered encouragement and reassurance. I could not have asked for more. You know you are my favorite ;)
Thank you!